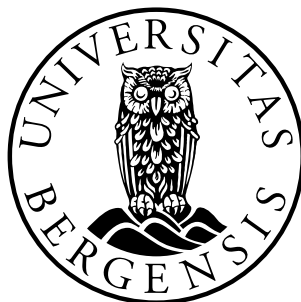


Still Water Performance Simulation of a SWATH Wind Turbine Service Vessel

Master of Science Thesis in Applied and Computational
Mathematics

Rune Angeltveit



Department of Mathematics
University of Bergen

November 20, 2012

Acknowledgements

First of all I would like to thank my supervisors Guttorm Alendal and Gunnar Furnes for all their help and good discussions through the work with my thesis. Their guidance and enthusiasm towards the project have motivated me in the work with the thesis.

Secondly I would like to thank Ove Sporsheim at MRPC(Marine Roll and Pitch Control) in Molde for letting me work with a newly developed SWATH(Small Waterplane Area Twin Hull) wind turbine service vessel for the ship owner Fredrik Odfjell, designed by Danish Yachts A/S.

I would also like to thank Vegard Larssen at Stadt Towing Tank AS (<http://www.stadttowingtank.no/>) for taking time for a visit to their hydrodynamic test facility located in Deknepollen, close to the city of Måløy and to Gunnar Furnes for bringing me to Måløy, Norway's second largest fishing port, and for good guiding and fresh local food.

I would also like to thank Henning Heiberg Andersen and Helge Avlesen at Uni Computing for helping me with all their experience with STAR-CCM+ and CFD (computational fluid dynamics), in the work with STAR-CCM+ simulation set-up and for giving me a workspace at their location. I am very grateful to CD-adapco for making the simulation possible by providing me with a student license for their CFD program STAR-CCM+.

To the end I would like to thank my fellow students for making the days at the Math department happier and more interesting. Finally, thank to my family making my education possible and to my wife Solbjørg who has supported me through the work with the thesis.

*Rune,
November 2012.*

Abstract

In this thesis I am making a computational fluid dynamics(CFD) simulation of a SWATH (Small Waterplane Area Twin Hull) wind turbine service vessel moving in still water at different speeds by using the CFD tool STAR-CCM+. Since I did not have any prior experience in CFD, a substantial part of the thesis is dedicated to theory in CFD. First of all theory for fluid dynamics and CFD methods are described. Based on this theory, models and solvers for the simulation in STAR-CCM+ are chosen with the required boundary conditions and initial values. A major part of the simulation work is to obtain a good mesh before the solution is achieved.

The paper consider the total hull resistance of the vessel at different speeds due to pressure and shear forces. The results are compared with a still water performance test for a scaled model. Wave making resistance is also considered in the comparison. The resistance on the four holes in the hull, where the ballast tanks are placed, are compared with the resistance on the hull. Secondly the paper examines how the water level inside the ballast tanks, which is open to sea at the front and at the back, are affected at different speeds.

Contents

Outline and motivation	1
1 Ship Motion	5
1.1 Motion of a marine craft	5
1.2 Motion control systems	6
1.3 Damping systems for ships	7
1.4 MRPC stabilization model	8
2 Theory from Fluid Mechanics	11
2.1 Fluid properties	11
2.2 Mass conservation	12
2.3 Conservation of momentum	14
2.4 Constitutive equation for Newtonian fluid	17
2.5 Navier-Stokes equation	20
2.6 Energy conservation	21
2.7 Thermal energy equation	22
2.8 Equation of state	24
2.9 Complete set of equations	25
2.10 Bernoulli equation	26
2.11 Boussinesq approximation	27
2.12 Dynamic similarity	30
2.13 Gravity Waves	32
3 Computational fluid dynamics	39
3.1 Discretization approaches	39
3.2 Finite volume method	41
3.3 Properties of discretization schemes	46
3.4 Central differencing scheme	48
3.5 Upwind differencing scheme	49
3.6 The hybrid differencing scheme	51
3.7 Quadratic upwind differencing scheme	51

3.8	Total variation diminishing scheme	51
3.9	Pressure-Velocity Coupling	52
3.9.1	SIMPLE algorithm	52
3.9.2	PISO algorithm	53
4	Turbulence Modelling	57
4.1	Turbulent flow	57
4.1.1	Reynolds-Averaged Navier-Stokes (RANS) Equations	58
4.2	Turbulence Models	64
4.2.1	The k-epsilon turbulence model	65
4.2.2	The k-omega turbulence model	66
5	Simulation set-up in STAR-CCM+	67
5.1	Introduction	67
5.2	3D-CAD Modeller	67
5.3	Geometry part	70
5.4	Region and boundaries	71
5.5	Surface mesh	73
5.6	Volume mesh	78
5.7	Physics models	80
5.8	Solvers	86
5.9	Analyzing	89
5.10	Force Technology still water performance test	89
6	Simulation results	91
6.1	Resistance on the twin hull	92
6.2	Force comparison	104
6.3	Water level change in the ballast tanks	107
7	Summary and Discussion	111
A	Force monitor plots	113
B	Reports	123
B.1	Force reports	123
B.2	Area of hull report	133
C	Water surface	135
	Bibliography	145

Outline and motivation

Danish Yachts has launch its advanced new range of commercial vessels designed for high-speed passenger transport. The first boat constructed in the range is the SeaStrider SWATH, see Figure 1. The purpose of the high-speed craft is to carry initially the construction teams and then the maintenance and emergency repair teams to and from the offshore windmill turbine farms efficiently, safely and in total comfort.

An important element of the vessel is to keep the vessel throughout its working life to the minimum maintenance down time and maximizing its time on the water. Therefore the vessel is the first service vessel ever to be designed and built with an active ballast tank system. The ballast tanks are open to the sea and the water level inside each ballast tank is regulated by changing the pressure inside the tank.



Figure 1: The SeaStrider SWATH designed by Danish Yachts (www.danishyachts.com/medias_news/SWATH.pdf).

In the thesis I will investigate the hull resistance of such a vessel and how the water level inside the ballast tanks will be effected at different speeds in still

water. In the 3D-CAD drawing that will be used in the simulation process, the vessel is constructed with closed ballast holes. Due to time limitations new 3D-CAD drawings of the ballast tanks with open holes to sea will not be created. Therefore I will calculate how the water level in the ballast tanks will be effected at different speeds by assuming they are open.

In the thesis I have used the CFD tool STAR-CCM+ and an IGES CAD file of the twin hull. In the start of the thesis I used the open source CFD tool OpenFOAM and SALOME. As I had no experience in computational fluid dynamics except for theory on the Navier-Stokes equations, many hours were spent in the work with simulation examples in OpenFOAM and in the study of the documentation and the user guide of OpenFOAM produced by OpenCFD (2011a,b).

As I progressed in learning OpenFOAM and after a long waiting time for the CAD file of the twin hull from Danish Yachts, the work with the twin hull could start. A great deal of effort was put into meshing this geometry by using the third party software SALOME (<http://www.salome-platform.org/>). Unfortunately I had some problems with obtaining a suitable mesh and also with the CAD geometry of the IGES file. Therefore after some discussions with Henning H. Andersen at Uni Computing, who has experience with both OpenFOAM and STAR-CCM+, I continued the CFD process by using STAR-CCM+ in the further work of the thesis.

The problem with the IGES file was solved, after some waiting time, by getting a new version of the file by Danish Yachts. The work of getting a student license from CD-adapco for STAR-CCM+ also took a long time as CD-adapco had to make an agreement with the University of Bergen. Four months after I started the work with OpenFOAM, I could continue with STAR-CCM+.

The disadvantage by choosing the commercial program STAR-CCM+ is that the simulation can only be run on one processor at a time. This has limited me in obtaining a good solution. The simulation domain had to be small and the mesh resolution big enough, for reducing the simulation time, resulting in boundary effects and a diffuse free surface.

In Chapter 1 I will look at maneuvering theory and different motion control systems will be presented. Passive and active damping systems will also be described.

In Chapter 2 I will introduce the basic definitions and concepts of fluid dynamics for providing a complete set of equations for modeling the flow.

In Chapter 3 I will look at different discretization approaches in computational fluid dynamics and the properties of discretization schemes. The most commonly used schemes are described in detail.

In Chapter 4 I will develop the Reynolds-Averaged Navier-Stokes (RANS) equations by using the continuity, momentum and energy equations, after Boussinesq approximation are applied to them, and finding their average. To provide closure of the system, the Reynolds stress in the momentum equation is modelled by using turbulence models.

In Chapter 5 I will provide the total set-up for the simulation and the different approaches tried for obtaining a good simulation. The process is described from receiving the 3D-CAD file of the vessel and the modifications done, to the long process of mesh generation, defining boundaries and selecting models and solvers.

In Chapter 6 I will present the results of the total resistance on the hull and of the four ballast tank holes. I will also compare the simulation results with the scale model test done by Force Technology, Rieu and Kishev (2012). Wave making resistance will also be presented in the comparison. At the end I present how the water level in the ballast tanks are effected at different speeds, by using Bernoulli's equation.

In Chapter 7 a summary is given together with discussion of the results and remarks on further work.

Chapter 1

Ship Motion

In this chapter I will give a short introduction in maneuvering theory, motion control systems and damping systems of ships which are mainly based upon the book of Fossen (2011). The expressions in the theory of ship motion will be used throughout the thesis.

1.1 Motion of a marine craft

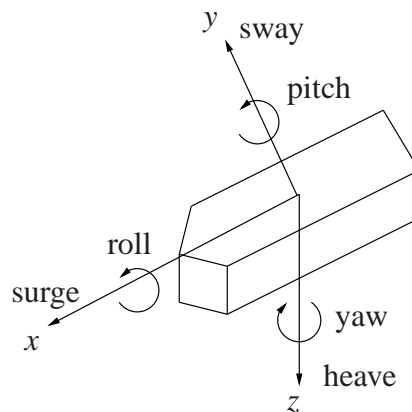


Figure 1.1: Motion in 6 degrees of freedom (DOF).

In maneuvering, a marine craft experience motion of 6 degrees of freedom (DOFs). The DOFs are the set of independent displacements and rotations that specify completely the displaced position and orientation of the craft. The motion in the horizontal plane is referred to as surge (longitudinal motion, usually superimposed on the steady propulsive motion) and sway (sideways or transverse motion). Yaw

(rotation about the normal vertical axis) describes the heading of the craft. The remaining three DOFs are roll (rotation about the longitudinal axis), pitch (rotation about the transverse axis) and heave (vertical motion), see Figure 1.1

DOF	Linear and angular velocities	Positions and Euler angles
1 motions in the x direction (surge)	u	x
2 motions in the y direction (sway)	v	y
3 motions in the z direction (heave)	w	z
4 moments about the x axis (roll, heel)	p	ϕ
5 moments about the y axis (pitch, trim)	q	θ
6 moments about the z axis (yaw)	r	ψ

Table 1.1: The notation of SNAME (1950) for marine vessels.

Roll motion is probably the most influential DOF with regards to human performance, since it produces the highest acceleration and, hence, is the principal villain in seasickness. Similarly, pitching and heaving feel uncomfortable to people.

1.2 Motion control systems

For marine craft the most common actuators are:

- **Main propellers:** The main propellers of the craft are mounted aft of the hull, usually in conjunction with rudders. They produce the necessary force F_x in the x direction needed for transit.
- **Tunnel thrusters:** These are transverse thrusters going through the hull of the craft. The propeller unit is mounted inside a transverse tube and produces a force F_y in the y direction. Tunnel thrusters are only effective at low speeds, which limits their use to low-speed maneuvering and stationkeeping.
- **Azimuth thrusters:** Thruster units that can be rotated an angle α about the z axis and produce two force components (F_x, F_y) in the horizontal plane usually referred to as azimuth thrusters. They are located usually mounted under the hull of the craft and the most sophisticated units are retractable. Azimuth thrusters are frequently used in dynamic positioning systems since they can produce forces in different directions.

- **Aft rudders:** Rudders are the primary steering device for conventional marine craft. They are located aft of the craft and the rudder force F_y will be a function of the rudder deflection (the drag force in the x direction is usually neglected in the control analysis). A rudder force in the y direction will produce a yaw moment that can be used for steering control.
- **Stabilizing fins:** Stabilizing fins are used for the damping of vertical vibrations and roll motions. They produce a force F_z in the z direction that is a function of the fin deflection. For small angles this relation is linear. Fin stabilizers can be retractable, allowing for selective use in bad weather. The lift forces are small at low speed so most effective operating condition is in transit.
- **Control surfaces:** Control surfaces can be mounted at different locations to produce lift and drag forces.
- **Water jets:** Water jets are an alternative to main propellers aft of the ship. They are usually used for high-speed craft.

1.3 Damping systems for ships

The roll motion of ships can be damped by using fins alone or in combination with rudders. The main motivation for using roll stabilization systems is to prevent cargo damage and to increase the effectiveness of the crew by avoiding or reducing seasickness. This is also important from a safety point of view.

Several passive and active systems have been proposed to accomplish roll reduction. Some passive solutions are:

Bilge Keels: Bilge keels are fins in planes approximately perpendicular to the hull or near the turn of the bilge. The longitudinal extent varies from about 25 to 50% of the length of the ship. Bilge keels are widely used, are inexpensive but increase the hull resistance. In addition to this, they are effective mainly around the natural roll frequency of the ship. This effect significantly decreases with the speed of the ship.

Hull Modifications: The shape and size of the ship hull can be optimized for minimum rolling using hydrostatic and hydrodynamic criteria. This must, however, be done before the ship is built.

Anti-Rolling Tanks: The most common anti rolling tanks in use are free-surface tanks, U-tube tanks and diversified tanks. These systems provide damping

of the roll motion even at small speeds. The disadvantages are the reduction in metacenter height due to free water surface effects and that a large amount of space is required.

The most widely used systems for active roll damping are:

Fin Stabilizers: Fin stabilizers are highly useful devices for roll damping. They provide considerable damping if the speed of the ship is not too slow. The disadvantage with additional fins is increased hull resistance and high costs associated with the installation, since at least two new hydraulic systems must be installed. Retractable fins are popular, since they are inside the hull when not in use (no additional drag). It should be noted that fins are not effective at low speed and that they cause underwater noise in addition to drag.

Rudder-Roll Damping(RRD): Roll damping by means of the rudder is relatively inexpensive compared to fin stabilizers, has approximately the same effectiveness and causes no drag or underwater noise if the system is turned off. However, RRD requires a relatively fast rudder to be effective. RRD will not be effective at low ship speeds.

Gyroscopic Roll Stabilizers: Gyroscopic roll stabilizers are typically used for boats and yachts under 100 feet. The ship gyroscopic stabilizer has a spinning rotor that generates a roll stabilizing moment that counteracts the wave-induced roll motions. Unlike stabilizing fins, the ship gyroscopic stabilizer can only produce a limited roll stabilizing moment and effective systems require approximately 3 to 5% of the craft displacement.

1.4 MRPC stabilization model

The SWATH wind turbine service vessel is designed and built with an active ballast tank system developed by the company Marine Roll & Pitch Control AS (MRPC) (http://www.mrpc.no/?page_id=307).

Technical description

The solution is based on open ballast tanks to sea in vertical direction, stretching over the sea water level. Utilizing negative- and positive pressure to work counter-phased towards waves. High volume air compressors, working with low pressure and vacuum manage volume in these tanks. The Active stabilization controller provides optimal filling in these tanks based on input from the ships movement.

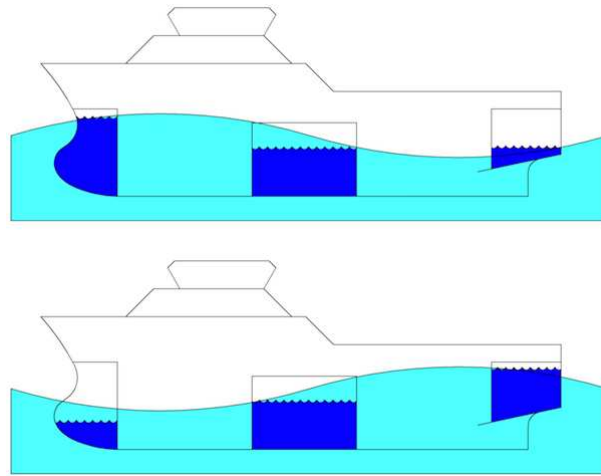


Figure 1.2: MRPC stabilization model.

Functional description

The center level and volume in the tanks is at the variation sea water level. This is to enable the system to “catch” the waves.

“Catching” the waves enables filling the tanks with seawater without any power consumption. If more filling or load on the tanks is needed, this is applied through the suction side of the compressors.

The compressors, working at high volume of air, but with low pressure and vacuum, require low power consumption.

Model verification

Through a model test at Stadt Towing Tank, using a Ramform model vessel as a test bed for the system all simulation models is verified. The model was fitted with transparent ballast tanks, valves and sensors necessary to implement the control system. Implementation of the control system has been done by Marine Innovation. The tests conclude that the stabilization principle is able to reduce the roll and pitch movement of a vessel significantly.

Chapter 2

Theory from Fluid Mechanics

In this chapter I will introduce the basic definitions and concepts of fluid dynamics for providing a complete set of equations for modelling the flow. The theory is mainly based upon the book of Kundu and Cohen (2010).

2.1 Fluid properties

Density

The density ρ of a fluid is defined as mass per unit volume and the value of density can vary widely between different fluids and changes in pressure p and temperature T . The relation between these three quantities is called equation of state:

$$\rho = \rho(p, T).$$

For liquids, variations in pressure and temperature generally have only a small effect on the value of ρ .

Viscosity

A fluid, unlike a solid, deforms continuously when a shear force is applied. Viscosity μ is a measure of the resistance of a fluid which is being deformed by shear stress. A fluid with high viscosity may be thought as a "thick" fluid, for example honey or heavy oil, while a "thin" fluid as water has low viscosity. Normally the viscosity of a fluid depends on both pressure and temperature.

Experiments shows that the magnitude of the shear stress τ along a surface, in a

horizontal fluid flow, is related to the velocity gradient by the linear relation

$$\tau = \mu \frac{du}{dy},$$

which is called Newton's law of friction. Here the constant of proportionality μ is known as the dynamic viscosity or simply the viscosity of the fluid. The kinematic viscosity ν , not involving unit mass, is given by

$$\nu = \frac{\mu}{\rho},$$

where ρ is the density.

2.2 Mass conservation

All fluid dynamics is based on the conservation of extensive properties. Extensive properties depends on the system size and the amount of material in the system. Mass and energy are extensive variables, while pressure and temperature is intensive variables. In a closed system both mass and energy are conserved. The conservation laws can be stated in differential form, applicable at a point, or in integral form, applicable to an extended region. In the integral form the laws are stated for a fixed volume Ω in space, also called control volume and geometrical volume. A material volume V following the particles.

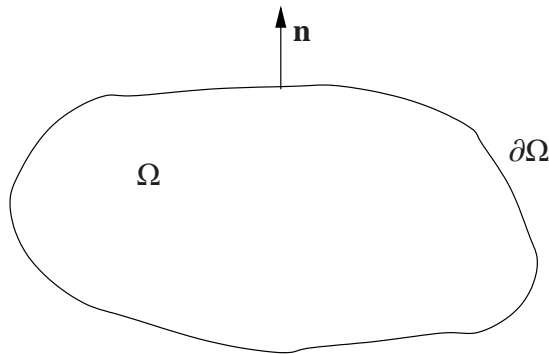


Figure 2.1: Fixed geometric volume Ω with boundary $\partial\Omega$ and outward unit normal \mathbf{n} .

To derive the conservation of mass consider a geometrical volume Ω having boundary $\partial\Omega$ and outward unit normal \mathbf{n} , see Figure 2.1. Mass may leave or enter the control volume through the boundary, or it may be accumulated or annihilated in a source or sink. The accumulation of mass inside the volume has

to be equal the produced mass through source minus net rate of mass flowing out of the volume and loss through sink. This can be written

$$\{\text{Accumulation}\} + \{\text{Net Rate Flowing Out}\} = \{\text{Source}\} - \{\text{Sink}\}. \quad (2.1)$$

Assume that there are no sources or sinks inside the volume. The accumulation of mass is given by the time derivative of the total mass, that is

$$\frac{d}{dt} \int_{\Omega} \rho dV,$$

where ρ is the density of the fluid. The total mass is expressed by the integral. Now the rate of flux through the boundary is the surface integral

$$\int_{\partial\Omega} \rho \mathbf{u} \cdot \mathbf{n} d\Omega,$$

where \mathbf{u} is the velocity and \mathbf{n} is the outward unit normal as observed in Figure 2.1. The expressions is inserted into the conservation law (2.1) and the following is obtained

$$\frac{d}{dt} \int_{\Omega} \rho dV + \int_{\partial\Omega} \rho \mathbf{u} \cdot \mathbf{n} d\Omega = 0.$$

Then apply Leibniz integral rule,

$$\frac{d}{dt} \int_{\Omega} F(x, t) dV = \int_{\Omega} \frac{\partial F}{\partial t} dV, \quad (2.2)$$

to the first term, and Gauss theorem

$$\int_{\partial\Omega} \mathbf{F} \cdot \mathbf{n} dS = \int_{\Omega} \nabla \cdot \mathbf{F} dV,$$

to the second term. Since the geometrical volume Ω is arbitrarily chosen and the integrand continuous, the pointwise mass conservation equation is obtained,

$$\frac{\partial \rho}{\partial t} + \nabla \cdot (\rho \mathbf{u}) = 0. \quad (2.3)$$

Equation (2.3) is the differential form of the principle of conservation of mass and is called the continuity equation. Rewriting the divergence term the continuity equation becomes

$$\frac{1}{\rho} \frac{D\rho}{Dt} + \nabla \cdot \mathbf{u} = 0, \quad (2.4)$$

where $\frac{D(\cdot)}{Dt} := \frac{\partial(\cdot)}{\partial t} + \mathbf{u} \cdot \nabla(\cdot)$ is the material derivative or the total derivative.

A fluid is said to be incompressible if the density of every particle in the fluid is constant in time, otherwise the fluid is compressible. Since the mass carried by individual particles by definition is constant, the volume associated with each particle has to be constant for an incompressible fluid, $dV(t) = \text{const}$. For an incompressible fluid the continuity equation (2.4) reduces to

$$\nabla \cdot \mathbf{u} = 0. \quad (2.5)$$

2.3 Conservation of momentum

Before deriving the momentum equation we must show the symmetry property of the stress tensor.

Consider an infinitesimal rectangular parallelepiped with faces perpendicular to the coordinate axes, see Figure 2.2. The first index of the stress tensor τ_{ij} indicates the normal to the surfaces on which the stress is considered. The second index indicates the direction in which the stress acts. The diagonal elements τ_{11} , τ_{22} and τ_{33} are the normal stresses, and the off diagonal elements are the tangential or shear stresses.

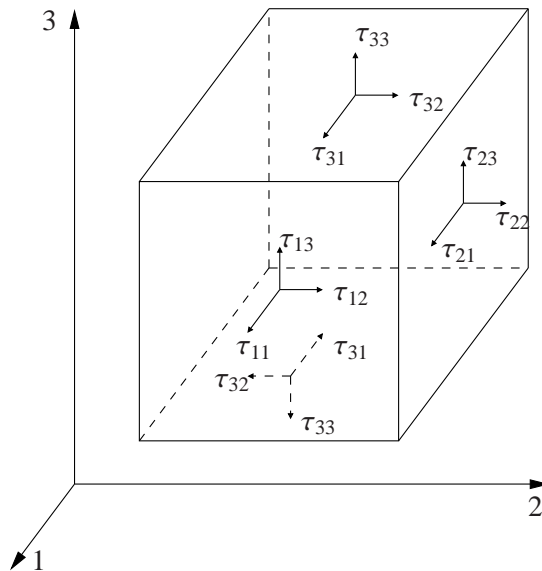


Figure 2.2: Stress at a point. Four of the six faces are shown.

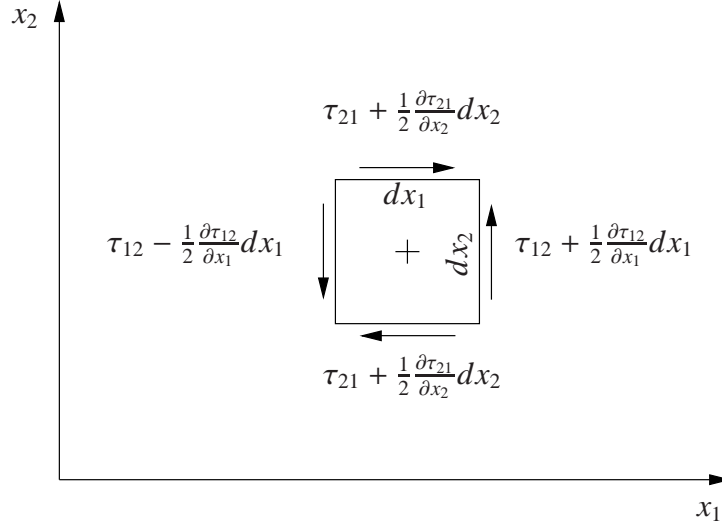


Figure 2.3: Torque on an element.

Consider the torque T on an element about a centroid axis parallel to x_3 , see Figure 2.3. The torque is generated only by the shear stresses in the x_1 x_2 -plane and is

$$T = \left[\tau_{12} + \frac{1}{2} \frac{\partial \tau_{12}}{\partial x_1} dx_1 \right] dx_2 dx_3 \frac{dx_1}{2} + \left[\tau_{12} - \frac{1}{2} \frac{\partial \tau_{12}}{\partial x_1} dx_1 \right] dx_2 dx_3 \frac{dx_1}{2} - \left[\tau_{21} + \frac{1}{2} \frac{\partial \tau_{21}}{\partial x_2} dx_2 \right] dx_1 dx_3 \frac{dx_2}{2} - \left[\tau_{21} - \frac{1}{2} \frac{\partial \tau_{21}}{\partial x_2} dx_2 \right] dx_1 dx_3 \frac{dx_2}{2}. \quad (2.6)$$

After canceling term, supposing $dx_3 = 1$, this gives

$$T = (\tau_{12} - \tau_{21}) dx_1 dx_2.$$

The rotational equilibrium of the element requires that $T = I \dot{\omega}_3$, where $\dot{\omega}_3$ is the acceleration of the element and I is its moment of inertia. For the rectangular element considered, it is easy to show that $I = dx_1 dx_2 (dx_1^2 + dx_2^2) \rho / 12$. The rotational equilibrium then requires

$$(\tau_{12} - \tau_{21}) dx_1 dx_2 = \frac{\rho}{12} dx_1 dx_2 (dx_1^2 + dx_2^2) \dot{\omega}_3,$$

that is,

$$\tau_{12} - \tau_{21} = \frac{\rho}{12} (dx_1^2 + dx_2^2) \dot{\omega}_3.$$

As dx_1 and dx_2 go to zero, the equation can only be satisfied if $\tau_{12} = \tau_{21}$. In general,

$$\tau_{ij} = \tau_{ji}.$$

The stress is therefore symmetric and has only six independent components.

For deriving the conservation of momentum in differential form, Newton's second law of motion is applied in the x_1 direction to an infinitesimal fluid element, see Figure 2.4.

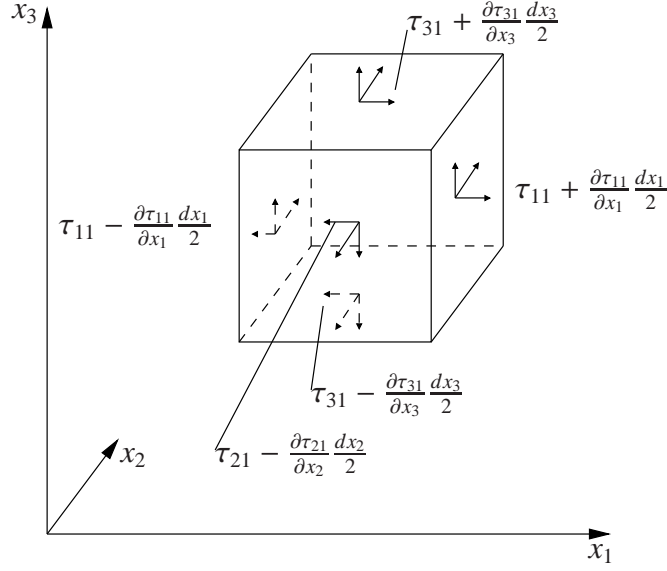


Figure 2.4: Surface stress on an element moving with the flow. Only five of the six stresses in the x_1 direction are labelled. The stress at the back is not shown.

The sum of the surface forces equals

$$\begin{aligned} & \left(\tau_{11} + \frac{\partial \tau_{11}}{\partial x_1} \frac{dx_1}{2} - \tau_{11} + \frac{\partial \tau_{11}}{\partial x_1} \frac{dx_1}{2} \right) dx_2 dx_3 \\ & + \left(\tau_{21} + \frac{\partial \tau_{21}}{\partial x_2} \frac{dx_2}{2} - \tau_{21} + \frac{\partial \tau_{21}}{\partial x_2} \frac{dx_2}{2} \right) dx_1 dx_3 \\ & + \left(\tau_{31} + \frac{\partial \tau_{31}}{\partial x_3} \frac{dx_3}{2} - \tau_{31} + \frac{\partial \tau_{31}}{\partial x_3} \frac{dx_3}{2} \right) dx_1 dx_2, \end{aligned}$$

which simplifies to

$$\left(\frac{\partial \tau_{11}}{\partial x_1} + \frac{\partial \tau_{21}}{\partial x_2} + \frac{\partial \tau_{31}}{\partial x_3} \right) dx_1 dx_2 dx_3 = \frac{\partial \tau_{j1}}{\partial x_j} dV,$$

where dV is the volume of the element. Generalizing of the surface force per unit volume of the element is

$$\frac{\partial \tau_{ij}}{\partial x_j},$$

where the symmetry property $\tau_{ij} = \tau_{ji}$ have been used. Let \mathbf{g} be the body force per unit mass, so that $\rho\mathbf{g}$ is the body force per unit volume. Then Newton's law gives

$$\rho \frac{Du_i}{Dt} = \rho g_i + \frac{\partial \tau_{ij}}{\partial x_j}, \quad (2.7)$$

which is the momentum equation, sometimes called Cauchy's equation of motion.

2.4 Constitutive equation for Newtonian fluid

The relation between the stress and deformation in a continuum is called a constitutive equation. In a fluid at rest there are only normal components of stress on a surface, and the stress does not depend on the orientation of the surface. In other words, the stress tensor is isotropic or spherically symmetric. An isotropic tensor is defined as one whose components do not change under a rotation of the coordinates system. The only second-order isotropic tensor is the Kronecker delta

$$\delta = \begin{pmatrix} 1 & 0 & 0 \\ 0 & 1 & 0 \\ 0 & 0 & 1 \end{pmatrix}.$$

Any isotropic second order-tensor must be proportional to δ . Therefore, because the stress in a static fluid is isotropic, it must be of the form

$$\tau_{ij} = -p\delta_{ij}, \quad (2.8)$$

where p is the thermodynamic pressure related to ρ and T by an equation of state, $p = p(\rho, T)$. A negative sign is introduced in equation (2.8) because the normal components of τ are regarded as positive if they indicate tension rather than compression.

A moving fluid develops additional components of stress due to viscosity. The diagonal terms of τ now become unequal, and shear stresses develop. Now for a moving fluid the stresses is split into a part $-p\delta_{ij}$ that would exist if it were at rest and a part σ_{ij} due to find the fluid motion alone:

$$\tau_{ij} = -p\delta_{ij} + \sigma_{ij}. \quad (2.9)$$

Assume that p appearing in equation (2.9) is still the thermodynamic pressure. The nonisotropic part σ , called the deviatoric stress tensor, is related to the velocity gradients $\partial u_i / \partial x_j$. The velocity gradient tensor can be decomposed into symmetric and antisymmetric parts:

$$\frac{\partial u_i}{\partial x_j} = \frac{1}{2} \left(\frac{\partial u_i}{\partial x_j} + \frac{\partial u_j}{\partial x_i} \right) + \frac{1}{2} \left(\frac{\partial u_i}{\partial x_j} - \frac{\partial u_j}{\partial x_i} \right).$$

The antisymmetric part represents fluid rotation without deformation, and cannot by itself generate stress. The stresses must be generated by the strain rate tensor

$$e_{ij} \equiv \frac{1}{2} \left(\frac{\partial u_i}{\partial x_j} + \frac{\partial u_j}{\partial x_i} \right),$$

alone. We shall assume a linear relation of the type

$$\sigma_{ij} = K_{ijmn} e_{mn}, \quad (2.10)$$

where K_{ijmn} is a fourth-order tensor having 81 components that depend on the thermodynamic state of the medium. Only two of the 81 elements of K_{ijmn} survive if it is assumed that the medium is isotropic and that the stress tensor is symmetric. It is shown in books on tensor analysis, as in Aris (1962), that all isotropic tensors of even order are made up of products of δ_{ij} and that a fourth-order isotropic tensor must have the form

$$K_{ijmn} = \lambda \delta_{ij} \delta_{mn} + \mu \delta_{im} \delta_{jn} + \gamma \delta_{in} \delta_{jm}, \quad (2.11)$$

where λ , μ and γ are scalars that depend on the local thermodynamic state. As δ_{ij} is a symmetric tensor, equation (2.10) requires that K_{ijmn} also must be symmetric in i and j . This is consistent with equation (2.11) only if

$$\gamma = \mu.$$

Only two constants μ and λ , of the original 81, have therefore survived under the restrictions of material isotropy and stress symmetry. Substitution of equation (2.11) into the constitutive equation (2.10) gives

$$\sigma_{ij} = 2\mu e_{ij} + \lambda e_{mm} \delta_{ij},$$

where $e_{mm} = \nabla \cdot \mathbf{u}$ is the volumetric strain rate, which is the sum of the linear strain rates in the three mutually orthogonal directions. The complete stress tensor (2.9) then becomes

$$\tau_{ij} = -p \delta_{ij} + 2\mu e_{ij} + \lambda e_{mm} \delta_{ij}. \quad (2.12)$$

The two scalar constants μ and λ can be further related as follows. Setting $i = j$, summing over the repeated index, and noting that $\delta_{ii} = 3$, the following is obtained

$$\tau_{ii} = -3p + (2\mu + 3\lambda) e_{mm},$$

from which the pressure is found to be

$$p = -\frac{1}{3} \tau_{ii} + \left(\frac{2}{3} \mu + \lambda \right) \nabla \cdot \mathbf{u}. \quad (2.13)$$

Now the diagonal terms of e_{ij} in a flow may be unequal. In such a case the stress tensor τ_{ij} can have unequal diagonal terms because of the presence of the term proportional to μ in equation (2.12). Therefore the average of the diagonal terms of τ is taken and a mean pressure is defined as

$$\bar{p} \equiv -\frac{1}{3}\tau_{ij}. \quad (2.14)$$

Substituting into equation (2.13) gives

$$p - \bar{p} = \left(\frac{2}{3}\mu + \lambda\right)\nabla \cdot \mathbf{u}. \quad (2.15)$$

For a completely incompressible fluid only the mechanical or mean pressure can be defined, because there is no equation of state to determine a thermodynamic pressure. The λ -term in the constitutive equation (2.12) drops out because $e_{mm} = \nabla \cdot \mathbf{u} = 0$, and no consideration of equation (2.15) is necessary. For incompressible fluids, the constitutive equation (2.12) takes the simple form

$$\tau_{ij} = -p\delta_{ij} + 2\mu e_{ij} \quad (\text{incompressible}), \quad (2.16)$$

where p can only be interpreted as the mean pressure. For a compressible fluid, on the other hand, a thermodynamic pressure can be defined, and it seems that p and \bar{p} can be different. In fact, equation (2.15) relates this difference to the rate of expansion through the proportionality constant $\kappa = \lambda + 2\mu/3$, which is called the coefficient of bulk viscosity. For many applications the Stokes assumption

$$\lambda + \frac{2}{3}\mu = 0, \quad (2.17)$$

is found to be sufficient accurate for determining κ , and can also be supported from the kinetic theory of monatomic gases.

To gain additional insight into the distinction between thermodynamic pressure and the mean of the normal stresses, consider a system inside a cylinder in which a piston may be moved in or out to do work. The first law of thermodynamics may be written in general terms as $de = dw + dQ = -\bar{p}dv + TdS$, where the last equality is written in terms of state functions. Then $TdS - dQ = (p - \bar{p})dv$. The Clausius-Duhem inequality, $S_2 - S_1 = \int_1^2 \frac{dQ_{rev}}{T}$ where S is entropy, whose change between states 1 and 2 and the integral is taken along any reversible process between the two states, tells us $TdS - dQ \geq 0$ for any process and, consequently, $(p - \bar{p})dv \geq 0$. Thus, for an expansion, $dv > 0$, so $p > \bar{p}$, and conversely for a compression. Equation (2.15) is:

$$p - \bar{p} = \left(\frac{2}{3}\mu + \lambda\right)\nabla \cdot \mathbf{u} = -\left(\frac{2}{3}\mu + \lambda\right)\frac{1}{\rho}\frac{D\rho}{Dt} = \left(\frac{2}{3}\mu + \lambda\right)\frac{1}{v}\frac{Dv}{Dt}, \quad v = \frac{1}{\rho}.$$

Further it is required that $(2/3)\mu + \lambda > 0$ to satisfy the Clausius-Duhem inequality statement of the second law of thermodynamics.

With the assumption $\kappa = 0$, the constitutive equation (2.12) reduces to

$$\tau_{ij} = -\left(p + \frac{2}{3}\mu\nabla \cdot \mathbf{u}\right)\delta_{ij} + 2\mu e_{ij}. \quad (2.18)$$

2.5 Navier-Stokes equation

The momentum equation for a Newtonian fluid is obtained by substituting the constitutive equation (2.18) into the Cauchy's equation of motion (2.7) to obtain

$$\rho \frac{Du_i}{Dt} = -\frac{\partial p}{\partial x_i} + \rho g_i + \frac{\partial}{\partial x_j} \left[2\mu e_{ij} - \frac{2}{3}\mu(\nabla \cdot \mathbf{u})\delta_{ij} \right], \quad (2.19)$$

where $(\partial p / \partial x_j)\delta_{ij} = \partial p / \partial x_i$ has been used. Equation (2.19) is a general form of the Navier-Stokes equation. Viscosity μ in this equation can be a function of thermodynamic state, and indeed μ for most fluids displays a rather strong dependence on temperature, decreasing with T for liquids and increasing with T for gases. However, if the temperature differences are small within the fluid, then μ can be taken outside the derivative in equation (2.19), which then reduces to

$$\begin{aligned} \rho \frac{Du_i}{Dt} &= -\frac{\partial p}{\partial x_i} + \rho g_i + 2\mu \frac{\partial e_{ij}}{\partial x_j} - \frac{2\mu}{3} \frac{\partial}{\partial x_i} (\nabla \cdot \mathbf{u}) \\ &= -\frac{\partial p}{\partial x_i} + \rho g_i + \mu \left[\nabla^2 u_i + \frac{1}{3} \frac{\partial}{\partial x_i} (\nabla \cdot \mathbf{u}) \right], \end{aligned}$$

where

$$\nabla^2 u_i \equiv \frac{\partial^2 u_i}{\partial x_j \partial x_j} = \frac{\partial^2 u_i}{\partial x_1^2} + \frac{\partial^2 u_i}{\partial x_2^2} + \frac{\partial^2 u_i}{\partial x_3^2},$$

is the Laplacian of u_i . For incompressible fluids $\nabla \cdot \mathbf{u} = 0$, and using vector notation the Navier-Stokes equation reduces to

$$\rho \frac{D\mathbf{u}}{Dt} = -\nabla p + \rho \mathbf{g} + \mu \nabla^2 \mathbf{u}. \quad (\text{incompressible}) \quad (2.20)$$

If viscous effects are negligible, which in general found to be true far from boundaries of the flow field, the Euler equation is obtained

$$\rho \frac{D\mathbf{u}}{Dt} = -\nabla p + \rho \mathbf{g}. \quad (2.21)$$

2.6 Energy conservation

An equation for mechanical energy of the fluid can be obtained by finding the scalar product of the momentum equation and the velocity vector. The equation of motion is

$$\rho \frac{Du_i}{Dt} = \rho g_i + \frac{\partial \tau_{ij}}{\partial x_j}.$$

Multiplying by u_i we obtain

$$\rho \frac{D}{Dt} \left(\frac{1}{2} u_i^2 \right) = \rho u_i g_i + u_i \frac{\partial \tau_{ij}}{\partial x_j}, \quad (2.22)$$

where the following relationships have been used $u_i \cdot \frac{\partial u_i}{\partial t} = \frac{\partial}{\partial t} \left(\frac{1}{2} u_i^2 \right)$ and $u_i \cdot (u_i \cdot \nabla u_i) = u_i \cdot \nabla \left(\frac{1}{2} u_i^2 \right)$. The equation (2.22) says that the rate of increase of kinetic energy at a point equals the sum of the rate work done by body force \mathbf{g} and the rate of work done by the net surface force $\nabla \cdot \boldsymbol{\tau}$ per unit volume.

The total work rate per unit volume at a point can be split up into two components:

$$\frac{\partial}{\partial x_j} (u_i \tau_{ij}) = \tau_{ij} \frac{\partial u_i}{\partial x_j} + u_i \frac{\partial \tau_{ij}}{\partial x_j},$$

where the second term is the rate of deformation work and the third term is the rate of increase of kinetic energy per unit volume. The deformation work rate can be rewritten using the symmetry of the stress tensor. A product of a symmetric and an antisymmetric tensor is zero. The product $\tau_{ij} (\partial u_i / \partial x_j)$ is therefore equal to τ_{ij} times the symmetric part of $\partial u_i / \partial x_j$, namely e_{ij} . Thus

$$\text{Deformation work rate per volume} = \tau_{ij} \frac{\partial u_i}{\partial x_j} = \tau_{ij} e_{ij}. \quad (2.23)$$

On substituting the Newtonian constitutive equation

$$\tau_{ij} = -p \delta_{ij} + 2\mu e_{ij} - \frac{2}{3} \mu (\nabla \cdot \mathbf{u}) \delta_{ij},$$

relation (2.23) becomes

$$\text{Deformation work} = p(\nabla \cdot \mathbf{u}) + 2\mu e_{ij} e_{ij} - \frac{2}{3} (\nabla \cdot \mathbf{u})^2,$$

where $e_{ij} \delta_{ij} = e_{ij} = \nabla \cdot \mathbf{u}$. Denoting the viscous term by ϕ , the following is obtained

$$\text{Deformation work (rate per volume)} = -p(\nabla \cdot \mathbf{u}) + \phi, \quad (2.24)$$

where

$$\phi \equiv 2\mu e_{ij}e_{ij} - \frac{2}{3}\mu(\nabla \cdot \mathbf{u})^2 = 2\mu \left[e_{ij} - \frac{1}{3}(\nabla \cdot \mathbf{u})\delta_{ij} \right]^2. \quad (2.25)$$

In order to write the energy equation in terms of ϕ we rewrite equation (2.22) in the form

$$\rho \frac{D}{Dt} \left(\frac{1}{2} u_i^2 \right) = \rho g_i u_i + \frac{\partial}{\partial x_j} (u_i \tau_{ij}) - \tau_{ij} \frac{\partial u_i}{\partial x_j}, \quad (2.26)$$

where $\tau_{ij}(\partial u_i / \partial x_j) = \tau_{ij} e_{ij}$ have been used. Using equation (2.24) to rewrite the deformation work rate per volume, equation (2.26) becomes

$$\rho \frac{D}{Dt} \left(\frac{1}{2} u_i^2 \right) = \underbrace{\rho \mathbf{g} \cdot \mathbf{u}}_{\text{rate of work by body force}} + \underbrace{\frac{\partial}{\partial x_j} (u_i \tau_{ij})}_{\text{total rate of work by } \tau} + \underbrace{p(\nabla \cdot \mathbf{u})}_{\text{rate of work by volume expansion}} - \underbrace{\phi}_{\text{rate of viscous dissipation}}. \quad (2.27)$$

2.7 Thermal energy equation

In flow with temperature variations we need an independent equation. This is provided by the first law of thermodynamics. Let \mathbf{q} be the heat flux (per unit area) and e the internal energy per unit mass; for a perfect gas $e = C_V T$, where C_V is the specific heat at constant volume (assumed constant). The sum $(e + u_i^2/2)$ can be called the "stored" energy per unit mass. The first law of thermodynamics is most easily stated for a material volume. It says that the

$$\begin{aligned} [\text{rate of stored energy}] &= [\text{sum of rate of work done}] \\ &+ [\text{heat addition to a material volume}] \end{aligned}$$

That is,

$$\frac{D}{Dt} \int_V \rho \left(e + \frac{1}{2} u_i^2 \right) dV = \int_V \rho g_i u_i dV + \int_{\partial S} \tau_{ij} u_i dS_j - \int_{\partial S} q_i dS_i. \quad (2.28)$$

The negative sign is needed on the heat transfer term because the direction of $d\mathbf{S}$ is along the outward normal to the area, and therefore $\mathbf{q} \cdot d\mathbf{S}$ represents the rate of heat outflow. To derive a differential form, all terms need to be expressed in the form of volume integrals.

But first we must generalize Leibniz integral rule (2.2). Consider a general case which $V(t)$ is neither a fixed volume nor a material volume. We write

$$\frac{D}{Dt} \int_{V(t)} F(\mathbf{x}, t) dV = \int_{V(t)} \frac{\partial F}{\partial t} dV + \int_{A(t)} d\mathbf{A} \cdot \mathbf{u}_A F, \quad (2.29)$$

where \mathbf{u}_A is the velocity of the boundary and $A(t)$ is the surface of $V(t)$. For a fixed volume $\mathbf{u}_A = 0$. For a material volume V the surfaces move with the fluid, so that $\mathbf{u}_A = \mathbf{u}$, where \mathbf{u} is the fluid velocity. Then (2.29) becomes

$$\frac{D}{Dt} \int_V F(\mathbf{x}, t) dV = \int_V \frac{\partial F}{\partial t} dV + \int_{\partial S} \mathbf{dS} \cdot \mathbf{u} F. \quad (2.30)$$

which is sometimes called the Reynolds transport theorem. Using Gauss' theorem, the transport equation (2.30) becomes

$$\frac{D}{Dt} \int_V F dV = \int_V \left[\frac{\partial F}{\partial t} + \frac{\partial}{\partial x_j} (F u_j) \right] dV.$$

Now defining a new function f such that $F \equiv \rho f$, where ρ is the fluid density. Then the preceding becomes

$$\begin{aligned} \frac{D}{Dt} \int_V \rho f dV &= \int_V \left[\frac{\partial(\rho f)}{\partial t} + \frac{\partial}{\partial x_j} (\rho f u_j) \right] dV \\ &= \int_V \left[\rho \frac{\partial f}{\partial t} + f \frac{\partial \rho}{\partial t} + f \frac{\partial}{\partial x_j} (\rho u_j) + \rho u_j \frac{\partial f}{\partial x_j} \right] dV. \end{aligned}$$

Using the continuity equation

$$\frac{\partial \rho}{\partial t} + \frac{\partial}{\partial x_j} (\rho u_j) = 0,$$

we finally obtain

$$\frac{D}{Dt} \int_V \rho f dV = \int_V \rho \frac{Df}{Dt} dV. \quad (2.31)$$

By using equation (2.31) the left hand side of the heat equation (2.28) can be written as

$$\frac{D}{Dt} \int_V \rho \left(e + \frac{1}{2} u_i^2 \right) dV = \int_V \rho \frac{D}{Dt} \left(e + \frac{1}{2} u_i^2 \right) dV.$$

Converting the two surface integral terms into volume integrals, equation (2.28) finally gives

$$\rho \frac{D}{Dt} \left(e + \frac{1}{2} u_i^2 \right) = \rho g_i u_i + \frac{\partial}{\partial x_j} (\tau_{ij} u_i) - \frac{\partial q_i}{\partial x_i}. \quad (2.32)$$

This is the first law of thermodynamics in the differential form, which has both mechanical and thermal energy terms in it. A thermal energy equation is obtained if the mechanical energy equation (2.27) is subtracted from it. This gives the thermal energy equation (commonly called the heat equation)

$$\rho \frac{De}{Dt} = -\nabla \cdot \mathbf{q} - p(\nabla \cdot \mathbf{u}) + \phi, \quad (2.33)$$

which says that internal energy increases because of convergence of heat, volume compression, and heating due to viscous dissipation.

2.8 Equation of state

A relationship between different thermodynamic state variables is called an equation of state. An equation of state provides a mathematical relationship between two or more state functions, such as its temperature, pressure, volume, or internal energy. Thermodynamics provides us with these two equations, see Dahle (2010),

$$\begin{aligned} p &= p(\rho, T), \\ e &= e(T, p). \end{aligned} \tag{2.34}$$

Another equation of state is the equation $p = \rho RT$ for a perfect gas. For a calorically perfect gas (constant specific heats), the relation for internal energy is $e = C_v T$, where C_v is the specific heat at constant volume.

2.9 Complete set of equations

Continuity equation:	$\frac{1}{\rho} \frac{D\rho}{Dt} + \nabla \cdot \mathbf{u} = 0,$
Momentum equation:	$\rho \frac{Du_i}{Dt} = -\frac{\partial p}{\partial x_i} + \rho g_i + \frac{\partial}{\partial x_j} \left[2\mu e_{ij} - \frac{2}{3}\mu(\nabla \cdot \mathbf{u})\delta_{ij} \right],$
Energy equation:	$\rho \frac{De}{Dt} = -\nabla \cdot \mathbf{q} - p(\nabla \cdot \mathbf{u}) + \phi,$
Energy dissipation:	$\phi = 2\mu \left[e_{ij} - \frac{1}{3}(\nabla \cdot \mathbf{u})\delta_{ij} \right]^2,$
Fourier's law of heat conduction:	$\mathbf{q} = -k\nabla T,$
Equation of state:	$p = p(\rho, T),$
	$e = e(\rho, T).$

Table 2.1: Complete set of equations for compressible flow

The complete set of equations, see Table 2.1, provides 11 equations for the 11 unknowns

$$\rho, p, T, e, \phi, \mathbf{u} \text{ and } \mathbf{q}. \quad (2.35)$$

More equations of state are needed to determine μ , κ and k if these are not constants. For the energy dissipation we have already assumed $\kappa = 1$.

It is clear from Table 2.1 that there are significant commonalities between the various equations. By introducing a general variable ϕ , from the book of Versteeg and Malasekera (2007), the conservative form of all fluid flow equations, including equations for scalar quantities such as temperature, can be written in the following form:

$$\frac{\partial(\rho\phi)}{\partial t} + \nabla \cdot (\rho\phi\mathbf{u}) = \nabla \cdot (\Gamma\nabla\phi) + S_\phi, \quad (2.36)$$

where Γ is the diffusive term. Equation (2.36) is usually called the transport equation. By setting ϕ equal to 1, u , w , e and selecting appropriate values for the diffusion coefficient Γ and S_ϕ we obtain each of the PDEs for mass, momentum

and energy conservation. Each of the terms in the transport equation can be expressed as following:

$$\begin{array}{ccccccc} \text{Rate of increase} & & \text{Net rate of flow} & & \text{Rate of increase} & & \text{Rate of increase} \\ \text{of } \phi \text{ of fluid} & + & \text{of } \phi \text{ out of} & = & \text{of } \phi \text{ due to} & + & \text{of } \phi \text{ due to} \\ \text{element} & & \text{fluid element} & & \text{diffusion} & & \text{sources} \end{array}$$

2.10 Bernoulli equation

The Bernoulli equation is derived from the momentum equation for inviscid flows, where viscous effects are negligible, namely the Euler equation (2.21):

$$\mathbf{u}_t + (\mathbf{u} \cdot \nabla)\mathbf{u} = \frac{1}{\rho}\nabla p + \mathbf{g}.$$

Assuming that the gravity $\mathbf{g} = -\nabla(gz)$ is the only body force and using the following identity

$$(\mathbf{u} \cdot \nabla)\mathbf{u} = \nabla\left(\frac{1}{2}\mathbf{u} \cdot \mathbf{u}\right) - \mathbf{u} \times (\nabla \times \mathbf{u}),$$

the Euler equation becomes

$$\mathbf{u}_t + \nabla\left(\frac{1}{2}\mathbf{u} \cdot \mathbf{u}\right) - \mathbf{u} \times (\nabla \times \mathbf{u}) = \frac{1}{\rho}\nabla p - \nabla(gz). \quad (2.37)$$

Now assuming that ρ is a function of p only. A flow which $\rho = \rho(p)$ is called a barotropic flow. For such a flow we can write

$$\frac{1}{\rho} \frac{\partial p}{\partial x_i} = \frac{\partial}{\partial x_i} \int \frac{dp}{\rho}. \quad (2.38)$$

Using equation (2.38), the Euler equation (2.37) becomes

$$\mathbf{u}_t + \nabla\left(\frac{1}{2}\mathbf{u} \cdot \mathbf{u} + \int \frac{dp}{\rho} + gz\right) = \mathbf{u} \times \boldsymbol{\omega},$$

where $(\nabla \times \mathbf{u}) = \boldsymbol{\omega}$ and $\boldsymbol{\omega}$ is the vorticity. Defining the Bernoulli function

$$B = \frac{1}{2}\mathbf{u} \cdot \mathbf{u} + \int \frac{dp}{\rho} + gz = \frac{1}{2}\mathbf{u} \cdot \mathbf{u} + \frac{p}{\rho} + gz,$$

the Euler equation becomes

$$\mathbf{u}_t + \nabla(B) = \mathbf{u} \times \boldsymbol{\omega}. \quad (2.39)$$

Important deductions can be made from the preceding by considering two special cases, namely a steady flow (rotational or irrotational) and an unsteady irrotational flow.

Steady flow

A steady flow is independent of time and equation (2.39) reduces to

$$\nabla(B) = \mathbf{u} \times \boldsymbol{\omega}. \quad (2.40)$$

The left-hand side is a vector perpendicular to both \mathbf{u} and $\boldsymbol{\omega}$. It follows that surface of constant B must contain the streamlines and vortex lines. Thus an inviscid, steady, barotropic flow satisfies

$$\frac{1}{2}\mathbf{u} \cdot \mathbf{u} + \frac{p}{\rho} + gz = \text{constant along streamlines and vortex lines}, \quad (2.41)$$

which is called the Bernoulli equation. If, in addition the flow is irrotational, $\boldsymbol{\omega} = 0$, then equation (2.40) shows that

$$\frac{1}{2}\mathbf{u} \cdot \mathbf{u} + \frac{p}{\rho} + gz = \text{constant everywhere}.$$

Unsteady irrotational flow

An unsteady form of Bernoulli's equation can be derived only if the flow is irrotational. For irrotational flows the velocity vector can be written as the gradient of a scalar potential ϕ , called velocity potential:

$$\mathbf{u} \equiv \nabla\phi. \quad (2.42)$$

On inserting equation (2.42) into equation (2.39), the following is obtained

$$\nabla \left[\frac{\partial\phi}{\partial t} + \frac{1}{2}\mathbf{u} \cdot \mathbf{u} + \frac{p}{\rho} + gz \right] = 0,$$

that is

$$\frac{\partial\phi}{\partial t} + \frac{1}{2}\mathbf{u} \cdot \mathbf{u} + \frac{p}{\rho} + gz = F(t),$$

where the integrating function $F(t)$ is independent of location.

2.11 Boussinesq approximation

For flows satisfying certain conditions, Boussinesq in 1903 suggested that the density changes in the fluid can be neglected except in the gravity term where ρ is multiplied by g . This approximation also treats the other properties of the fluid (such as μ, k, C_p) as constants. The Boussinesq approximation applies if the Mach number of the flow is small, propagation of sound or shock waves is not considered, the vertical scale of the flow is not too large, and the temperature differences in the fluid is small.

Continuity equation

The Boussinesq approximation replaces the continuity equation

$$\frac{1}{\rho} \frac{D\rho}{Dt} + \nabla \cdot \mathbf{u} = 0, \quad (2.43)$$

by the incompressible form

$$\nabla \cdot \mathbf{u} = 0. \quad (2.44)$$

The density is not regarded as constant along the direction of motion, but simply that the magnitude of $\rho^{-1}(D\rho/Dt)$ is small in comparison to the magnitudes of the velocity gradients in $\nabla \cdot \mathbf{u}$.

Momentum equation

Because of the incompressible continuity equation $\nabla \cdot \mathbf{u} = 0$, the stress tensor is given by equation (2.16). From equation (2.20), the equation of motion is then

$$\rho \frac{D\mathbf{u}}{Dt} = -\nabla p + \rho \mathbf{g} + \mu \nabla^2 \mathbf{u}. \quad (2.45)$$

Consider a hypothetical static reference state in which the density is ρ_0 everywhere and the pressure is $p_0(z)$, so that $\nabla p_0 = \rho_0 \mathbf{g}$. Subtracting this state from equation (2.45) and writing $p = p_0 + p'$ and $\rho = \rho_0 + \rho'$, we obtain

$$\rho \frac{D\mathbf{u}}{Dt} = -\nabla p' + \rho' \mathbf{g} + \mu \nabla^2 \mathbf{u}. \quad (2.46)$$

Dividing by ρ_0 , we obtain

$$\left(1 + \frac{\rho'}{\rho_0}\right) \frac{D\mathbf{u}}{Dt} = -\frac{1}{\rho_0} \nabla p' + \frac{\rho'}{\rho_0} \mathbf{g} + \nu \nabla^2 \mathbf{u}, \quad (2.47)$$

where $\nu = \mu/\rho_0$. The ratio ρ'/ρ_0 appears in both the inertia and the buoyancy terms. For small values of ρ'/ρ_0 , the density variations generate only a small correction to the inertia term and can be neglected. However, the buoyancy term $\rho'g/\rho_0$ is very important and cannot be neglected.

Heat equation

From equation (2.33), the thermal energy equation is

$$\rho \frac{De}{Dt} = -\nabla \cdot \mathbf{q} - p(\nabla \cdot \mathbf{u}) + \phi. \quad (2.48)$$

Although the continuity equation is approximately $\nabla \cdot \mathbf{u} = 0$, an important point is that the volume expansion term $p(\nabla \cdot \mathbf{u})$ is not negligible compared to other dominant terms of equation (2.48); only for incompressible liquids is $p(\nabla \cdot \mathbf{u})$ negligible in equation (2.48). We have

$$-p\nabla \cdot \mathbf{u} = \frac{p}{\rho} \frac{D\rho}{Dt} \simeq \frac{p}{\rho} \left(\frac{\partial \rho}{\partial T} \right)_p \frac{DT}{Dt} = -p\alpha \frac{DT}{Dt}.$$

Assuming a perfect gas, for which $p = \rho RT$, $C_P - C_V = R$ and $\alpha = 1/T$, the foregoing estimate becomes

$$-p\nabla \cdot \mathbf{u} = -\rho RT\alpha \frac{DT}{Dt} = -\rho(C_P - C_V) \frac{DT}{Dt}.$$

Equation (2.48) then becomes

$$\rho C_P \frac{DT}{Dt} = -\nabla \cdot \mathbf{q} + \phi, \quad (2.49)$$

where we have used $e = C_V T$ for a perfect gas.

Now we show that the heating due to viscous dissipation of energy is negligible under the restrictions underlying the Boussinesq approximation. Comparing the magnitudes of viscous heating with the left-hand side of equation (2.49), we obtain

$$\frac{\phi}{\rho C_P (DT/Dt)} \sim \frac{2\mu e_{ij} e_{ij}}{\rho C_P u_j (\partial T / \partial x_j)} \sim \frac{\mu U^2 / L^2}{\rho_0 C_P U \delta T / L} = \frac{\nu}{C_P} \frac{U}{\delta T L}.$$

In typical situations this is extremely small ($\sim 10^{-7}$). Neglecting ϕ , and assuming Fourier's law of conduction

$$\mathbf{q} = -k\nabla T,$$

the heat equation (2.49) finally reduces to (if $k = \text{const.}$)

$$\frac{DT}{Dt} = \kappa \nabla^2 T,$$

where $\kappa \equiv k/\rho C_P$ is the thermal diffusivity.

Summary

The set of equations corresponding to the Boussinesq approximation is

$$\begin{aligned} \nabla \cdot \mathbf{u} &= 0, \\ \frac{D\mathbf{u}}{Dt} &= -\frac{1}{\rho_0} \nabla P + \frac{\rho \mathbf{g}}{\rho_0} + \nu \nabla^2 \mathbf{u}, \\ \frac{DT}{Dt} &= \kappa \nabla^2 T, \\ \rho &= \rho_0 [1 - \alpha(T - T_0)], \end{aligned}$$

where the z -axis is taken upward. The constant ρ_0 is a reference density corresponding to a reference temperature T_0 , which can be taken to be the mean temperature in the flow or the temperature at a boundary.

2.12 Dynamic similarity

Two flows having different values of length scales, flow speeds, or fluid properties can apparently be different but still "dynamic similar". The concept of similarity for designing models in which tests can be conducted for predicting flow properties of full-scale vessel is used a lot. The method of dynamic similarity is used in the still water performance test done by Rieu and Kischev (2012) for the company Force Technology.

To illustrate the method of determining nondimensional parameters from the governing equations, consider a flow in which both viscosity and gravity are important. An example of such a flow is the motion of a vessel, where the drag experienced is caused by generation of surface waves and by friction on the surface of the hull. All other effects such as surface tension and compressibility are neglected. The governing differential equation is the Navier-Stokes equation

$$\frac{\partial w}{\partial t} + u \frac{\partial w}{\partial x} + v \frac{\partial w}{\partial y} + w \frac{\partial w}{\partial z} = -\frac{1}{\rho} \frac{\partial p}{\partial z} - g + \frac{\mu}{\rho} \left(\frac{\partial^2 w}{\partial x^2} + \frac{\partial^2 w}{\partial y^2} + \frac{\partial^2 w}{\partial z^2} \right), \quad (2.50)$$

and two other for u and v . The equation can be nondimensionalized by defining a characteristic length scale l and a characteristic velocity scale U . Dynamic similarity requires that the flows have geometric similarity of the boundaries, so that all characteristic lengths are proportional; for example, in Figure 2.5 we must have $d/l = d_1/l_1$. Dynamic similarity also requires that the flows should be kinematically similar, that is, they should have geometrically similar streamlines. The velocities at the same relative location are therefore proportional; if the velocity at point P in Figure 2.5a is $U/2$, then the velocity at the corresponding point P_1 in Figure 2.5b must be $U_1/2$. All length and velocity scales are then proportional in a class of dynamically similar flows. Accordingly, we introduce the following nondimensional variables, denoted by primes:

$$\begin{aligned} x' &= \frac{x}{l}, & y' &= \frac{y}{l}, & z' &= \frac{z}{l}, & t' &= \frac{tU}{l}, \\ u' &= \frac{u}{U}, & v' &= \frac{v}{U}, & w' &= \frac{w}{U}, & p' &= \frac{p - p_\infty}{\rho U^2}. \end{aligned} \quad (2.51)$$

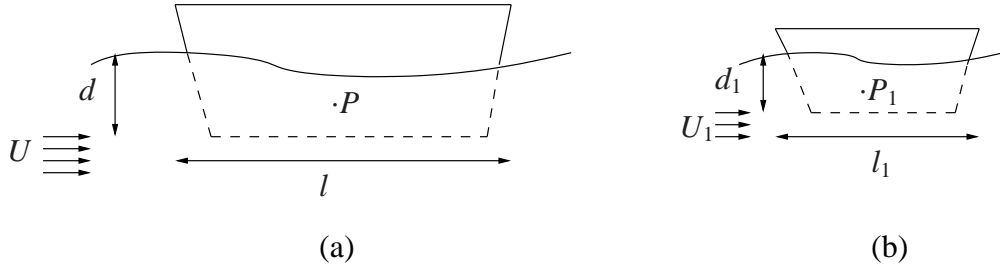


Figure 2.5: Two geometrically similar ships.

The conventional practice is to render $p - p_\infty$ dimensionless. Depending on nature of the flow, this could be in terms of viscous stress $\mu U/l$, a hydrostatic pressure $\rho g l$, or as in the preceding, a dynamic pressure ρU^2 . Substitution of equation (2.51) into equation (2.50) gives

$$\frac{\partial w'}{\partial t'} + u' \frac{\partial w'}{\partial x'} + v' \frac{\partial w'}{\partial y'} + w' \frac{\partial w'}{\partial z'} = -\frac{\partial p'}{\partial z'} - \frac{g l}{U^2} + \frac{\nu}{U l} \left(\frac{\partial^2 w'}{\partial x'^2} + \frac{\partial^2 w'}{\partial y'^2} + \frac{\partial^2 w'}{\partial z'^2} \right). \quad (2.52)$$

It is apparent that two flows will obey the same nondimensional differential equation if the values of nondimensional groups $g l / U^2$ and $\nu / U l$ are identical. Because the nondimensional boundary conditions are also identical in the two flows, it follows that they will have the same nondimensional solutions. The nondimensional parameters $U l / \nu$ and $U / \sqrt{g l}$ have been given the names:

$$\begin{aligned} \text{Re} &\equiv \frac{U l}{\nu} = \text{Reynolds number}, \\ \text{Fr} &\equiv \frac{U}{\sqrt{g l}} = \text{Froude number}. \end{aligned} \quad (2.53)$$

Both Re and Fr have to be equal for dynamic similarity of two flows in which both viscous and gravitational effects are important, see Dysthe (1992). In the Still Water Performance Test ν , ρ and g must be equal for the scaled model and the twin hull. For dynamic similarity, where both Re and Fr is equal for the two flows, we have that

$$U l = U_1 l_1 \quad \text{and} \quad U^2 l_1 = U_1^2 l,$$

which have the solution $U = U_1$, $l = l_1$. It is therefore not possible to keep both the Reynolds and the Froude number equal for the two flows. Scaling models are still used because the viscous friction and the gravitational effects in form of wave making resistance can approximately be added together. Wave making resistance does only depend on the Froude number and not the Reynolds number.

It is usual to estimate the viscous friction per area from a model test by dragging plates through the water. The total viscous friction of the ship is estimated by multiplying with the area of the wetted surface. The wave making resistance can be found by subtracting the viscous friction from the total resistance of the ship from model experiment with same Froude number.

2.13 Gravity Waves

Many wave motions of small amplitude obey the wave equation

$$\frac{\partial^2 \eta}{\partial t^2} = c^2 \nabla^2 \eta, \quad (2.54)$$

which is a linear partial differential equation of the hyperbolic type. η is any type of disturbance, for example the displacement of the free surface in a liquid. Waves travelling only in the x direction are described by

$$\frac{\partial^2 \eta}{\partial t^2} = c^2 \frac{\partial^2 \eta}{\partial x^2}, \quad (2.55)$$

which has a general solution of the form

$$\eta = f(x - ct) + g(x + ct), \quad (2.56)$$

where f and g are arbitrary functions. Equation (2.56), called d'Alembert's solution, signifies that any arbitrary function of the combination $(x \pm ct)$ is a solution of the wave equation.

Wave parameters

According to Fourier's principle, any disturbance can be decomposed into sinusoidal wave components of different wavelengths and amplitudes. We will study sinusoidal waves of the form

$$\eta = a \sin \left[\frac{2\pi}{\lambda} (x - ct) \right]. \quad (2.57)$$

The argument $2\pi(x - ct)/\lambda$ is called the phase of the wave, and points of constant phases are those where the waveform has the same value. Since η varies between $\pm a$, a is the amplitude of the wave. The parameter λ is called the wavelength because the value of η in equation (2.57) does not change if x is changed by $\pm \lambda$. The wavenumber is defined as follows

$$k \equiv \frac{2\pi}{\lambda}, \quad (2.58)$$

which is the number of complete waves in a length 2π . The waveform equation (2.57) can then be written as

$$\eta = a \sin k(x - ct). \quad (2.59)$$

The period T of a wave is the time required for the condition at a point to repeat itself, and must be equal the time required for the wave to travel one wavelength:

$$T = \frac{\lambda}{c}. \quad (2.60)$$

The number of oscillations at a point per unit time is the frequency, given by

$$\nu = \frac{1}{T}. \quad (2.61)$$

Clearly $c = \lambda\nu$. The quantity

$$\omega = 2\pi\nu = kc, \quad (2.62)$$

is called the circular frequency and is the rate of change of phase (in radians) per unit time. The speed of propagation of the waveform is related to k and ω by

$$c = \frac{\omega}{k}, \quad (2.63)$$

which is called the phase speed. In terms of ω and k , the waveform equation (2.57) is written as

$$\eta = a \sin(kx - \omega t). \quad (2.64)$$

By considering three-dimensional waves of sinusoidal shape, equation (2.64) is generalized to

$$\eta = a \sin(\mathbf{K} \cdot \mathbf{x} - \omega t), \quad (2.65)$$

where $\mathbf{K} = (k, l, m)$ is a vector called the wavenumber vector. The wavelength of (2.65) is

$$\lambda = \frac{2\pi}{K}. \quad (2.66)$$

The phase velocity is $c = \omega/K$, and the direction of propagation is that of \mathbf{K} . We can therefore write the phase velocity as the vector

$$\mathbf{c} = \frac{\omega}{K} \frac{\mathbf{K}}{K}, \quad (2.67)$$

where \mathbf{K}/K represents the unit vector in the direction of \mathbf{K} .

Surface gravity waves

In this section we shall discuss gravity waves at the free surface of a sea of liquid of uniform depth H , which may be large or small compared to the wavelength λ .

Formulation of the problem

Consider a case where the waves propagate in the x direction only, and that the motion is two dimensional in the xz – plane, see Figure 2.6.

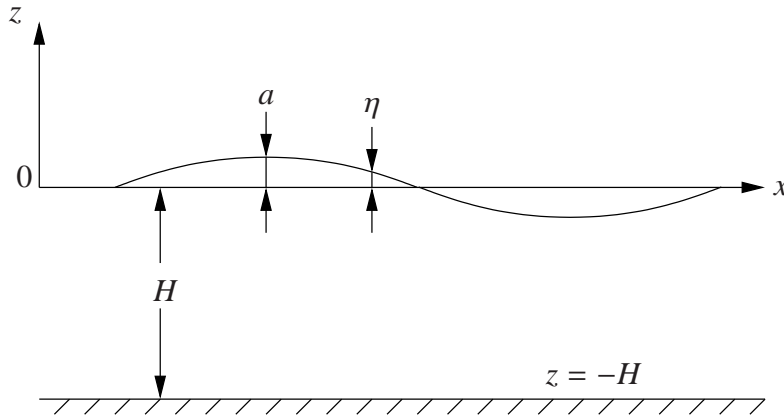


Figure 2.6: Wave nomenclature.

Let the vertical coordinate z be measured upward from the undisturbed free surface. The free surface displacement is $\eta(x, t)$. Because the motion is irrotational, a velocity potential ϕ can be defined such that

$$u = \frac{\partial \phi}{\partial x}, \quad w = \frac{\partial \phi}{\partial z}. \quad (2.68)$$

Substitution into the continuity equation

$$\frac{\partial u}{\partial x} + \frac{\partial w}{\partial z} = 0, \quad (2.69)$$

gives the Laplace equation

$$\frac{\partial^2 \phi}{\partial x^2} + \frac{\partial^2 \phi}{\partial z^2} = 0. \quad (2.70)$$

Boundary conditions are to be satisfied at the free surface and at the bottom. The condition at the bottom is zero normal velocity, that is

$$w = \frac{\partial \phi}{\partial z} = 0 \quad \text{at} \quad z = -H. \quad (2.71)$$

At the free surface, a kinematic boundary condition is that the fluid particle never leaves the surface, that is

$$\frac{D\eta}{Dt} = w_\eta \quad \text{at} \quad z = \eta, \quad (2.72)$$

where $D/Dt = \partial/\partial t + u(\partial/\partial x)$, and w_η is the vertical component of fluid velocity at the free surface. The forementioned condition can be written as

$$\left. \frac{\partial \eta}{\partial t} + u \frac{\partial \eta}{\partial x} \right|_{z=\eta} = \left. \frac{\partial \phi}{\partial z} \right|_{z=\eta}. \quad (2.73)$$

For small-amplitude waves both u and $\partial\eta/\partial x$ are small, so that the quadratic term $u(\partial\eta/\partial x)$ is one order smaller than other terms in equation (2.73), which then simplifies to

$$\left. \frac{\partial \eta}{\partial t} \right|_{z=\eta} = \left. \frac{\partial \phi}{\partial z} \right|_{z=\eta}. \quad (2.74)$$

We can simplify this condition still further by arguing that the right-hand side can be evaluated at $z = 0$ rather than at the free surface. To justify this, expand $\partial\phi/\partial z$ in a Taylor series around $z = 0$:

$$\left. \frac{\partial \phi}{\partial z} \right|_{z=\eta} = \left. \frac{\partial \phi}{\partial z} \right|_{z=0} + \eta \left. \frac{\partial^2 \phi}{\partial z^2} \right|_{z=0} + \dots \simeq \left. \frac{\partial \phi}{\partial z} \right|_{z=0}.$$

Therefore, to the first order of accuracy desired here, $\partial\phi/\partial z$ in equation (2.74) can be evaluated at $z = 0$. We then have

$$\left. \frac{\partial \eta}{\partial t} \right|_{z=\eta} = \left. \frac{\partial \phi}{\partial z} \right|_{z=0} \quad \text{at} \quad z = \eta. \quad (2.75)$$

In addition to the kinematic condition at the surface, there is a dynamic condition that the pressure just below the free surface is always equal to the ambient pressure, with surface tension neglected. Taking the ambient pressure to be zero, the condition is

$$p = 0 \quad \text{at} \quad z = \eta. \quad (2.76)$$

Since the motion is irrotational, Bernoulli's equation (2.10)

$$\frac{\partial \phi}{\partial t} + \frac{1}{2}(u^2 + w^2) + \frac{p}{\rho} + gz = F(t), \quad (2.77)$$

is applicable. Here, the function $F(t)$ can be absorbed in $\partial\phi/\partial t$ by redefining ϕ . Neglecting the nonlinear term $(u^2 + w^2)$ for small-amplitude waves the linearized form of the unsteady Bernoulli equation is

$$\frac{\partial \phi}{\partial t} + \frac{p}{\rho} + gz = 0. \quad (2.78)$$

Substitution into the surface boundary condition (2.76) gives

$$\frac{\partial\phi}{\partial t} + g\eta = 0 \quad \text{at } z = \eta. \quad (2.79)$$

As before, for small-amplitude waves, the term $\partial\phi/\partial t$ can be evaluated at $z = 0$ rather than at $z = \eta$ to give

$$\frac{\partial\phi}{\partial t} = -g\eta \quad \text{at } z = 0. \quad (2.80)$$

Solution of the problem

Recapitulating, we have to solve

$$\frac{\partial^2\phi}{\partial x^2} + \frac{\partial^2\phi}{\partial z^2} = 0, \quad (2.81)$$

subject to the conditions

$$\frac{\partial\phi}{\partial z} = 0 \quad \text{at } z = -H, \quad (2.82)$$

$$\frac{\partial\phi}{\partial z} = \frac{\partial\eta}{\partial t} \quad \text{at } z = 0, \quad (2.83)$$

$$\frac{\partial\phi}{\partial t} = -g\eta \quad \text{at } z = 0. \quad (2.84)$$

In order to apply the boundary conditions, we need to assume a form for $\eta(x, t)$. The simplest case is that of a sinusoidal component with wavenumber k and frequency ω , for which

$$\eta = a \cos(kx - \omega t). \quad (2.85)$$

For a cosine dependence of η on $(kx - \omega t)$, conditions (2.83) and (2.84) show that ϕ must be a sine function of $(kx - \omega t)$. Consequently, we assume a separable solution of the Laplace equation in the form

$$\phi = f(z) \sin(kx - \omega t), \quad (2.86)$$

where $f(z)$ and $\omega(k)$ are to be determined. After some calculations, see Kundu and Cohen (2010), the velocity potential becomes

$$\phi = \frac{a\omega}{k} \frac{\cosh k(z+H)}{\sinh kH} \sin(kx - \omega t), \quad (2.87)$$

from which the velocity components are found as

$$u = a\omega \frac{\cosh k(z+H)}{\sinh kH} \cos(kx - \omega t), \quad (2.88)$$

$$w = a\omega \frac{\sinh k(z+H)}{\sinh kH} \sin(kx - \omega t). \quad (2.89)$$

Substitution of equation (2.85) and (2.87) into (2.84) gives the relation between k and ω

$$\omega = \sqrt{gk \tanh kH}. \quad (2.90)$$

The phase speed $c = \omega/k$ is related to the wave size by

$$c = \sqrt{\frac{g}{k} \tanh kH} = \sqrt{\frac{g\lambda}{2\pi} \tanh \frac{2\pi H}{\lambda}}. \quad (2.91)$$

This shows that the speed of propagation of a wave component depends on its wavenumber. Waves for which c is a function of k are called "dispersive" because waves of different lengths, propagating at different speeds, "disperse" or separate.

For deep-water approximation ($H/\lambda \gg 1$) the phase speed, see equation (2.91), is approximated by

$$c = \sqrt{\frac{g\lambda}{2\pi}}. \quad (2.92)$$

For shallow-water approximation ($H/\lambda \ll 1$) the phase speed, see equation (2.91), is approximated by

$$c = \sqrt{gH}. \quad (2.93)$$

Energy considerations

In a dispersive system, the energy of a wave component does not propagate at the phase speed velocity $c = \omega/k$, but at the group velocity defined as $c_g = d\omega/dk$. For surface gravity waves having the dispersion relation

$$\omega = \sqrt{gk \tanh kH}, \quad (2.94)$$

the group velocity is found to be

$$c_g = \frac{c}{2} \left[1 + \frac{2kH}{\sinh kH} \right]. \quad (2.95)$$

For deep and shallow water approximation the group velocity reduces to

$$c_g = \frac{1}{2}c \quad (\text{deep water}), \quad (2.96)$$

$$c_g = c \quad (\text{shallow water}). \quad (2.97)$$

In the book of Kundu and Cohen (2010) it is shown that the wave energy (E), where kinetic (E_k) and potential (E_p) energy is considered, in a water column per unit horizontal area is

$$E = E_p + E_k = \rho g \overline{\eta^2} = \frac{1}{2} \rho g a^2, \quad (2.98)$$

where the last form in terms of amplitude a is valid if η is assumed sinusoidal.

Next we consider the rate of transmission of energy due to a single sinusoidal component of wavenumber k . Per unit length of crest, the time average energy flux is

$$F = E \cdot c_g = \left[\frac{1}{2} \rho g a^2 \right] \left[\frac{c}{2} \left(1 + \frac{2kH}{\sinh 2kH} \right) \right]. \quad (2.99)$$

The first factor is the wave energy given in (2.98). The second factor is the speed of propagation of wave energy of component k , called the group speed.

Chapter 3

Computational fluid dynamics

The following is based on the book of Ferziger and Perić (2002) which gives a good introduction to computational fluid dynamics. Flows and related phenomena can be described by partial differential equations, which cannot be solved analytically except in special cases. To obtain an appropriate solution numerically, we have to use a discretization method which approximates the differential equations by a system of algebraic equations, which can be solved on a computer. The approximations are applied to small domains in space and/or time so the numerical solution provides results at discrete locations in space and time. Such as the accuracy of experimental data depends on the quality of the tools used, the accuracy of numerical solutions are dependent on the quality of discretizations used.

In the following sections the discretization approaches and the details for the finite volume method will be presented by using the theory from the book of Versteeg and Malasekera (2007). Numerical method for pure diffusion and convection-diffusion in steady state will be developed for the finite volume method. Afterwards the properties of the main discretization schemes, used in CDF, will be discussed. The central differencing scheme and the upwind differencing scheme will be explained in detail.

3.1 Discretization approaches

In the book of Ferziger and Perić (2002) we can read about the three main discretization methods for solving partial differential equations, respectively the finite difference method, the finite volume method and the finite element method.

Finite difference method

The finite difference (FD) method is the oldest method for numerical solution of PDE's believed to have been introduced by Euler in the 18th century. The starting point is the conservation equation in differential form. The solution domain is covered by a grid. At each grid point, the differential equation is approximated by replacing the partial derivatives by approximations in terms of the nodal values of the functions. The result is one algebraic equation per grid node, in which the variable value at that and a certain number of neighbour nodes appear as unknowns. In principle, the FD method can be applied to any grid type. However, in most applications it has been applied to structured grids. Taylor series expansion or polynomial fitting is used to obtain approximations to the first and second derivatives of the variables with respect to the coordinates. The disadvantage of FD methods is that the conservation is not enforced unless special care is taken. Also, the restriction to simple geometries is a significant disadvantage in complex flows.

Finite volume method

The finite volume (FV) method uses the integral form of the conservation equations as its starting point. The solution domain is subdivided into a finite number of contiguous control volumes (CVs), and the conservation equations are applied to each CV. At the centroid of each CV lies a computational node at which the variable values are to be calculated. Interpolation is used to express variable values at the CV surface in terms of the nodal (CV-center) values. The FV method can accommodate any type of grid, so it is suitable for complex geometries. The grid defines only the control volume boundaries and need not be related to a coordinate system. The method is conservative by construction. The disadvantage of FV methods compared to FD schemes is that methods of order higher than second are more difficult in 3D. This is due to the fact that the FV approach requires three levels of approximation: interpolation, differentiation and integration.

Finite element method

The finite element (FE) method is similar to the FV method in many ways. The domain is broken into a set of discrete volumes or finite elements that are generally unstructured. The distinguishing feature of FE methods is that the equations are multiplied by a weight function before they are integrated over the entire domain. In the simplest FE methods, the solution is approximated by a linear shape function within each element in a way that guarantees continuity of the solution across element boundaries. Such a function can be constructed from its values

at the corners of the elements. The weight function is usually of the same form. An important advantage of finite element methods is the ability to deal with arbitrary geometries. The principle drawback, which is shared by any method that uses unstructured grids, is that the matrices of the linearized equations are not as well structured as those for regular grids making it more difficult to find efficient solution methods.

It has generally been found that the finite element method requires greater computational resources and computer processing power than the equivalent finite volume method, see Tu et al. (2007).

3.2 Finite volume method

Based on the book of Versteeg and Malasekera (2007) we will first develop the numerical method the finite volume method, by considering the simplest transport process of all: pure diffusion in the steady state. The governing equation of diffusion can easily be derived from the general transport equation (2.36),

$$\frac{\partial(\rho\phi)}{\partial t} + \nabla \cdot (\rho\phi\mathbf{u}) = \nabla \cdot (\Gamma\nabla\phi) + S_\phi,$$

for property of ϕ by deleting the transient and convective terms. This gives

$$\nabla \cdot (\Gamma\nabla\phi) + S_\phi = 0. \quad (3.1)$$

The control volume integration, which forms the key step of the finite volume method that distinguishes it from all other CFD techniques, yields the following form,

$$\int_{CV} \nabla \cdot (\Gamma\nabla\phi) + \int_{CV} S_\phi = 0 = \int_A \mathbf{n} \cdot (\Gamma\nabla\phi)dA + \int_{CV} S_\phi dV = 0, \quad (3.2)$$

where Gauss's divergence theorem has been applied to the first volume integral. By working with one-dimensional steady state diffusion equation, the approximation techniques that are needed to obtain the discretized equations are introduced.

By considering the steady state diffusion of a property ϕ in one-dimensional domain defined in Figure 3.1. The process is governed by

$$\frac{d}{dx} \left(\Gamma \frac{d\phi}{dx} \right) + S = 0, \quad (3.3)$$

where Γ is the diffusion coefficient and S is the source term. Boundary values at points A and B are prescribed.

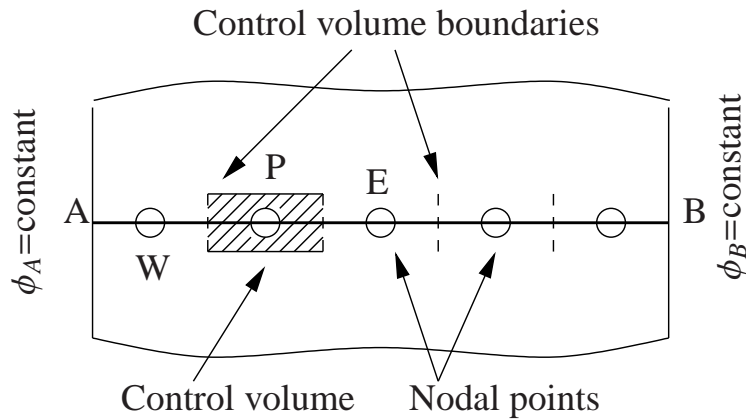


Figure 3.1: One dimensional domain.

Step 1: Grid generation

The first step in the finite volume method is to divide the domain into discrete control volumes. A number of nodal points is placed in the space between A and B. The boundaries, or faces, of the control volumes are positioned mid-way between adjacent nodes.

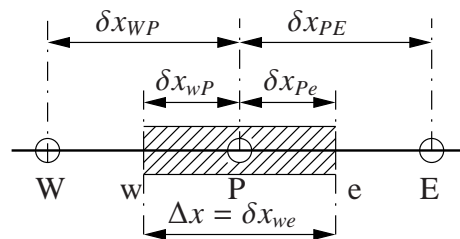


Figure 3.2: One dimensional grid.

A general nodal point is identified by P and its neighbours in a one-dimensional geometry, the nodes to the west and east, are identified by W and E respectively. The west side face of the control volume is referred to by w and the east side control volume face by e . The distances between the nodes W and P , and between nodes P and E , are identified by δx_{WP} and δx_{PE} respectively. Similarly the distances between face w and point P and between P and face e are denoted by δx_{wP} and δx_{Pe} respectively. Figure 3.2 shows that the control volume width is $\Delta x = \delta x_{we}$.

Step 2: Discretization

The key step of the finite volume method is the integration of the governing equation over a control volume to yield a discretized equation at its nodal point P . For the control volume defined above this gives

$$\int_{\Delta V} \frac{d}{dx} \left(\Gamma \frac{d\phi}{dx} \right) dV + \int_{\Delta V} S dV = \left(\Gamma A \frac{d\phi}{dx} \right)_e - \left(\Gamma A \frac{d\phi}{dx} \right)_w + \bar{S} \Delta V = 0. \quad (3.4)$$

Here A is the cross-sectional area of the control volume face, ΔV is the volume and \bar{S} is the average value of source S over the control volume. Equation (3.4) states that the diffusive flux of ϕ leaving the east face minus the diffusive flux of ϕ entering the west face is equal to the generation of ϕ .

In order to derive useful forms of the discretized equations, the interface diffusion coefficient Γ and the gradient $d\phi/dx$ at east and west are required. Following well established practice, the values of the property ϕ and the diffusion coefficient are defined and evaluated at nodal points. To calculate gradients and fluxes at the control volume faces an approximate distribution of properties between nodal points is used. Linear approximations seem to be the obvious and simplest way of calculating interface values and the gradients. The practice is called central differencing. In a uniform grid, linearly interpolated values of Γ_w and Γ_e are given by

$$\Gamma_w = \frac{\Gamma_W + \Gamma_P}{2}, \quad (3.5)$$

$$\Gamma_e = \frac{\Gamma_P + \Gamma_E}{2}. \quad (3.6)$$

And the diffusive flux terms are evaluated as

$$\left(\Gamma A \frac{d\phi}{dx} \right)_e = \Gamma_e A_e \left(\frac{\phi_E - \phi_P}{\delta x_{PE}} \right), \quad (3.7)$$

$$\left(\Gamma A \frac{d\phi}{dx} \right)_w = \Gamma_w A_w \left(\frac{\phi_P - \phi_W}{\delta x_{WP}} \right). \quad (3.8)$$

In practical situations the source term S may be a function of the dependent variable. In such cases the finite volume method approximates the source term by means of a linear form:

$$\bar{S} \Delta V = S_u + S_P \phi_P. \quad (3.9)$$

Substitution of the equations (3.7), (3.8) and (3.9) into equation (3.4) gives

$$\Gamma_e A_e \left(\frac{\phi_E - \phi_P}{\delta x_{PE}} \right) - \Gamma_w A_w \left(\frac{\phi_P - \phi_W}{\delta x_{WP}} \right) + (S_u + S_P \phi_P) = 0. \quad (3.10)$$

This can be rearranged as

$$\left(\frac{\Gamma_e}{\delta x_{PE}}A_e + \frac{\Gamma_w}{\delta x_{WP}} - S_P\right)\phi_P = \left(\frac{\Gamma_w}{\delta x_{WP}}A_w\right)\phi_W + \left(\frac{\Gamma_e}{\delta x_{PE}}A_e\right)\phi_E + S_u. \quad (3.11)$$

Identifying the coefficients of ϕ_W and ϕ_E in equation (3.11) as a_W and a_E , and the coefficient of ϕ_P as a_P , the above equation can be written as

$$a_P\phi_P = a_W\phi_W + a_E\phi_E + S_u, \quad (3.12)$$

where

$$a_w = \frac{\Gamma_w}{\delta x_{WP}}A_w, \quad a_e = \frac{\Gamma_e}{\delta x_{PE}}A_e, \quad a_P = a_W + a_E - S_P.$$

Equation (3.12) represents the discretized form for the steady state diffusion problem.

Step 3: Solution of the equations

Discretized equations of the form (3.12) must be set up at each of the nodal points in order to solve a problem. For control volumes that are adjacent to the domain boundaries the general discretized equation (3.12) is modified to incorporate boundary conditions. The resulting system of linear algebraic equations is then solved to obtain the distribution of the property ϕ at nodal points.

Steady state convection-diffusion equation

In the absence of sources, steady convection and diffusion of a property ϕ in a given one-dimensional flow field u is governed by

$$\frac{d}{dt}(\rho u \phi) = \frac{d}{dx}\left(\Gamma \frac{d\phi}{dx}\right). \quad (3.13)$$

The flow must satisfy the continuity equation, so

$$\frac{d(\rho u)}{dx} = 0. \quad (3.14)$$

We consider the one dimensional control volume shown in Figure 3.3.

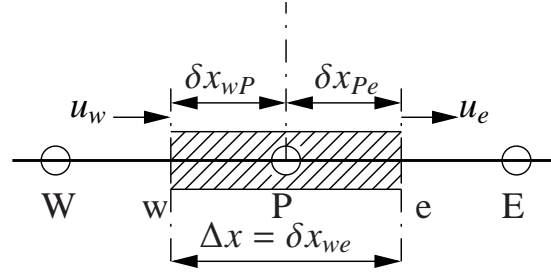


Figure 3.3: A control volume around node P . One dimensional grid.

Integration of the transport equation (3.13) over the control volume of Figure 3.3 gives

$$(\rho u A \phi)_e - (\rho u A \phi)_w = \left(\Gamma A \frac{d\phi}{dx} \right)_e - \left(\Gamma A \frac{d\phi}{dx} \right)_w. \quad (3.15)$$

And integration of continuity equation (3.14) yields

$$(\rho u A)_e - (\rho u A)_w = 0. \quad (3.16)$$

To obtain discretized equations for the convection-diffusion problem we must approximate the terms in equation (3.15). It is convenient to define two variables F and D to represent the convective mass flux per unit area and diffusion conductance at cell faces:

$$F = \rho u \quad \text{and} \quad D = \frac{\Gamma}{\delta x}. \quad (3.17)$$

The cell face values of the variables F and D can be written as

$$F_w = (\rho u)_w, \quad F_e = (\rho u)_e, \quad (3.18)$$

$$D_w = \frac{\Gamma_w}{\delta x_{wP}}, \quad D_e = \frac{\Gamma_e}{\delta x_{Pe}}. \quad (3.19)$$

We develop our techniques assuming that $A_w = A_e = A$, so we can divide the left and right hand side of equation (3.15) by area A . As before, we employ the central differencing approach to represent the contribution of the diffusion terms on the right hand side. The integrated convection-diffusion (3.15) can now be written as

$$F_e \phi_e - F_w \phi_w = D_e (\phi_E - \phi_P) - D_w (\phi_P - \phi_W), \quad (3.20)$$

and the integrated continuity equation (3.16) as

$$F_e - F_w = 0. \quad (3.21)$$

We also assume that the velocity field is known which takes care of the values of F_e and F_w . In order to solve equation (3.20) we need to calculate the transported property ϕ at the e and w faces. There are several schemes for this purpose.

3.3 Properties of discretization schemes

In theory numerical results may be obtained that are indistinguishable from the 'exact' solution of the transport equation when the number of computational cells is infinitely large. However, in practical calculations we can only use a finite, sometimes quite small, number of cells, and our numerical results will be physically realistic when the discretization schemes has certain fundamental properties. The most important ones are:

- Conservativeness
- Boundedness
- Transportiveness

Conservativeness

Integration of the convection-diffusion equation over a finite number of control volumes yields a set of discretized conservation equations involving fluxes of the transported property ϕ through control volume faces. To ensure conservation of ϕ for the whole solution domain the flux of ϕ leaving a control volume across a certain face must be equal to the flux of ϕ entering the adjacent control volume through the same face. To achieve this the flux through a common face must be represented in a consistent manner, by one and the same expression, in adjacent control volumes.

Boundedness

The discretized equations at each nodal point represent a set of algebraic equations that needs to be solved. Normally iterative numerical techniques are used to solve large equation sets. These methods start the solution process from a guessed distribution of the variable ϕ and perform successive updates until a converged solution is obtained. Scarborough (1958) has shown that a sufficient condition for a convergent iterative method can be expressed in terms of the values of the coefficients of the discretized equations:

$$\frac{\sum |a_{nb}|}{|a'_p|} = \begin{cases} \leq 1 & \text{at all nodes} \\ < 1 & \text{at least at one node.} \end{cases} \quad (3.22)$$

Here a'_p is the net coefficient of the central node P and a_{nb} is all the neighbouring nodes. If the differencing scheme produces coefficients that satisfy the above criterion the resulting matrix of coefficients is diagonally dominant. Diagonal

dominance is a desirable feature for satisfying the 'boundedness' criterion. This states that in the absence of sources the internal values of property ϕ should be bounded by its boundary values. Hence in a steady state conduction problem without sources and with boundary temperatures of 500°C and 200°C, all interior values of T should be less than 500°C and greater than 200°C. Another essential requirement for boundedness is that all coefficients of the discretized equations should have same sign. Physically this implies that an increase in the variable ϕ at one node should result in an increase in ϕ at neighbouring nodes.

Transportiveness

The transportiveness property of a fluid flow, Roache (1976), can be illustrated by considering the effect at a point P due to two constant sources of ϕ at nearby points W and E on either side, see Figure 3.3. We define the non-dimensional cell Peclet number as a measure of the relative strengths of convection and diffusion:

$$Pe = \frac{F}{D} = \frac{\rho u}{\Gamma/\delta x}, \quad (3.23)$$

where δx is the characteristic length (cell width) and Γ is the diffusion coefficient. Lets consider 2 cases.

- no convection and pure diffusion ($Pe \rightarrow 0$)
- no diffusion and pure convection ($Pe \rightarrow \infty$)

If we consider only pure diffusion the fluid is stagnant ($Pe \rightarrow 0$) and the contours of constant ϕ will be concentric circles centered around W and E . The result is that the point P is influenced equally of the two sources at W and E . However as Pe increases the contours change shape from circular to elliptical and are shifted in the direction of the flow. In the case of pure convection ($Pe \rightarrow \infty$) the elliptical contours are completely stretched out in the flow direction. All properties of ϕ emanating from sources at W and E is immediately transported downstream. Thus, conditions at P are now unaffected by the downstream source at E and completely dictated by the upstream source at W . Since there is no diffusion, ϕ_P is equal to ϕ_W . It is very important that the relationship between the directionality of influencing and the flow direction and magnitude of the Peclet number, known as the transportiveness, is born out in the discretization scheme.

3.4 Central differencing scheme

The central differencing approximation was used for the convection and diffusion problem. For a uniform grid we can write the cell face values of property ϕ as

$$\phi_e = \frac{\phi_P + \phi_E}{2}, \quad (3.24)$$

$$\phi_w = \frac{\phi_W + \phi_P}{2}. \quad (3.25)$$

Substitution of the above expressions into the convection terms of equation (3.20) yields

$$\frac{F_e}{2}(\phi_P + \phi_E) - \frac{F_w}{2}(\phi_W + \phi_P) = D_e(\phi_E - \phi_P) - D_w(\phi_P - \phi_W). \quad (3.26)$$

This can be rearranged to give

$$\left[\left(D_w - \frac{F_w}{2} \right) + \left(D_e + \frac{F_e}{2} \right) \right] \phi_P = \left(D_w + \frac{F_w}{2} \right) \phi_W + \left(D_e - \frac{F_e}{2} \right) \phi_E. \quad (3.27)$$

Identifying the coefficients of ϕ_W and ϕ_E as a_W and a_E , the central difference expressions for the discretized convection-diffusion equation are

$$a_P \phi_P = a_W \phi_W + a_E \phi_E, \quad (3.28)$$

where

$$a_W = D_w + \frac{F_w}{2}, \quad a_E = D_e - \frac{F_e}{2}, \quad a_P = a_W + a_E + (F_e - F_w). \quad (3.29)$$

The properties of the scheme will be discussed next.

Central differencing scheme properties

Conservativeness

The central differencing scheme uses consistent expressions to evaluate convection and diffusive fluxes at the control volume faces. The scheme is determined by only one function and is therefore conservative.

Boundedness

When we apply the discretized continuity equation (3.21) for a steady one dimensional flow field to the coefficients of equation (3.28), the expression for a_P becomes equal to $a_P = a_W + a_E$. The coefficients of the central difference scheme

satisfy the Scarborough criterion (3.22).

With $a_E = D_e - F_e/2$ the convective contribution to the east coefficient is negative; if the convection dominates it is possible for a_E to be negative. Given that $F_w > 0$ and $F_e > 0$ for a_E to be positive D_e and F_e must satisfy the following condition:

$$\frac{F_e}{D_e} = Pe_e < 2. \quad (3.30)$$

For a Pe larger than 2 the east coefficient will be negative. This violates one of the requirements for boundedness and may lead to physically impossible solutions.

Transportiveness

The central differencing scheme introduce influencing at node P from the directions of all its neighbours to calculate the convective and diffusive flux. Thus the scheme does not recognize the direction of the flow or the strength of convection relative to diffusion. It does not possess the transportiveness property at high Pe .

Accuracy

By using Taylor series we get a truncation error of second order, see Versteeg and Malasekera (2007).

3.5 Upwind differencing scheme

One of the major inadequacies with the central differencing scheme is its inability to identify flow direction. The value of property ϕ at a west cell face is always influenced by both ϕ_P and ϕ_W in central differencing. In a strongly convective flow from west to east, the above treatment is unsuitable because the west cell face should receive much stronger influencing from node W than from node P . The upwind differencing scheme takes into account the flow direction when determining the value at a cell face: the convected value of ϕ at a cell face is taken to be equal to the value at the upstream node. If the flow goes in the positive direction from west to east ($F_w > 0$, $F_e > 0$), the upwind scheme sets

$$\phi_w = \phi_W, \quad (3.31)$$

$$\phi_e = \phi_P, \quad (3.32)$$

and the discretized equation (3.20) becomes

$$F_e \phi_P - F_w \phi_W = D_e(\phi_E - \phi_P) - D_w(\phi_P - \phi_W), \quad (3.33)$$

which can be rearranged as

$$(D_w + D_e + F_e)\phi_P = (D_w + F_w)\phi_W + D_e\phi_E, \quad (3.34)$$

to give

$$[(D_w + F_w) + D_e + (F_e - F_w)]\phi_P = (D_w + F_w)\phi_W + D_e\phi_E. \quad (3.35)$$

Identifying the coefficients of ϕ_W and ϕ_E as a_W and a_E , equation (3.35) can be written in the usual general form

$$a_P\phi_P = a_W\phi_W + a_E\phi_E, \quad (3.36)$$

with central coefficient

$$a_P = a_W + a_E + (F_e - F_w),$$

and neighbour coefficients

$$a_W = D_w + F_w, \quad (3.37)$$

$$a_E = D_e. \quad (3.38)$$

When the flow is in the negative direction ($F_w < 0$, $F_e < 0$), the scheme takes

$$\phi_w = \phi_P, \quad (3.39)$$

$$\phi_e = \phi_E, \quad (3.40)$$

and the neighbour coefficients

$$a_W = D_w, \quad (3.41)$$

$$a_E = D_e - F_e. \quad (3.42)$$

Upwind differencing scheme properties

Conservativeness

The upwind differencing scheme utilizes consistent expressions to calculate fluxes through cell faces; therefore it can be easily shown that the formulation is conservative.

Boundedness

The coefficients of the discretized equation are always positive and satisfy the requirements for boundedness. When the flow satisfy the continuity term ($F_e - F_w$) in a_P is zero and gives $a_P = a_W + a_E$, which is desirable for stable iterative solutions. All the coefficients are positive and the coefficient matrix is diagonally dominant, hence no 'wiggles' occur in the solution.

Transportiveness

The scheme accounts for the direction of the flow so transportiveness is built into the formulation.

Accuracy

The scheme is based on the backward differencing formula so the accuracy is only of first order on the basis of the Taylor series truncation error, see Versteeg and Malasekera (2007).

3.6 The hybrid differencing scheme

The hybrid differencing scheme of Spalding (1976) is based on a combination of central and upwind differencing scheme. The hybrid difference scheme exploits the favourable properties of the upwind and central differencing schemes. It switches to upwind differencing when central differencing produce inaccurate results at high Pe numbers. The scheme is fully conservative and since the coefficients are always positive it is unconditionally bounded. It satisfies the transportiveness requirement by using an upwind formulation for large values of Peclet number. The scheme produces physically realistic solutions and is highly stable when compared with higher order schemes such as QUICK.

3.7 Quadratic upwind differencing scheme

The quadratic upstream interpolation for convective kinetics (QUICK) scheme of Leonard (1979) uses a three-point upstream-weighted quadratic interpolation for cell face values. The face value of ϕ is obtained from a quadratic function passing through two bracketing nodes, on each side of the face, and a node on the upstream side and is therefore conservative. Since the scheme is based on a quadratic function its accuracy in term of Taylor series truncation error is third order on a uniform mesh. The transportiveness property is built into the scheme as the quadratic function is based on two upstream and one downstream nodal values. The downside is that the QUICK scheme is only conditionally stable.

3.8 Total variation diminishing scheme

From the book of Versteeg and Malasekera (2007) we know that the upwind differencing scheme (UD) is the most stable scheme and does not give any wiggles,

whereas the central difference (CD) and quadratic upwind differencing schemes (QUICK) have higher order accuracy and give rise to wiggles under certain conditions. The goal is to find a scheme with higher order of accuracy without wiggles. This led to the development of TVD schemes with the desirable property for a stable, non-oscillatory and higher order scheme called monotonicity preserving. For a scheme to preserve monotonicity, (i) it must not create local extrema and (ii) the value of an existing local minimum must be non-decreasing and that of a local maximum must be non-increasing.

TVD schemes are generalizations of existing discretization schemes, like CD, UP and QUICK schemes under the necessary and sufficient condition for TVD schemes of Swedby (1984), so they inherently satisfy all the requirements of transportiveness, conservativeness and boundedness.

3.9 Pressure-Velocity Coupling

The convection of a scalar variable ϕ depends on the magnitude and direction of the local velocity field. In the previous sections we have assumed that the velocity field was known. In general the velocity field is not known and emerges as part of the overall solution process along with all other flow variables. In this section we will look at two of the most popular strategies of computing the entire flow field. The first is the SIMPLE algorithm, Semi-Implicit Method for Pressure-Linked Equations, originally put forward by Patankar and Spalding (1972) and is essentially a guess and correct procedure for the calculation of pressure. The second is the PISO algorithm, Pressure Implicit with Splitting of Operators, of Issa (1986). The PISO algorithm is a pressure-velocity calculation procedure developed originally for non-iterative computation of unsteady compressible flows. The algorithms will be outlined considering steady state for the SIMPLE algorithm and unsteady for the PISO algorithm. Further details of the algorithms can be found in the books of Versteeg and Malasekera (2007); Tu et al. (2007).

3.9.1 SIMPLE algorithm

The SIMPLE algorithm will be illustrated by considering a two dimensional laminar steady flow. To initiate the SIMPLE calculation process a pressure field p^* , where the star (*) denotes the guessed variable, is guessed which is used to solve discretized momentum equations

$$a_{i,j}u_{i,j}^* = \sum a_{nb}u_{nb}^* + (p_{I-1,j}^* - p_{I,j}^*)A_{i,j} + b_{i,j}, \quad (3.43)$$

$$a_{I,j}v_{I,j}^* = \sum a_{nb}v_{nb}^* + (p_{I,j-1}^* - p_{I,j}^*)A_{I,j} + b_{I,j}. \quad (3.44)$$

After the momentum equations is considered, the continuity equation is solved from which an equation for pressure correction p' is obtained.

$$\begin{aligned} a_{I,J}p'_{I,J} = & a_{I+1,J}p'_{I+1,J} + a_{I-1,J}p'_{I-1,J} \\ & + a_{I,J+1}p'_{I,J+1} + a_{I,J-1}p'_{I,J-1} + b'_{I,J}. \end{aligned} \quad (3.45)$$

Now correct pressure and velocities can be found

$$\begin{aligned} p_{i,j} &= p_{i,j}^* + p'_{i,j}, \\ u_{i,j} &= u_{i,j}^* + d_{i,j}(p'_{I-1,J} - p'_{I,J}), \\ v_{I,j} &= v_{I,j}^* + d_{I,j}(p'_{I,J-1} - p'_{I,J}). \end{aligned} \quad (3.46)$$

From the correct pressure and velocities all other discretized transport equations can be solved. The algorithm will run until the solution has converged. The sequence of operations in a CFD procedure which employs the SIMPLE algorithm is given in Figure 3.4.

3.9.2 PISO algorithm

The PISO algorithm involves one predictor step and two corrector steps and may be seen as an extension of SIMPLE, with a further corrector step to enhance it. The second pressure correction equation is

$$\begin{aligned} a_{I,J}p''_{I,J} = & a_{I+1,J}p''_{I+1,J} + a_{I-1,J}p''_{I-1,J} \\ & + a_{I,J+1}p''_{I,J+1} + a_{I,J-1}p''_{I,J-1} + b''_{I,J}. \end{aligned} \quad (3.47)$$

From equation (3.47) the pressure and velocity is corrected for the second time.

$$p_{I,J}^{***} = p_{I,J}^* + p'_{I,J} + p''_{I,J}, \quad (3.48)$$

$$\begin{aligned} u_{i,j}^{***} = & u_{i,j}^* + d_{i,j}(p'_{I-1,J} - p'_{I,J}) + \frac{\sum a_{nb}(u_{nb}^{**} - u_{nb}^*)}{a_{i,j}} \\ & + d_{i,j}(p''_{I-1,J} - p''_{I,J}), \end{aligned} \quad (3.49)$$

$$\begin{aligned} v_{I,j}^{***} = & v_{I,j}^* + d_{I,j}(p'_{I,J-1} - p'_{I,J}) + \frac{\sum a_{nb}(v_{nb}^{**} - v_{nb}^*)}{a_{I,j}} \\ & + d_{I,j}(p''_{I,J-1} - p''_{I,J}). \end{aligned} \quad (3.50)$$

The sequence of operations for an iterative steady state PISO calculation is given in Figure 3.5.

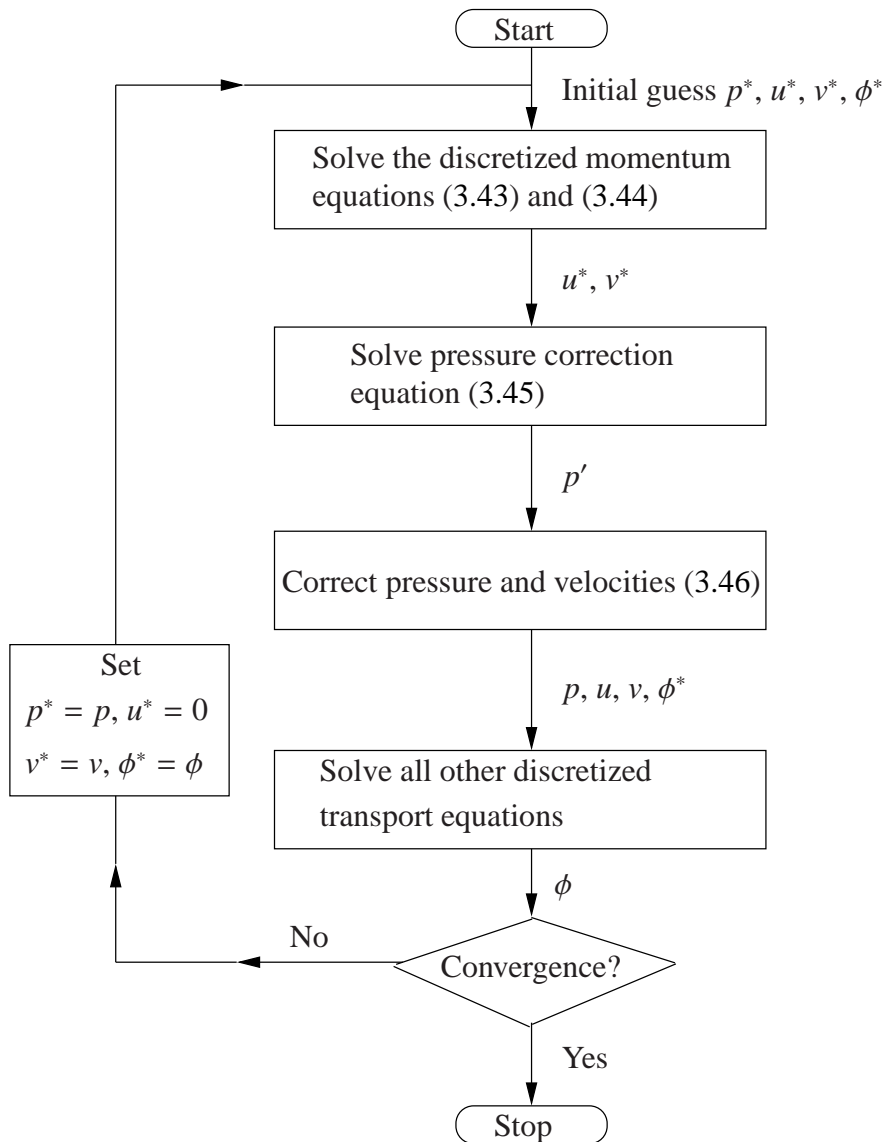


Figure 3.4: The SIMPLE algorithm.

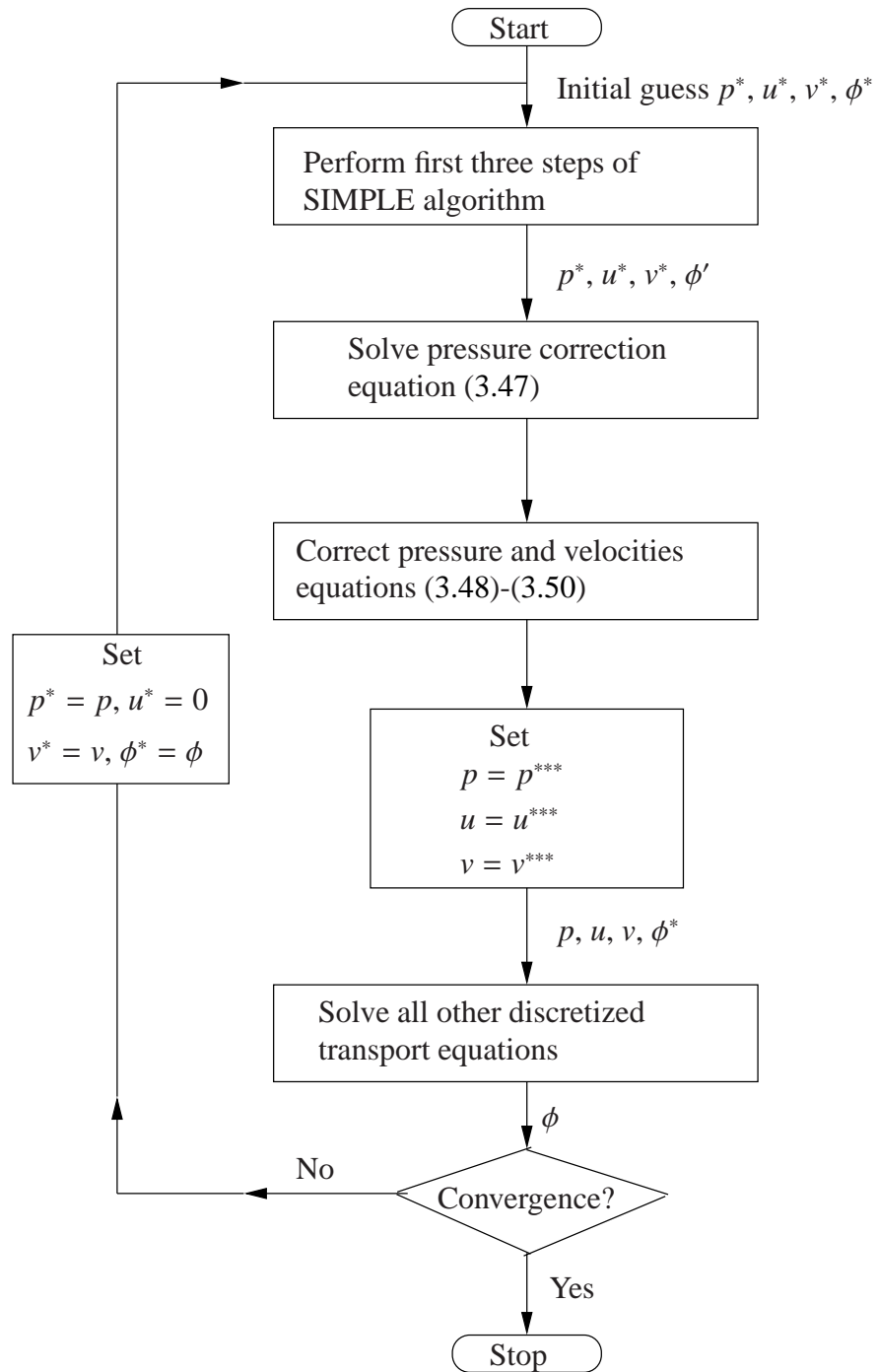


Figure 3.5: The PISO algorithm.

Chapter 4

Turbulence Modelling

4.1 Turbulent flow

In fluid dynamics, turbulence or turbulent flow do not allow a strict analytic study, and one depends heavily on physical intuition on dimensional arguments.

Before proceeding to the discussion of numerical methods for turbulent flows, it is useful to introduce a classification scheme for the approaches to predicting turbulent flows. According to Bardina et al. (1980) there are six categories, most of which can be divided in sub-categories. We will introduce the three most used categories.

- The first is based on equations obtained by averaging the equations of motion over time, over a coordinate in which the mean flow does not vary, or over an ensemble of realizations. This approach is called one-point closure and leads to a set of partial differential equations called the Reynolds-averaged Navier-Stokes (RANS) equations. These equations do not form a closed set so the method requires the introduction of approximations, turbulence models.
- The second is the large eddy simulation (LES) and solves for the largest scale motions of the flow while approximating or modelling only the small scale motions. It can be regarded as a kind of compromise between one point closure methods (RANS) and direct numerical simulation (DNS)
- The third is the direct numerical simulation (DNS) in which the Navier-Stokes equations are solved for all of the motions in a turbulent flow.

As one progresses down this list, more and more of the turbulent motions are computed and fewer are approximated by models. This makes the last methods

more exact, but the computation time is increased considerably. We are most interested in the quantitative properties, like pressure and forces on the hull, of the flow. Therefore we will use the RANS equations for the simulation in this thesis.

4.1.1 Reynolds-Averaged Navier-Stokes (RANS) Equations

In Reynolds-Averaged approaches to turbulence all the unsteadiness is averaged out, in other word all unsteadiness is regarded as part of the turbulence. On averaging, the non linearity of the Navier-stokes equations gives rise to terms that must be modelled. The complexity of turbulence makes it unlikely that any single Reynolds-averaged model will be able to represent all turbulent flows, so turbulence models should be regarded as engineering approximations rather than scientific laws, see Ferziger and Perić (2002). In the following sections the continuity, momentum and heat equation will be averaged by using the method in the book of Kundu and Cohen (2010).

Averages

Let $u(t)$ be any measured variable in a turbulent flow. Consider a case when the "average characteristics" of $u(t)$ do not vary with time. In such a case we can define the average variable as the time mean

$$\bar{u} \equiv \lim_{t_0 \rightarrow \infty} \frac{1}{t_0} \int_0^{t_0} u(t) dt. \quad (4.1)$$

A collection of experiments, performed under identical set of experimental conditions, is called ensemble, and an average over the collection is called an ensemble average, or expected value. The ensemble average of u at time t can be defined to be

$$\bar{u}(t) \equiv \frac{1}{N} \sum_{i=1}^N u^i(t), \quad (4.2)$$

where N is a large number and the i th record is denoted by $u^i(t)$. From this it follows that the average derivative at a certain time is

$$\begin{aligned} \overline{\frac{\partial u}{\partial t}} &= \frac{1}{N} \left[\frac{\partial u^1(t)}{\partial t} + \frac{\partial u^2(t)}{\partial t} + \frac{\partial u^3(t)}{\partial t} + \dots \right] \\ &= \frac{\partial}{\partial t} \left[\frac{1}{N} u^1(t) + u^2(t) + \dots \right] = \frac{\partial \bar{u}}{\partial t}. \end{aligned}$$

This shows that the operation of differentiation commutes with the operation of ensemble averaging, so that their orders can be interchanged. In a similar manner

we can therefore have the rules

$$\overline{\frac{\partial u}{\partial t}} = \frac{\partial \bar{u}}{\partial t}, \quad (4.3)$$

$$\overline{\int_a^b u dt} = \int_a^b \bar{u} dt. \quad (4.4)$$

Similar rules also hold when the variable is a function of space:

$$\overline{\frac{\partial u}{\partial x_i}} = \frac{\partial \bar{u}}{\partial x_i}, \quad (4.5)$$

$$\overline{\int_a^b u dx} = \int_a^b \bar{u} dx. \quad (4.6)$$

Averaged Equations of Motion

A turbulent flow instantaneously satisfies the Navier-Stokes equations. However, it is virtually impossible to predict the flow in detail. In this section we shall derive the equations of motion for the mean state in a turbulent flow and examine what effect the turbulent fluctuation may have on the mean flow. We assume that the density variations are caused by temperature fluctuations alone. Under the Boussinesq approximation, the equations of motion for the instantaneous variables are

$$\frac{\partial \tilde{u}_i}{\partial t} + \tilde{u}_j \frac{\partial \tilde{u}_i}{\partial x_j} = -\frac{1}{\rho_0} \frac{\partial \tilde{p}}{\partial x_i} - g[1 - \alpha(\tilde{T} - T_0)]\delta_{i3} + \nu \frac{\partial^2 \tilde{u}_i}{\partial x_j \partial x_j}, \quad (4.7)$$

$$\frac{\partial \tilde{u}_i}{\partial x_i} = 0, \quad (4.8)$$

$$\frac{\partial \tilde{T}}{\partial t} + \tilde{u}_j \frac{\partial \tilde{T}}{\partial x_j} = \kappa \frac{\partial^2 \tilde{T}}{\partial x_j \partial x_j}. \quad (4.9)$$

Instantaneous quantities are denoted by a tilde ($\tilde{}$). Let the variables be decomposed into their mean part and a deviation from the mean:

$$\begin{aligned} \tilde{u}_i &= U_i + u_i, \\ \tilde{p} &= P + p, \\ \tilde{T} &= \bar{T} + T'. \end{aligned} \quad (4.10)$$

(The corresponding density is $\tilde{\rho} = \bar{\rho} + \rho'$.) This is called the Reynolds decomposition. The mean velocity and the mean pressure are denoted by uppercase letters, and their turbulent fluctuations are denoted by lowercase letters. This convention is impossible to use for temperature and density, for which we use an overbar for

the mean state and a prime for the turbulent part. The mean quantities (U, P, \bar{T}) are to be regarded as ensemble averages; for stationary flows they can also be regarded as time averages. Taking the average of both sides of equation (4.10), we obtain

$$\bar{u}_i = \bar{p} = \bar{T}' = 0$$

showing that the fluctuations have zero mean.

The equations satisfied by the mean flow are obtained by substituting the Reynolds decomposition (4.10) into the instantaneous Navier-Stokes equations (4.7)-(4.9) and taking the average of the equations. The three equations transform as follows.

Mean Continuity Equation

Averaging the continuity equation (4.8), we obtain

$$\overline{\frac{\partial}{\partial x_i}(U_i + u_i)} = \frac{\partial U_i}{\partial x_i} + \frac{\partial \bar{u}_i}{\partial x_i} = \frac{\partial U_i}{\partial x_i} + \frac{\partial \bar{u}_i}{\partial x_i} = 0,$$

where we have used the commutation rule (4.5). Using $\bar{u}_i = 0$, we obtain

$$\frac{\partial U_i}{\partial x_i} = 0,$$

which is the continuity equation for the mean flow. Subtracting this from the continuity equation (4.8) for the total flow, we obtain

$$\frac{\partial u_i}{\partial x_i} = 0,$$

which is the continuity equation for the turbulent fluctuation field. It is therefore seen that the instantaneous, the mean, and the turbulent parts of the velocity field are all nondivergent.

Mean Momentum Equation

The momentum equation (4.7) gives

$$\begin{aligned} & \frac{\partial}{\partial t}(U_i + u_i) + (U_j + u_j) \frac{\partial}{\partial x_j}(U_i + u_i) \\ &= -\frac{1}{\rho_0} \frac{\partial}{\partial x_i}(P + p) - g[1 - \alpha(\bar{T} + T' - T_0)]\delta_{i3} + \nu \frac{\partial^2}{\partial x_j^2}(U_i + u_i). \end{aligned} \quad (4.11)$$

We shall take the average of each term of this equation. The average of the time derivative term is

$$\overline{\frac{\partial}{\partial t}(U_i + u_i)} = \frac{\partial U_i}{\partial t} + \frac{\partial \bar{u}_i}{\partial t} = \frac{\partial U_i}{\partial t} + \frac{\partial \bar{u}_i}{\partial t} = \frac{\partial U_i}{\partial t},$$

where we have used the commutation rule (4.3), and $\bar{u}_i = 0$. The average of the advective term is

$$\begin{aligned} \overline{(U_j + u_j) \frac{\partial}{\partial x_j} (U_i + u_i)} &= U_j \frac{\partial U_i}{\partial x_j} + U_j \frac{\partial \bar{u}_i}{\partial x_j} + \bar{u}_j \frac{\partial U_i}{\partial x_j} + \overline{u_j \frac{\partial u_i}{\partial x_j}} \\ &= U_j \frac{\partial U_i}{\partial x_j} + \frac{\partial}{\partial x_j} (\bar{u}_i \bar{u}_j), \end{aligned}$$

where we have used the commutation rule (4.5) and $\bar{u}_i = 0$; the continuity equation $\partial u_j / \partial x_j = 0$ has also been used in obtaining the last term.

The average of the pressure gradient term is

$$\overline{\frac{\partial}{\partial x_i} (P + p)} = \frac{\partial P}{\partial x_i} + \frac{\partial \bar{p}}{\partial x_i} = \frac{\partial P}{\partial x_i}.$$

The average of the gravity term is

$$\overline{g[1 - \alpha(\bar{T} + T' - T_0)]} = g[1 - \alpha(\bar{T} - T_0)],$$

where we have used $\bar{T}' = 0$. The average of the viscous term is

$$\overline{\nu \frac{\partial^2}{\partial x_j^2} (U_i + u_i)} = \nu \frac{\partial^2 U_i}{\partial x_j \partial x_j}.$$

Collecting terms, the mean of the momentum equation (4.11) takes the form

$$\frac{\partial U_i}{\partial t} + U_j \frac{\partial U_i}{\partial x_j} + \frac{\partial}{\partial x_j} (\bar{u}_i \bar{u}_j) = -\frac{1}{\rho_0} \frac{\partial P}{\partial x_i} - g[1 - \alpha(\bar{T} - T_0)] \delta_{i3} + \nu \frac{\partial^2 U_i}{\partial x_j \partial x_j}. \quad (4.12)$$

The correlation $\bar{u}_i \bar{u}_j$ in equation (4.12) is generally nonzero, although $\bar{u}_i = 0$. This is discussed forward in what follows.

Reynolds Stress

Writing the term $\overline{u_i u_j}$ on the right-side, the mean momentum equation (4.12) becomes

$$\frac{DU_i}{Dt} = -\frac{1}{\rho_0} \frac{\partial P}{\partial x_i} - g[1 - \alpha(\bar{T} - T_0)]\delta_{i3} + \frac{\partial}{\partial x_j} \left[\nu \frac{\partial U_i}{\partial x_j} - \overline{u_i u_j} \right],$$

which can be written as

$$\frac{DU_i}{Dt} = \frac{1}{\rho_0} \frac{\partial \bar{\tau}_{ij}}{\partial x_j} - g[1 - \alpha(\bar{T} - T_0)]\delta_{i3}, \quad (4.13)$$

where

$$\bar{\tau}_{ij} = -P\delta_{ij} + \mu \left(\frac{\partial U_i}{\partial x_j} + \frac{\partial U_j}{\partial x_i} \right) - \rho_0 \overline{u_i u_j}. \quad (4.14)$$

Then we compare equations (4.13) and (4.14) with the corresponding equations for the instantaneous flow, given by

$$\begin{aligned} \frac{D\tilde{u}_i}{Dt} &= \frac{1}{\rho_0} \frac{\partial \tilde{\tau}_{ij}}{\partial x_j} - g[1 - \alpha(\tilde{T} - T_0)]\delta_{i3}, \\ \tilde{\tau}_{ij} &= -\tilde{p}\delta_{ij} + \mu \left(\frac{\partial \tilde{u}_i}{\partial x_j} + \frac{\partial \tilde{u}_j}{\partial x_i} \right). \end{aligned}$$

It is seen from equation (4.13) that there is an additional stress $-\rho_0 \overline{u_i u_j}$ acting in a mean turbulent flow. In fact, these extra stresses on the mean field of a turbulent flow are much larger than the viscous contribution $\mu(\partial U_i/\partial x_j + \partial U_j/\partial x_i)$, except very close to a solid surface where the fluctuations are small and mean flow gradients are large.

The tensor $-\rho_0 \overline{u_i u_j}$ is called the Reynolds stress tensor and has the nine Cartesian components

$$\tau_t = \begin{pmatrix} -\rho_0 \overline{u^2} & -\rho_0 \overline{uv} & -\rho_0 \overline{uw} \\ -\rho_0 \overline{uv} & -\rho_0 \overline{v^2} & -\rho_0 \overline{vw} \\ -\rho_0 \overline{uw} & -\rho_0 \overline{vw} & -\rho_0 \overline{w^2} \end{pmatrix}. \quad (4.15)$$

This is a symmetric tensor; its diagonal components are normal stress, and the off-diagonal components are shear stresses. If the turbulent fluctuation are completely isotropic, that is, if they do not have any directional preference, then the off-diagonal components of $\overline{u_i u_j}$ vanish, and $\overline{u^2} = \overline{v^2} = \overline{w^2}$.

Mean Heat equation

The heat equation (4.9) is

$$\frac{\partial}{\partial t}(\bar{T} + T') + (U_j + u_j)\frac{\partial}{\partial x_j}(\bar{T} + T') = \kappa\frac{\partial^2}{\partial x_j^2}(\bar{T} + T').$$

The average of the time derivative term is

$$\overline{\frac{\partial}{\partial t}(\bar{T} + T')} = \frac{\partial \bar{T}}{\partial t} + \frac{\partial \bar{T}'}{\partial t} = \frac{\partial \bar{T}}{\partial t}.$$

The average of the advective term is

$$\begin{aligned} \overline{(U_j + u_j)\frac{\partial}{\partial x_j}(\bar{T} + T')} &= U_j\frac{\partial \bar{T}}{\partial x_j} + U_j\frac{\partial \bar{T}'}{\partial x_j} + \bar{u}_j\frac{\partial \bar{T}}{\partial x_j} + \overline{u_j\frac{\partial T'}{\partial x_j}} \\ &= U_j\frac{\partial \bar{T}}{\partial x_j} + \frac{\partial}{\partial x_j}(\overline{u_j T'}). \end{aligned}$$

The average of the diffusion term is

$$\overline{\frac{\partial^2}{\partial x_j^2}(\bar{T} + T')} = \frac{\partial^2 \bar{T}}{\partial x_j^2} + \frac{\partial^2 \bar{T}'}{\partial x_j^2} = \frac{\partial^2 \bar{T}}{\partial x_j^2}.$$

Collecting terms, the mean heat equation takes the form

$$\frac{\partial \bar{T}}{\partial t} + U_j\frac{\partial \bar{T}}{\partial x_j} + \frac{\partial}{\partial x_j}(\overline{u_j T'}) = \kappa\frac{\partial^2 \bar{T}}{\partial x_j^2},$$

which can be written as

$$\frac{D\bar{T}}{Dt} = \frac{\partial}{\partial x_j}\left(\kappa\frac{\partial \bar{T}}{\partial x_j} - \overline{u_j T'}\right). \quad (4.16)$$

Multiplying by $\rho_0 C_p$, we obtain

$$\rho_0 C_p \frac{D\bar{T}}{Dt} = -\frac{\partial Q_j}{\partial x_j}, \quad (4.17)$$

where the heat flux is given by

$$Q_j = -k\frac{\partial \bar{T}}{\partial x_j} + \rho_0 C_p \overline{u_j T'}, \quad (4.18)$$

and $k = \rho_0 C_p \kappa$ is the thermal conductivity. Equation (4.18) shows that the fluctuations cause an additional mean turbulent heat flux of $\rho_0 C_p \overline{\mathbf{u}T'}$, in addition to the molecular heat flux of $-k\nabla\bar{T}$. For example, the surface of the earth becomes hot during the day, resulting in a decrease of the mean temperature with height, and an associated turbulent convective motion. An upward fluctuating motion is then mostly associated with a positive temperature fluctuation, giving rise to an upward heat flux $\rho_0 C_p \overline{wT'} > 0$.

4.2 Turbulence Models

To obtain the Reynolds-Averaged Navier-Stokes (RANS) equations, we have used the Navier-Stokes equations for the instantaneous velocity and pressure fields are decomposed into a mean value and a fluctuating component. The resulting equations for the mean quantities are essentially identical to the original equations, except that an additional Reynolds stress tensor, see equation (4.15), now appears in the momentum transport equation.

The challenge is thus to model the Reynolds stress tensor τ_i in terms of the mean flow quantities, and hence provide closure of the governing equations. A basic approach that is used is the

- eddy viscosity models.

It is widely acknowledged that turbulence models are inexact representations of the physical phenomena being modelled, and no single turbulence model is the best for every flow simulation. Consequently, it is necessary to provide a suite of models that reflect the current state of the art.

By using the notation of the book of Ferziger and Perić (2002) the averaged continuity and momentum equation can, for incompressible flows without body forces, be written in tensor notation and Cartesian coordinates as:

$$\frac{\partial(\rho\bar{u}_i)}{\partial x_i} = 0, \quad (4.19)$$

$$\frac{\partial(\rho\bar{u}_i)}{\partial t} + \frac{\partial}{\partial x_j} \left(\rho\bar{u}_i\bar{u}_j + \overline{\rho u'_i u'_j} \right) = -\frac{\partial\bar{p}}{\partial x_i} + \frac{\partial\bar{\tau}_{ij}}{\partial x_j}, \quad (4.20)$$

where overbar is the time averaged value and fluctuation denoted with (') and where the $\bar{\tau}_{ij}$ are the mean viscous stress tensor components:

$$\bar{\tau}_{ij} = \mu \left(\frac{\partial \bar{u}_i}{\partial x_j} + \frac{\partial \bar{u}_j}{\partial x_i} \right). \quad (4.21)$$

Finally the equation for the mean of a scalar quantity can be written:

$$\frac{\partial(\rho\bar{\phi})}{\partial t} + \frac{\partial}{\partial x_j} \left(\rho\bar{u}_j\bar{\phi} + \overline{\rho u'_j\phi'} \right) = \frac{\partial}{\partial x_j} \left(\Gamma \frac{\partial \bar{\phi}}{\partial x_j} \right). \quad (4.22)$$

4.2.1 The k-epsilon turbulence model

To close the set of equations we have to introduce a turbulence model. To see what a reasonable model might be, we note, that in laminar flows, energy dissipation and transport of mass, momentum and energy normal to the streamlines are mediated by the viscosity, so it is natural to assume that the effect of turbulence can be represented as an increased viscosity. This leads to the eddy-viscosity model for the Reynolds stress:

$$-\overline{\rho u'_i u'_j} = \mu_t \left(\frac{\partial \bar{u}_i}{\partial x_j} + \frac{\partial \bar{u}_j}{\partial x_i} \right) - \frac{2}{3} \rho \delta_{ij} k, \quad (4.23)$$

and the eddy-diffusion model for a scalar:

$$-\overline{\rho u'_j \phi'} = \Gamma_t \frac{\partial \bar{\phi}}{\partial x_j}. \quad (4.24)$$

In equation (4.23), k is the turbulent kinetic energy:

$$k = \frac{1}{2} \overline{u'_i u'_i} = \frac{1}{2} (\overline{u'_x u'_x} + \overline{u'_y u'_y} + \overline{u'_z u'_z}). \quad (4.25)$$

The transport equation for k is derived in the book of Wilcox (2006) and continue as follows:

$$\frac{\partial(\rho k)}{\partial t} + \frac{\partial(\rho \bar{u}_j k)}{\partial x_j} = \frac{\partial}{\partial x_j} \left(\mu \frac{\partial k}{\partial x_j} \right) - \frac{\partial}{\partial x_j} \left(\frac{\rho}{2} \overline{u'_j u'_i u'_i} + \overline{p' u'_j} \right) - \overline{\rho u_i u'_j} \frac{\partial \bar{u}_i}{\partial x_j} - \mu \frac{\partial u'_i}{\partial x_k} \frac{\partial u'_i}{\partial x_k}. \quad (4.26)$$

and the transport equation for ϵ is

$$\frac{\partial(\rho \epsilon)}{\partial t} + \frac{\partial(\rho u_j \epsilon)}{\partial x_j} = C_{\epsilon 1} P_k \frac{\epsilon}{k} - \rho C_{\epsilon 2} \frac{\epsilon^2}{k} + \frac{\partial}{\partial x_j} \left(\frac{\mu_t}{\sigma_\epsilon} \frac{\partial \epsilon}{\partial x_j} \right). \quad (4.27)$$

In this model, the eddy viscosity is expressed as:

$$\mu_t = \rho C_\mu \frac{k^2}{\epsilon}. \quad (4.28)$$

This k-epsilon model is based on equation (4.26) and (4.27) and contains five parameters; the most commonly used values for them are:

$$C_\mu = 0.09, \quad C_{\epsilon 1} = 1.44, \quad C_{\epsilon 2} = 1.92, \quad \sigma_k = 1.0, \quad \sigma_\epsilon = 1.3. \quad (4.29)$$

4.2.2 The k-omega turbulence model

The second most used commonly used model is the k-omega model, originally introduced by Saffman but popularized by Wilcox. The k-omega model uses the turbulent kinetic energy equation (4.26) but it has to be modified a bit:

$$\frac{\partial(\rho k)}{\partial t} + \frac{\partial(\rho \bar{u}_j k)}{\partial x_j} = P_k - \rho \beta^* k \omega + \frac{\partial}{\partial x_j} \left[\left(\mu + \frac{\mu_t}{\sigma_k^*} \right) \frac{\partial \omega}{\partial x_j} \right]. \quad (4.30)$$

The ω equation as given by Wilcox (2006) is:

$$\frac{\partial(\rho \omega)}{\partial t} + \frac{\partial(\rho \bar{u}_j \omega)}{\partial x_j} = \alpha \frac{\omega}{k} P_k - \rho \beta \omega^2 + \frac{\partial}{\partial x_j} \left[\left(\mu + \frac{\mu_t}{\sigma_\omega^*} \right) \frac{\partial \omega}{\partial x_j} \right], \quad (4.31)$$

where the eddy viscosity is expressed as:

$$\mu_t = \rho \frac{k}{\omega}. \quad (4.32)$$

The coefficients that go into this model are:

$$\alpha = \frac{5}{9}, \quad \beta = 0.075, \quad \beta^* = 0.09, \quad \sigma_k^* = \sigma_\omega^* = 2, \quad \epsilon = \beta^* \omega k. \quad (4.33)$$

The numerical behavior of this model is similar to that the k-epsilon model.

Chapter 5

Simulation set-up in STAR-CCM+

In this chapter we develop the simulation set-up. In the simulation we will use the computational fluid dynamic(CFD) simulation tool STAR-CCM+. The simulation is done on a SWATH wind turbine service vessel designed by Danish Yachts. We would like to find the resistance of the vessel as it moves in still water at the speed 8-24 knots.

In the following sections theory of the different tools and concepts used in STAR-CCM+, will be presented in addition to the set-up for the still water performance simulation.

5.1 Introduction

STAR-CCM+ is based on object-oriented programming technology. It is specifically designed to handle large models quickly and efficiently using a client-server architecture that meshes and solves and post-processes. The object-oriented nature of the code can be seen in a user interface. An object tree is provided for the simulation, containing object representations of all the data associated with the simulation. STAR-CCM+ also provides us with a user guide, see CD-adapco (2011).

5.2 3D-CAD Modeller

We start with the 3D-CAD modeller which is a feature-based parametric solid modeller within STAR-CCM+ that allows geometry to be built from scratch. The geometry created with 3D-CAD is stored as 3D-CAD models called bodies, which can subsequently be converting to geometry parts for integration with the meshing

and simulation process. The bodies represent the individual solid objects that make up the 3D-CAD model. In our case we already have a 3D-CAD geometry of the vessel, see Figure 5.1. The 3D-CAD geometry can be imported to STAR-CCM+ and modified afterwards.

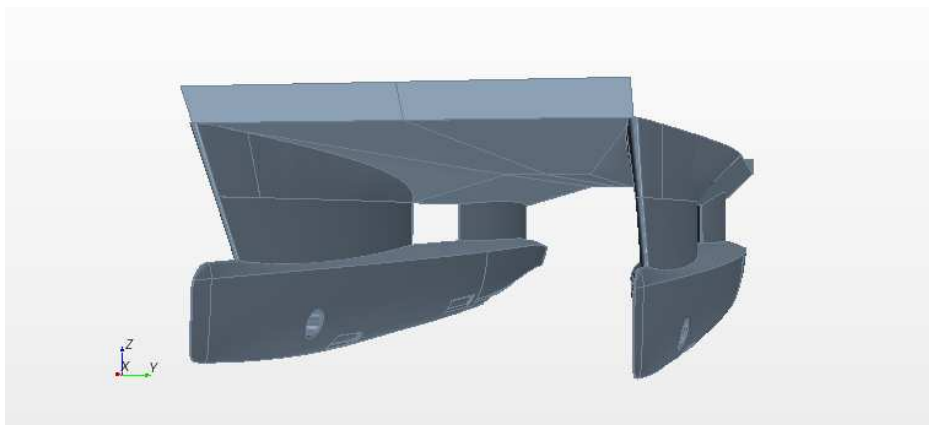


Figure 5.1: The SWATH(Small Waterplane Area Twin Hull) Wind turbine Service Vessel.

The dimensions of the twin hull are given in Table 5.1 below. The twin hull is 24.000 meter long, 10.600 meter wide and the height is 5.380 meter.

Coordinate	Corner 1 (meter)	Corner 2 (meter)
x	0	24
y	-5.29997406	5.29997406
z	0	5.37993214

Table 5.1: Dimensions of the twin hull.

As we are restricted to only use one processor for the simulation we would like to simulate the twin hull by using one of the hulls and a symmetry plane. The symmetry plane will maintain some of the physical effects the hulls have on each other and reduce the simulation domain and the simulation time, due to smaller mesh.

The coordinate system is fixed in the middle of the twin hull where $z = 0$ is the bottom of the twin hull and the direction of heave, $x = 0$ is located at the end of the stern and is the direction of surge and $y = 0$ is in the middle of the hull and is the direction of sway.

First one of the hulls is extruded away by using the $x - z$ plane at $y = 0$, which is the symmetry plane of the twin hull. Secondly the top of the twin hull from $z = 3.4$ is extruded away by using the $x - y$ plane at $z = 3.4$, see Figure 5.2.

The dimensions of the hull are given in Table 5.2. The width of one hull is 2.694 meter and the height is 3.400 meter.

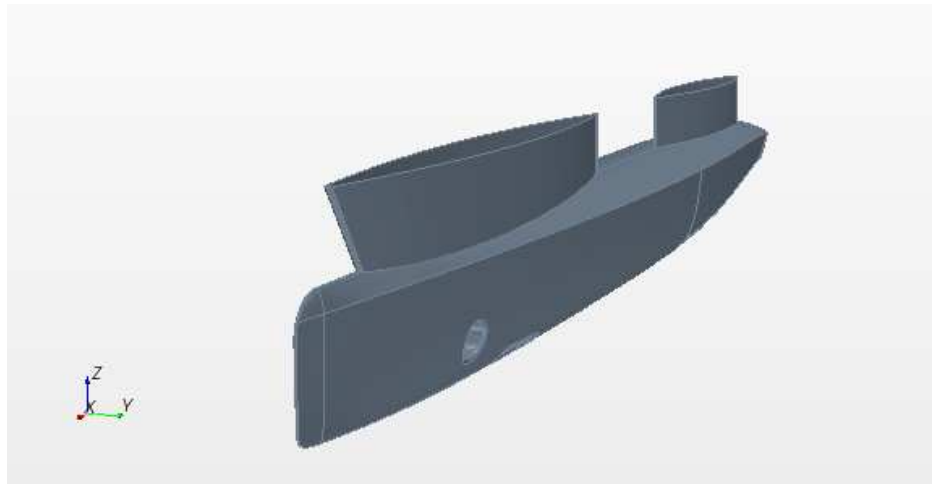


Figure 5.2: One hull of the SWATH wind turbine service vessel.

Coordinate	Corner 1 (meter)	Corner 2 (meter)
x	0	24
y	2.60611722	5.29997406
z	0	3.4

Table 5.2: Dimensions of the hull.

As we did the first 3D-CAD geometry importation of the 3D-CAD IGES file, some of the bodies were missing. The bodies were manually redrawn and used in the simulation work. After some discussion with CD-adapco, the producer of STAR-CCM+, we found that there were some problems with the 3D-CAD IGES-importer for the STAR-CCM+ version 7. The problems were resolved by using an earlier version of Star-CCM+. Version 6 was suitable for solving the problems with the 3D-CAD importation. After a successful 3D-CAD importation, the work could continue.

5.3 Geometry part

After the 3D-CAD model bodies are created from the CAD importation and the two extrudes, the next step is to convert the 3D-CAD bodies to geometry parts. A geometry part represents an object or collection of objects that can be used as the input geometry for the meshing tools. Each geometry part has a surface. The surface can be split by patch into several surfaces. This is done for the hull because we want different meshing set-ups for the different surfaces. The surfaces will be presented later, after the surfaces have been converted to boundaries, in Table 5.4 and Figure 5.7.

In this section we also specify the simulation domain. We will use the same sea level as in the still water performance test, $z = 2.525$, done by Force Technology, called SWATH mode. We specify one domain for the water and one for air by creating 2 blocks surrounding the hull and that coincides at sea level.

The block for the air coincides with the top of the hull at $z = 3.4$ providing closure of the hull geometry. The second block with water coincides with the sea level $z = 2.525$ and continue in the negative direction $z < 2.525$. After several simulations, by looking at boundary effects in the solutions and increasing the blocks sizes until the we get small contribution from the boundaries, we end up with the dimensions given in Table 5.3. The blocks are 54 meter long and 15 meter wide. The total height of the blocks is 16.4 meter.

Coordinate	Corner 1 (meter)	Corner 2 (meter)
Water		
x	-20	34
y	0	15
z	-13	2.525
Air		
x	-20	34
y	0	15
z	2.525	3.4

Table 5.3: Dimensions of water and air blocks.

The dimensions of the simulation domain, seen from the side and the front, are shown in the Figures 5.3 and 5.4.

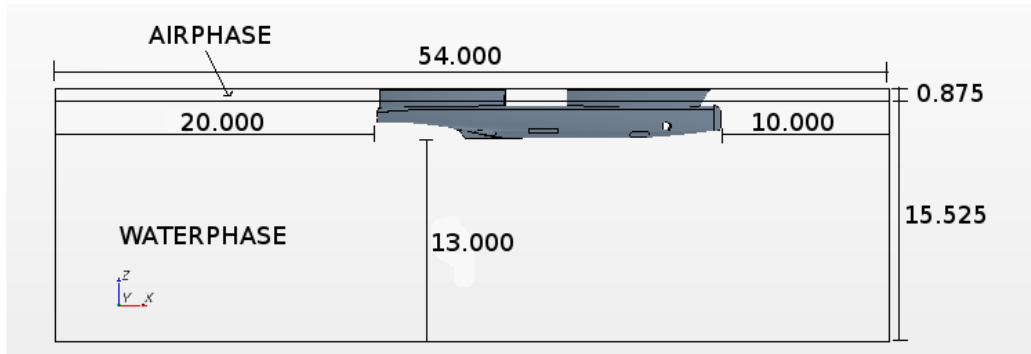


Figure 5.3: Dimensions of the simulation domain seen from the side.

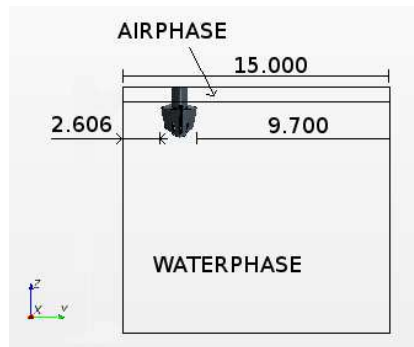


Figure 5.4: Dimensions of the simulation domain seen from the front.

Before we can convert the geometry parts to regions and specify the boundary conditions, the blocks must be split by patch from one surface for each block to six surfaces. We are only able to make one boundary condition per surface. The two surfaces that coincide at sea level are deleted, since the free surface is specified in the physics models. To the end the hull and the two blocks with 5 surfaces each are assigned to one region.

5.4 Region and boundaries

The regions are volume domains in space that are completely surrounded by boundaries. They are not necessarily contiguous, and are discretized by a conformal mesh consisting of connected faces, cells and vertices. As the hull and the 2 blocks have been assigned to one region for all parts and one boundary per part surface, the next step is to define the boundaries, see Figure 5.5. STAR-CCM+ provides us with the following boundaries for our problem:

- Flow-Split Outlet
- Mass flow Outlet
- Overset Mesh
- Pressure Outlet
- Stagnation Inlet
- Symmetry Plane
- Velocity Inlet
- Wall

The boundaries of the hull are defined as wall with no slip condition.

The next step is to define the boundaries of two blocks. Water.Inlet and Air.Inlet are defined as velocity inlet. Water.Outlet and Air.Outlet are defined as pressure outlet. Water.Symmetry and Air.Symmetry are defined as symmetry plane. Water.Side and Water.Bottom are defined as wall with no slip condition. Air.Side and Air.Top are defined as wall with slip condition.

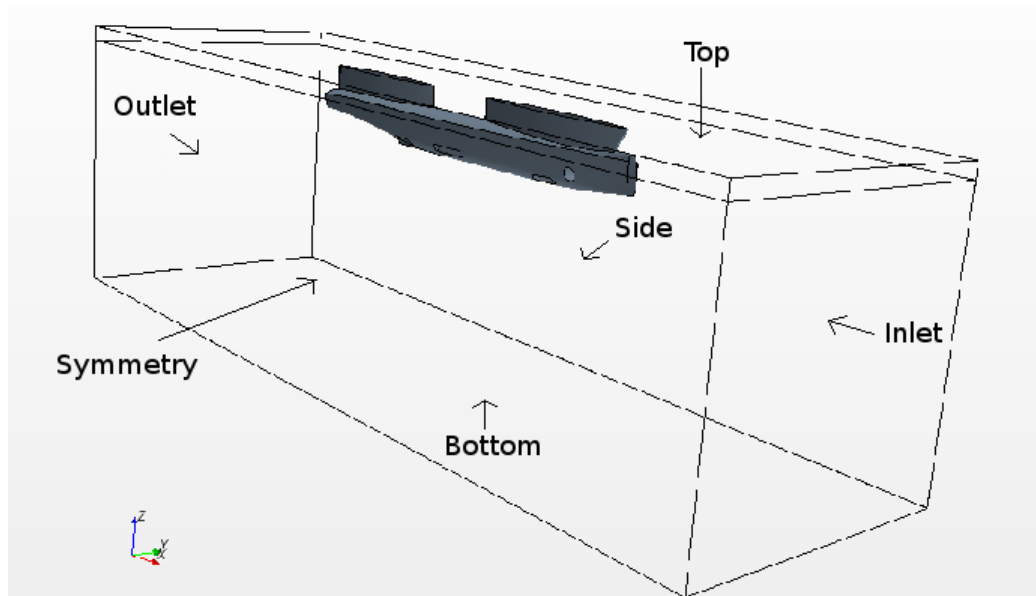


Figure 5.5: Boundaries of the two blocks.

5.5 Surface mesh

After the boundaries are specified, the next step is to create a surface mesh. A surface mesh is a discrete representation of the geometry of the individual regions that will be used for the volume mesh generation. It is made of faces and vertices.

The majority of the time spent in industry on a CFD project, is usually devoted to successfully generating a mesh for the domain geometry and is one of the most important steps during pre-process stage after the definition of the domain geometry, see Tu et al. (2007).

Ideally, the surface mesh should have the following properties:

- Closed - Contains no free edges or mismatches.
- Manifold - Edges are shared between no more than two triangles.
- Non-intersecting - The surface does not self-intersect.

The quality of triangle faces is also important. The surface should ideally contain:

- Equilateral sized triangles.
- Gradual variation in triangle size from one to the next.
- No sharp angles/surface folds etc. within the triangle proximity sphere.

STAR-CCM+ provides us with two different surface meshing types:

Surface remesher The surface remesher is used to re-triangulate an existing surface in order to improve the overall quality of the surface and optimize it for the volume mesh models.

Surface wrapper The surface wrapper can be used to provide a closed, manifold, non-intersecting surface when starting from poor quality CAD data. It is typically used when the imported surface includes problems such as:

- Multiple intersecting parts
- Missing data in the form of holes and gaps
- Surface mismatches
- Double and internal surfaces
- Overly complex geometry with too much detail

In the start of the surface mesh process, we give all the boundaries shown in Figure 5.7 a mesh set-up as shown in Table 5.4. Afterwards the surface mesher is chosen.

To obtain the best surface mesh for our analysis, we use the surface remesher, chosen in the mesh continua set-up, with a base size of 0.05 meter. After the mesh is created, we must check the quality of the surface. For this task we use the surface repair tool to run a diagnostic of the mesh. The mesh is checked for pierced faces, poor quality faces, close proximity faces, free edges and non-manifold vertices.

The mesh set-up gives several thousands of poor quality faces, close proximity faces and free edges. By using the auto-repair tool, we are able to repair face quality, face proximity and self-intersections, but not the free edges. The free edges must be fixed manually. This is a job too large to handle.

It seems like STAR-CCM+ is not able to read the 3D-CAD geometry for the imported 3D-CAD twin hull file. A solution to the problem is to consider the definition of the geometry parts. Each part should have a geometrical volume, not just a surface. When converting the 3D-CAD geometry bodies to geometrical parts, this problem might occur. Therefore we will try to combine all the parts to one part by using imprint, to ensure that the interfaces between the parts are created correctly with the result of no free edges. This procedure was attempted with the base size of 0.1, 0.05, 0.02 and 0,01 meter. Unfortunately we still got a lot of free edges.

Therefore we will do a new attempt by using the surface wrapper tool, and a base size of 0.05 meter. With this meshing set-up we did not get free edges, but only poor quality faces and close proximity faces that can be repaired with the auto-repair tool. Unfortunately the mesh was far from equal to the 3D-CAD geometry. This is the problem with the surface wrapper.

We had to do the same process with a lower base size. After several increases of the mesh resolution we get a suitable mesh with a base size equal 0.01 meter and over 500 000 faces. This resulted in over 20 millions cells as we make the volume mesh. A cell number under one million is desirable. The solution is to define an appropriate surface mesh size for each boundary of the region by adjusting the relative minimum size and relative target size. The sizes are defined as percentage of base size.

For obtaining a desirable surface mesh we must try several meshing set-up. We start with low resolution for each boundary and create the surface mesh and the volume mesh. After several attempts we get a useful surface mesh with a good resolution at the critical places, see Figure 5.6. The base size is set to 0.6 meter and the meshing set-up for each boundary is given below in Table 5.4. Some of the boundaries are shown in Figure 5.7. There are still some faces that do not match the 3D-CAD geometry, but the surface mesh with 122846 faces is considered good enough for modelling the physics of our problem.

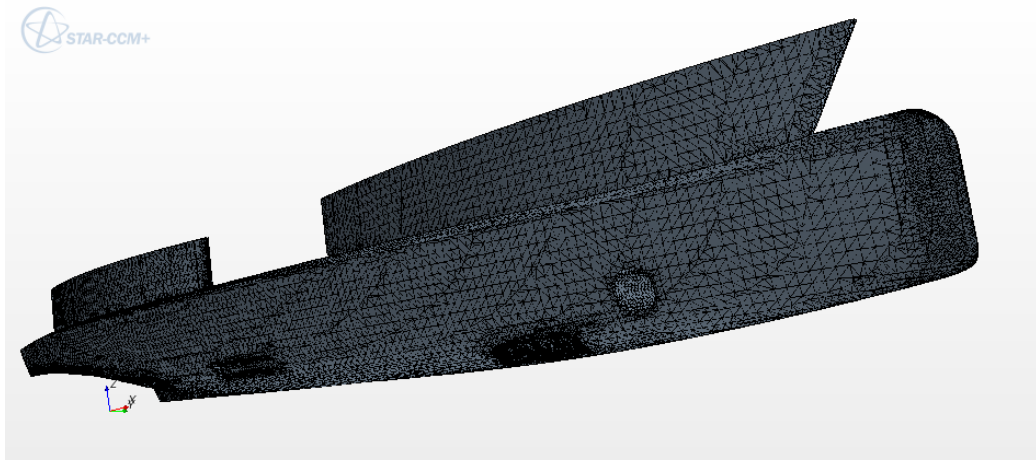


Figure 5.6: The surface mesh of the hull.

Boundary	Relative minimum size Percentage of Base	Relative target size Percentage of Base
Base size 0.6 meter		
Fin.Shell	5	10
Hull.Bau	2.5	5
Hull.HoleBackInside	5	10
Hull.HoleBackOutside	5	10
Hull.HoleFrontInside	2.5	5
Hull.HoleFrontOutside	2.5	5
Hull.HullSideBottom	7.5	30
Hull.HoleSide	5	20
Hull.HullTop	10	30
Hull.Tunnel	12.5	50
Air.Inlet	10	20
Air.Outlet	10	20
Air.Side	100	200
Air.Symmetry	10	20
Air.Top	30	50
TopBracketBack.TopBracketBack	10	30
TopBracketBack.TopBracketBackAngle	5	10
TopBracketFront.TopBracketFront	10	30
TopBracketFront.TopBracketFrontAngle	2.5	10
Water.Bottom	100	200
Water.Inlet	10	20
Water.Outlet	10	20
Water.Side	100	200
Water.Symmetry	10	20

Table 5.4: Boundary mesh set-up.

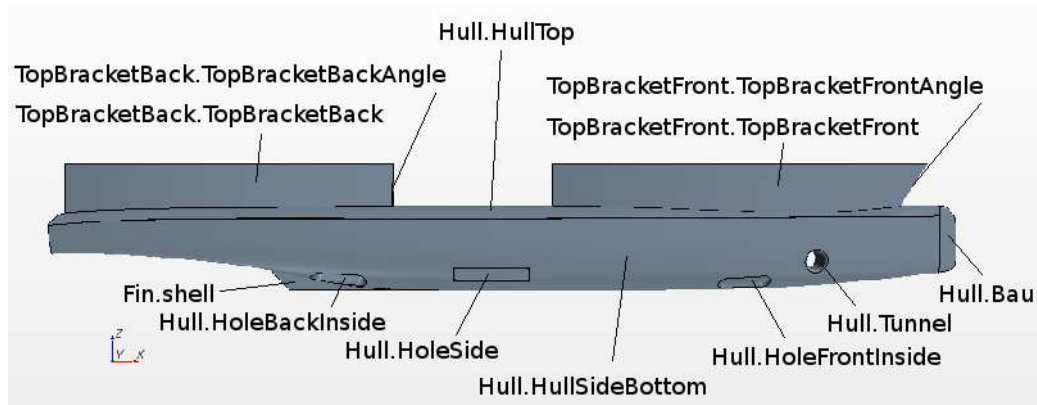
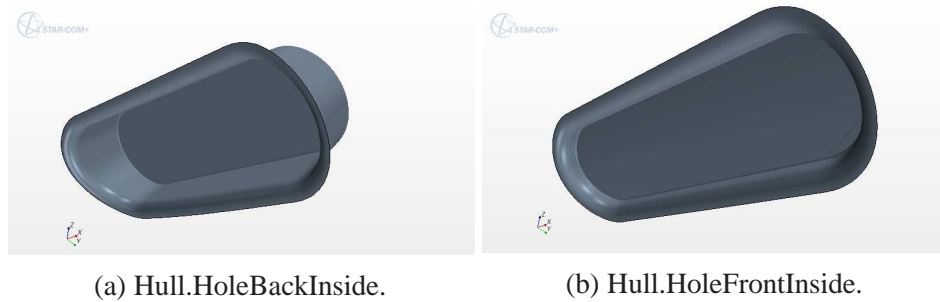


Figure 5.7: Boundaries of the hull. Not all boundaries are shown.



(a) Hull.HoleBackInside.

(b) Hull.HoleFrontInside.

Figure 5.8: The boundaries of the holes on the inside of the hull.

The faces that do not match the 3D-CAD model might affect the solution. We have some small bad faces in the four holes and also at the Fin.shell boundary, see Figure 5.9. We have tried to reduce the bad faces by using a higher resolution for the mesh at these areas, but we get even more bad faces for higher resolutions. The bad faces can be fixed manually, but there is too many of them. Therefore we will continue the simulation with these faces.

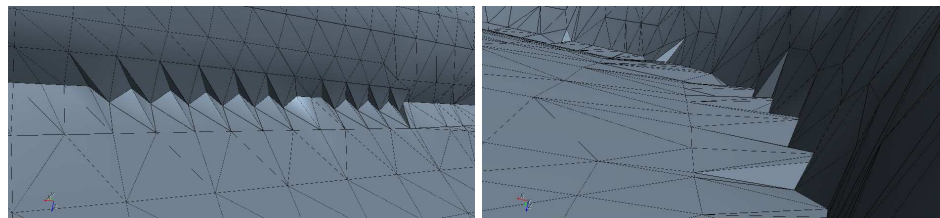


Figure 5.9: Bad surface mesh of Hull.HoleBackInside.

5.6 Volume mesh

After the surface mesh is created, the volume mesh can be created for the simulation domain. The volume mesh is the mathematical description of the space or geometry of the problem being solved. It is in turn constructed of the following mesh entities: vertices, faces and cells.

In order to generate the volume mesh, the following steps are followed:

1. Prepare the surface mesh according the requirements for STAR-CCM+.
2. Select the desired volume mesh model and the optional prism layer model, extruder model and/or generalized cylinder model.
3. Input the appropriate meshing values for the selected models.
4. Launch the volume mesh generator.
5. Visualize the volume mesh representation and check the mesh quality statistics.
6. Remove any invalid cells if they exist.
7. Continue with the simulation set-up.

The surface mesh is already made according to the requirements for STAR-CCM+. Therefore the next step is to select a volume mesh model. In STAR-CCM+ we have four different types:

- tetrahedral mesher;
- polyhedral mesher;
- trimmer;
- thin mesher

The polyhedral mesher and the trimmer are the most suitable volume meshers for our problem. In the simulation we will use the polyhedral mesher. The polyhedral cells created typically have an average of 14 cell faces. The polyhedral core mesh density can be increased or decreased by using the volume mesh density factors. Volumetric controls can also be included to locally increase or decrease the mesh density based on a range of prescribed shapes. For the first volume mesh the values are set to default.

The prism layer mesh model is also used in conjunction with a core volume mesh to generate orthogonal prismatic cells next to wall boundaries. This layer of cells is necessary to improve the accuracy of the flow solution. A prism layer is defined in terms of its thickness, the number of cell layers within it, the size distribution of the layers, and the function used to generate the distribution. The prism layer mesh model is set to default with two prism layer.

The volume mesh could now be generated. The first time we got a mesh with very large resolution, small cells near the surface of the hull and slightly larger further out. The high resolution will result in long computational time for the simulation. After having adjusted the meshing set-up of the surface mesh several times, mainly decreasing the mesh resolution at the boundaries Air.Side, Water.side and Water.Bottom and increasing the resolution for the Air.Top boundary, we obtain a mesh with a good resolution near the hull and increasing cell size near the boundaries of the blocks with water and air.

The volume mesh is still not suitable for our problem. We still need a good resolution of the mesh at the free surface. This is hardly done without affecting the rest of the mesh. Prism layers will give a better mesh at sea level than the polyhedral cells where some of the cells stretches over the sea level and other below. This can create mixing of the two phases. The problem is solved by defining several prism layers from the Air.Top boundary stretching under sea level.

The prism layers should travel at the same height from the inlet to outlet starting and ending at the same height. In STAR-CCM+ the prism layers are generated with respect to other nearby boundaries. Therefore the prism layers start from the intersection of the Air.Top plane and Air.Inlet and continue downwards crossing the water level, see Figure 5.10 and 5.11. Different prism layer set-up have been attempted, but without removing this effect. The prism layer set-up is given in Table 5.5.

The meshing process is a major part of the CFD simulation and is up to the skills of the CFD user to design a mesh that is a suitable compromise between the desired accuracy and solution cost, see Tu et al. (2007). For our simulation the final mesh quality is satisfying and no invalid cells have been found. The simulation is ready for analysis and the models and solvers for the problem are defined in the next sections.

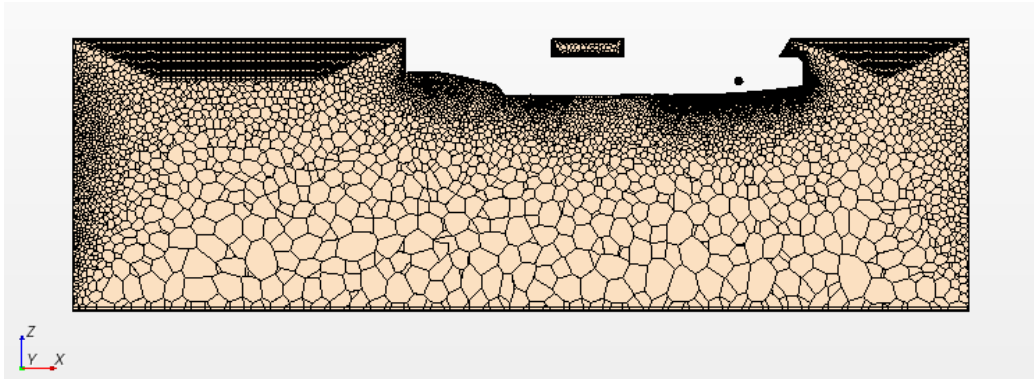


Figure 5.10: Volume mesh at cross section in the middle of the hull.

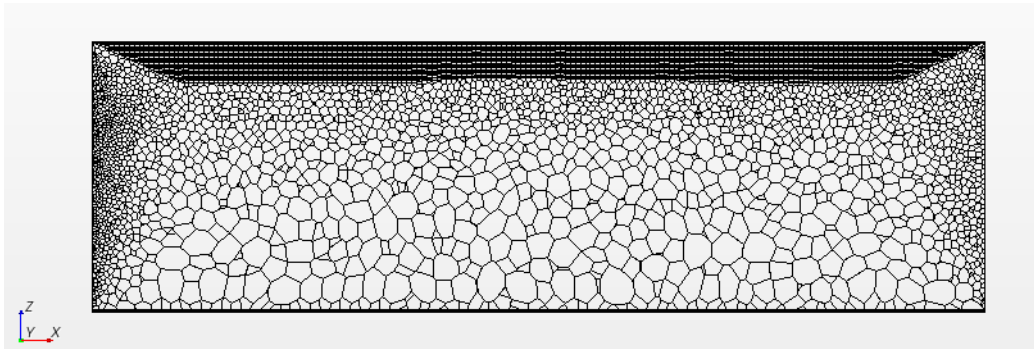


Figure 5.11: Volume mesh at cross section outside the hull.

Boundary	Number of prism layers	Prism layer stretching (ratio)	Prism layer thickness
Air.Top	50	1	Absolute size: 10 meter
All other	Default:2	Default:1.5	Default: 33% of base

Table 5.5: Prism layer mesh set-up.

5.7 Physics models

In this section the physics set-up for our problem is defined. The physics continuum contains a selection of physics models, such as a chosen flow solver, material models, steady or transient time model, a turbulence model and so on. Each

physics continuum represents a single substance that will be present in all regions to which the physics continuum applies.

A physics model in STAR-CCM+ defines how a physical phenomenon in a continuum is represented. Essentially, physics models define the primary variables of the simulation such as pressure, temperature and velocity and what mathematical formulation will be used to generate the solution.

In situations where transport equations are required, the model will provide these equations to the solvers. This means that model properties will often include coefficients relevant to the transport equations, as well as parameters relevant to the discretization approach.

Physics models used in the simulation

In this section the different physics models for the problem is chosen and described. A summary of the physics models for our problem is given in Table 5.6.

In the start of the model selection we choose a Space model. The following models are provided: Axisymmetric, Shell three dimensional, Three dimensional and two dimensional. The Three dimensional model is suitable for our problem. In addition the Gradients model is chosen automatically.

Next we are asked to choose a Time model. The following models are provided: Explicit unsteady, Harmonic balance, Implicit unsteady and Steady. The Implicit unsteady model is most suitable for our problem. The Steady model was tried first, but with the result of divergence.

Further we choose a Material model. The following models are provided: Gas, Liquid, Solid, Multi-component gas, Multi-component liquid and Multiphase mixture. The Multiphase mixture model is chosen for simulating the water and air phases. In addition the Multiphase interaction and Eulerian multiphase model are chosen automatically.

Next we must specify our viscous regime model. The following models are provided: Inviscid, Laminar and Turbulent. We have a turbulent flow, therefore the Turbulent model is chosen for the viscous regime.

Next we choose the Turbulence model. The following models are provided: The Detached Eddy Simulation (DNS), Large Eddy Simulation (LES) and the Reynolds-Averaged Navier-Stokes (RANS). The Reynolds-Averaged Navier-Stokes

model is chosen.

After having specified a turbulent flow we must choose which Reynolds-Averaged turbulence model we would like to use. The following models are provided: K-epsilon turbulence, K-omega turbulence, Reynolds stress turbulence and Spalart-Allmaras turbulence. After recommendation of Wilcox, see Wilcox (2006), we choose the K-omega turbulence model in addition to the SST-(Menter) K-omega model, which apply the K-epsilon turbulence model far field and the K-omega model near the wall. The All y+ Wall Treatment is chosen automatically.

In the end we choose the energy model Segregated fluid isothermal, since we have small temperature differences in the flow. The VOF waves model is also chosen for capturing the physics of the waves that will be generated when the hull is moving.

Physics models
All y+ Wall Treatment
Eulerian Multiphase
Gradients
Implicit unsteady
K-Omega Turbulence
Multiphase Equation of State
Multiphase Interaction
Multiphase Mixture
Reynolds-Averaged Navier-Stokes
Segregated Flow
Segregated Fluid Isothermal
Three Dimensional
SST (Menter) K-Omega
Turbulent
VOF Waves
Volume of Fluid (VOF)

Table 5.6: The physics models used for our problem.

In the proceedings some of the physics models are explained. Additional physics set-up is given to some of the models.

ALL y^+ wall treatment

All y^+ wall treatment is automatically selected when we select the k-Omega turbulence model. The wall treatment in STAR-CCM+ is the set of near-wall modelling assumptions for each turbulence model. This term avoids confusion with the term wall functions, which typically refers to only one type of wall treatment. Three types of wall treatment are provided, depending on the turbulence model:

- The high- y^+ wall treatment implies the wall-function-type approach in which it is assumed that the near-wall cell lies within the logarithmic region of the boundary layer.
- The low- y^+ wall treatment is suitable only for low-Reynolds number turbulence models in which it is assumed that the viscous sublayer is properly resolved.
- The all- y^+ wall treatment is a hybrid treatment that attempts to emulate the high- y wall treatment for coarse meshes and the low- y wall treatment for fine meshes. It is also formulated with the desirable characteristic of producing reasonable answers for meshes of intermediate resolution (that is, when the wall-cell centroid falls within the buffer region of the boundary layer).

Both the high- y^+ and all- y^+ wall treatments share a common need to specify profiles of the mean flow quantities in the near-wall region of turbulent boundary layers, and these profiles are termed wall laws.

A wall law is a mathematical description of mean flow quantities, such as velocity, temperature and species concentration, in turbulent boundary layers. Two types of wall laws are used in STAR-CCM+:

- Standard wall laws, which are slope-discontinuous between the laminar and turbulent profiles;
- Blended wall laws, which include a buffer region that smoothly blends the laminar and turbulent profiles together.

The wall laws are not user-selectable, but have been chosen based on the behavior of the turbulence model.

Eulerian multiphase

The eulerian multiphase model is a placeholder for the phases of multiphase flow modelling. An eulerian phase in STAR-CCM+ is a phase modelled in an eulerian

framework. The definition of each eulerian phase includes the set of models applicable to its material; two different materials will constitute two different Eulerian phases. One for water and one for air.

The following list outlines the procedure for creating and defining eulerian phases:

- Creating a new eulerian phase
- Selecting phase models
- Replacing the phase material
- Customizing material properties

For the water phase called phase 1 we choose phase models liquid, constant density, and turbulent. For the Air phase called phase 2 we choose phase models gas, ideal gas and turbulent. Phase material and properties are set to default.

Gradients

The gradients method select the gradient and limiter methods. The gradient and limiter methods are set to default Hybrid Gauss-LSQ and Venkatakrisnan.

Multiphase equation of state

A eulerian multiphase requires its own equation of state model to define how the density of the material will be computed. The water is defined with constant density and the air is defined as an ideal gas.

Multiphase interaction

After the eulerian multiphases have been specified the next step is to define the phase interactions. The interactions are set to default.

Multiphase mixture

The multiphase mixture material model is for simulating two or more immiscible phases, where each phase is composed of a pure gas or liquid substance, such as air and water in our problem. Default mixture is used.

Segregated flow

We can choose between segregated or coupled flow models. The segregated flow model uses less memory than the coupled. The coupled flow model is used for compressible flow, natural convection problems and flows with large body force or energy sources. The segregated flow model is for incompressible or mildly compressible flows. The segregated flow model is suitable for computing the physics of our problem and for keeping the computational resources as low as possible and is therefore used. If computational resources are not an issue, we can choose the coupled flow model for incompressible and/or isothermal flows.

Segregated fluid isothermal

The segregated fluid isothermal uses a constant setting for temperature. For this problem where the temperature variations are small and negligible.

SST (Menter) K-Omega

The SST (Menter) k-omega turbulence model is automatically selected when we select the k-omega turbulence model. Menter's turbulence model, see Menter (1994), is similar to the standard k-omega model, but adds an additional non conservative cross-diffusion term containing the dot product $\nabla k \cdot \nabla \omega$ for reducing the problem of sensitivity to free-stream/inlet conditions. Inclusion of this term in the ω transport equation will potentially make the k-omega model give identical results to k-epsilon model. Menter suggested using a blending function (which includes functions of wall distance) that would include the cross-diffusion term far from walls, but not near the wall. This approach effectively blends a k-epsilon model in the far-field with a k-omega model near the wall.

VOF waves

VOF waves are used to simulate surface gravity waves on a light fluid-heavy fluid interface, where air is the light fluid, and need to be used in conjunction with the volume of fluid (VOF) multiphase model in STAR-CCM+. When created, VOF Waves provide field functions that can be used to initialize the VOF calculation and to provide suitable profiles at boundaries. We do not make any initial wave. The waves will be created as the water and air flows past the hull.

Volume of Fluid (VOF)

After the eulerian multiphase model is used to define phases, and the multiphase interaction model is used to define phase interactions, we can choose the approach

for modelling the multiphase flow: The volume of fluid (VOF) homogenous multiphase model, which assumes a common velocity, pressure and temperature field for all phases. The models variables are set to default. The interface between two immiscible fluids is called a free surface. The VOF multiphase model allows us to resolve the position of the free surface.

The VOF model makes use of multiple eulerian phases and it is necessary to set the initial volume fraction of each phase. This is done by applying a field function to the initial condition called volume fraction for each phase. The field function is located under the tool node i STAR-CCM+ Phase 1 is the water phase and phase 2 the air phase. The field functions for water and air is defined as follows:

Waterfraction: Definition = ($\$Position[1] \leq 2.525$)?1:0

Airfraction: Definition = ($\$Position[1] > 2.525$)?1:0

5.8 Solvers

The solvers used for the problem is selected automatically from the physics models that are already chosen. The solvers used for the problem are:

- Implicit unsteady
- Wall distance
- Damping boundary distance
- Segregated flow
- Segregated VOF
- Segregated energy
- K-Omega turbulence
- K-Omega turbulent viscosity

Implicit unsteady solver

The implicit unsteady solver is activated by the implicit unsteady model. In the implicit unsteady approach each physical time-step involves some number of inner iterations to converge the solution for that given instant of time. These inner iterations may be accomplished using the same implicit integration or explicit integration schemes used for steady analysis. The physical time-step size used

in the outer loop is specified by us, whereas the inner iterations are marched by the integration scheme using optimal local steps as determined by the Courant number.

Wall distance solver

Wall distance is a parameter that represents the distance from a cell centroid to the nearest wall face. It is required by all turbulence models. The wall distance computation is controlled by the wall distance solver.

The wall distance solver controls the wall distance solution in all the continua for which wall distance is calculated. It becomes available when turbulence models are activated. The wall distance calculation takes place during the initialization step of the simulation.

Damping boundary distance solver

Damping boundary distance solver is activated by the VOF waves model. The damping boundary distance solver controls the damping boundary distance solution in all the continua for which damping boundary distance is calculated.

Segregated flow solver

The segregated flow model solves the flow equations, one for each component of velocity, and one for pressure, in a segregated or uncoupled manner. The linkage between the momentum and continuity equations is achieved with a predictor-corrector approach. The complete formulation can be described as using a collocated variable arrangement and a Rhie-and-Chow-type pressure-velocity coupling combined with a SIMPLE-type algorithm.

The segregated flow solver controls the solution update for the segregated flow model according to the SIMPLE algorithm. It controls two additional solvers:

- Velocity solver
- Pressure solver

Velocity solver

Controlled by the segregated flow solver, the velocity solver controls the under-relaxation factor and algebraic multigrid parameters for the momentum equations.

More specifically, it solves the discretized momentum equation to obtain the intermediate velocity field.

Pressure solver

Controlled by the segregated flow solver, the pressure solver controls the under-relaxation factor and algebraic multigrid parameters for the pressure correction equation. More specifically, it solves the discrete equation for pressure correction, and updates the pressure field.

Segregated VOF solver

The segregated VOF solver controls the solution update for the phase volume fractions. It solves the discretized volume-fraction conservation equation for each phase present in the flow.

Segregated energy solver

The segregated energy solver controls the solution update for the segregated fluid energy model. It is used to set the under-relaxation factor and algebraic multigrid parameters for the energy equation. Default parameters are used.

K-Omega turbulence solver

The k-omega turbulence solver controls the solution of the k-omega model in all the continua for which the model is activated. For each transported variable, k and ω , the basic steps involved in the solution update are as follows:

1. Update boundary conditions.
2. Compute the reconstruction gradients and cell gradients.
3. Create the linear system using the discretization methods described in the K-Omega model formulation.
4. Compute the residual sum for the purpose of monitoring convergence.
5. Solve the linear system.
6. Update the transported variable field.

K-Omega turbulent viscosity solver

The k-omega turbulent viscosity solver controls the update of the turbulent viscosity.

5.9 Analyzing

In the simulation process we run 9 simulations for respectively 8, 10, 12, 14, 16, 18, 20, 22 and 24 knots by adjusting the inlet velocity of Water.Inlet and Air.Inlet. By using monitor plots, reports, scalar and vector scenes of the solutions, we are able to control that velocities, forces, pressures, etc. have believable values. We can also control whether fluid variables such as velocity and pressure are smoothly distributed over the body and vary rapidly only where expected.

By using residual monitor we are able to follow the convergence of the solutions. The residual r in each cell represents the degree to which the discretized equation is not completely satisfied. In a perfect converged solution, the residual for each cell would be equal to machine round off. To gauge convergence and the progress of the solution, it is useful to monitor a global quantity given by

$$\sqrt{\frac{\sum_{n \text{ cells}} r^2}{n}}$$

Residual monitors keep a record of this global quantity for each of the transport equations solved in the continua within the simulation.

The results will be compared with the results from the Force Technology's still water performance tests, where a scale model has been used and total resistance measured. The set-up for the still water performance test is given in the next section.

5.10 Force Technology still water performance test

Model description and set-up

The vessel is a model of a fast twin screw SWATH wind turbine service vessel with one open shaft propeller and 2 brackets on the shaft line for each hull. To keep the weight of the model down, the hull was made of foam, reinforced by wood stringers, and protected by yellow paint. A wooden deck was mounted also to give additional strength of the model. Rudders were made in aluminium. Shaft

brackets were produced in brass. The set-up for the tests was deviating from the standard set-up they have for still-water tests, due to the special kind of vessel they were testing. Two poles were mounted in each hull, allowing for pitch motion. The lower point of the poles was positioned at the level of the shaft lines. The poles were connected to each other with a stiff frame. A force gauge (measuring forces on X and Y direction) was mounted on the frame. The whole arrangement was then mounted on the carriage in such a way as to allow for heave motion of the vessel. The model was built in scale 1: 7.376523.

Chapter 6

Simulation results

In this section the results from the nine simulations, for respectively 8, 10, 12, 14, 16, 18, 20, 22 and 24 knots, will be presented. The results of the resistance of the twin hull, the four holes and each of the four holes will be presented. The results of resistance on the twin hull will be compared with the results from the still water performance tests by Rieu and Kishev (2012). Wave making resistance will also be discussed. The resistance of the four holes will be compared with the resistance of the hull. We will also analyze how the water level inside the ballast tanks will be affected as the twin hull is moving.

6.1 Resistance on the twin hull

The simulations have been run 100 time steps and respectively 20 inner iterations per time step, which gives a total of 2000 iterations. We can see that the solutions have converged by looking at the residuals for each simulation. The residuals for the 8 knots simulation are given in Figure 6.1

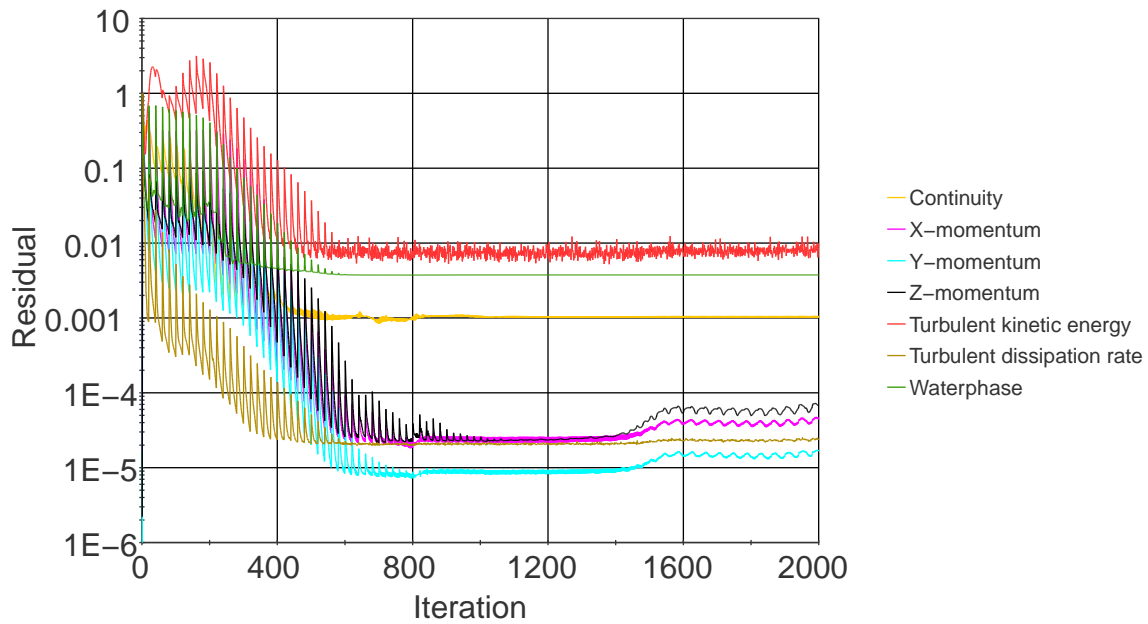


Figure 6.1: Residuals for simulation at 8 knots. The simulation has been run 100 seconds, 20 iterations per time step.

In the start of the simulation the phases are spinned up. This gives transients and may be uninteresting. After 800 iterations almost all the transients have disappeared and there are small changes in the residuals. As the simulation continues to about iteration 1400, the residuals for the momentum equations start to oscillate. The small oscillations may come from boundary effects. By running the simulation further, these small oscillations continue and do not increase. By controlling the velocities, forces and pressures, we can see that they have believable values. We can also see that the velocity and pressure are smoothly distributed over the domain and that there are larger changes at the bow and the stern, see Figure 6.2 for the velocity scene.

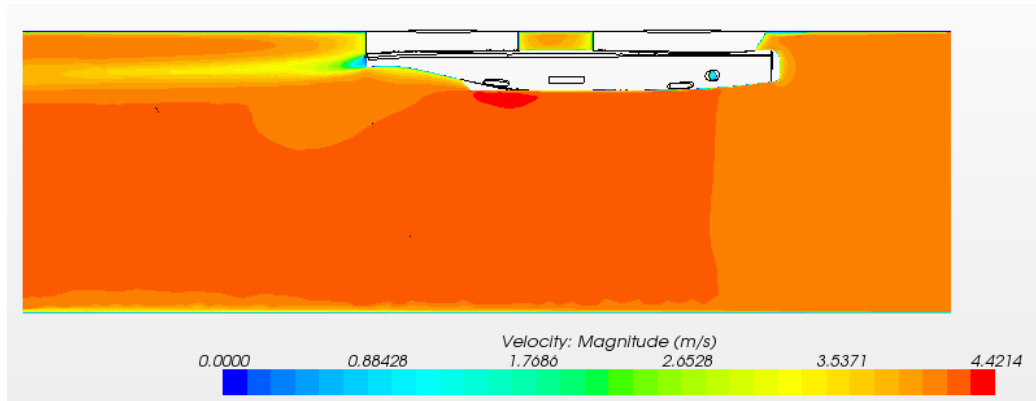


Figure 6.2: Velocity scene at 8 knots. Section in the middle of the hull.

The results of the resistance of the SWATH wind turbine service vessel are given in Figure 6.3 below. Pressure and shear forces are included in the total resistance for our simulation graph (ForceSTARkomega). The simulation is done for one hull, therefore the forces have to be multiplied by 2 to get the forces of the twin hull. We can see that the pressure forces are more dominant than the shear forces.

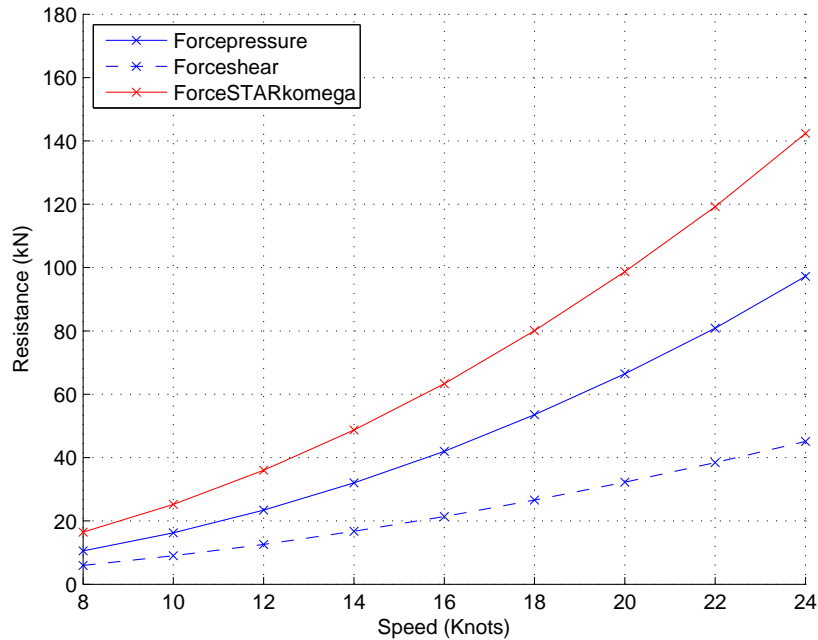


Figure 6.3: Resistance of the twin hull due to pressure and shear forces at 8-24 knots. (ForceSTARkomega) is the total resistance.

The (ForceCOND4) graph, see Figure 6.4, is the total resistance results from a still water performance test, done by Rieu and Kishev (2012) for Force Technology, of the SWATH wind turbine service vessel produced by Danish Yacht A/S, by using a scaled hull model. The results from the scaled model have been transformed to full scale. We are using the same vessel, but in full scale. Below in Figure 6.4 we can see a comparison of the total resistance forces in the simulation (ForceSTARcomega) and the scaled model test (ForceCond4) where the values are taken from the force reports, see Table 6.1.

From Figure 6.4 we can see that the resistance of the simulation (ForceSTARcomega) at 8 and 10 knots is almost similar to the resistance in the scaled model (ForceCond4). The simulation only consider pressure and shear forces. In the scaled model we will have wave making resistance in addition due to generation of waves as the hull displace water. This will explains some of the large resistance differences when the twin hull is moving at 12-24 knots. By considering wave making resistance, we can also see that the resistance for the simulation (ForceSTARcomega) at 8 and 10 knots should be lower as the wave making resistance must be added to the results.

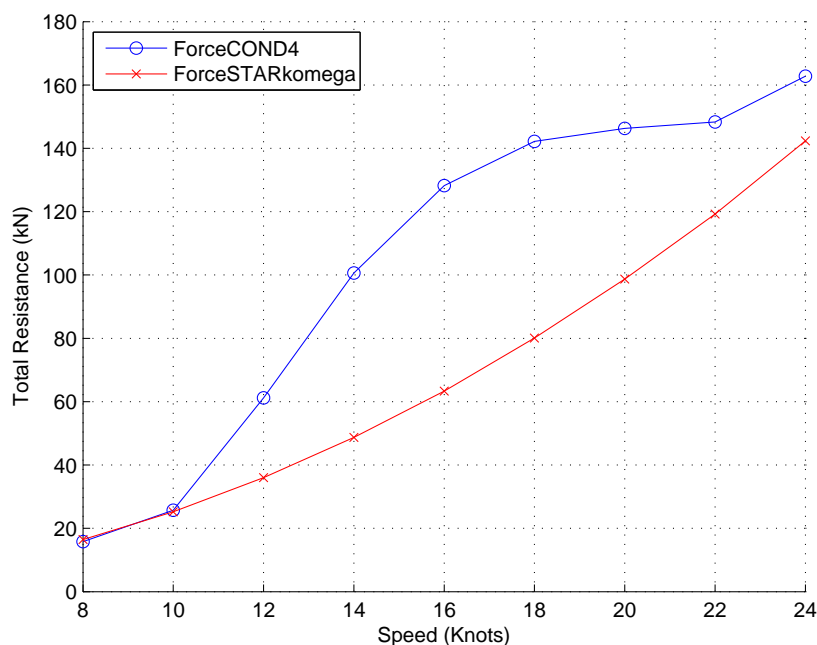


Figure 6.4: Resistance of the twin hull at 8-24 knots

Speed (knots)	ForceCOND4 (kN)	ForceSTARKomega (kN)
8	15.8	16.5
10	25.7	25.2
12	61.2	36.0
14	100.6	48.7
16	128.2	63.4
18	142.2	80.1
20	146.3	98.7
22	148.3	119.3
24	162.8	142.3

Table 6.1: Resistance of the twin hull at 8-24 knots

For a general hull at low speeds the viscous resistance dominates, and at high speeds the total resistance curve turns upward dramatically as wave making resistance begins to dominate, see Figure 6.5. Wave making resistance will be discussed later.

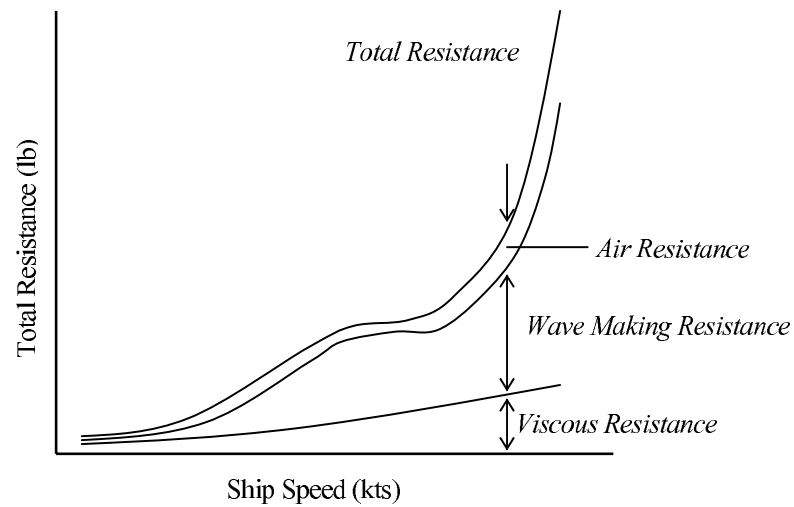


Figure 6.5: A typical curve for the components of the total hull resistance, Surjo and Adji (2007).

An important element is that the hull in the simulation was only able to move in the direction of surge, while the scaled model had two more degrees of freedom, namely pitch and heave motion. The pitch and the heave motion will change the

wetted area of the hull and may lead to increasing resistance due to pressure and shear forces. As the hull moves at higher speeds we may experience that the hull digs down, due to pressure drop under the hull. The wave making resistance may also increase as the twin hull must displace more water. In addition the scaled model has rudders and a main propeller for each hull, that will increase the resistance of hull.

Another element that we have to consider, is that the results from the still water performance test (ForceCond4), will not be equal to a full scale test. According to Dysthe (1992), it is not possible to keep both the Reynolds and the Froude number equal for the two flows. The viscous friction and the wave making resistance can approximately be added together when converting scaled results to full scale.

By considering the simulation set-up, there are several factors that will affect the solution. Some factors are the meshing set-up, boundaries effects, models and the solvers chosen. There are several ways of meshing and the meshing set-up in the simulation may not be the most optimal. Maybe the tetrahedral mesher or the trimmed mesher, should have been used. Due to time limitations other mesh was not tried.

Another consideration is that the simulation domain most likely should have been larger so that the boundaries would make smaller effect on the solution. In the simulation we used one of the hulls. By using both hulls, namely the twin hull, we would have got a better physical solution than by using the symmetry plane. At the same time this would have lead to longer simulation time for each simulation.

Regarding the physics models, we could have chosen another turbulence model, like the Detached Eddy Simulation (DES) which uses both RANS and LES or the Large eddy simulation(LES) which solves the largest scale motions of the flow while approximating or modelling only the small scale motions. The volume of fluid (VOF) model should be considered. The VOF model creates a thick mixing phase, 2 meter, of air and water outside the hull, see Figure 6.6 and even larger after the stern, see Figure 6.7.

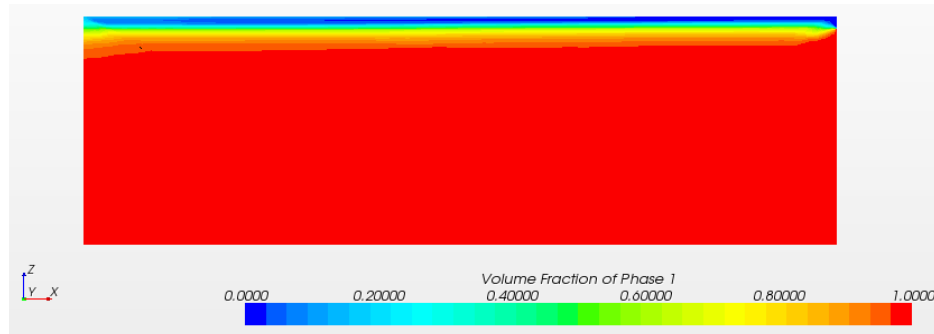


Figure 6.6: Volume fraction of the water phase. The section is outside the hull.

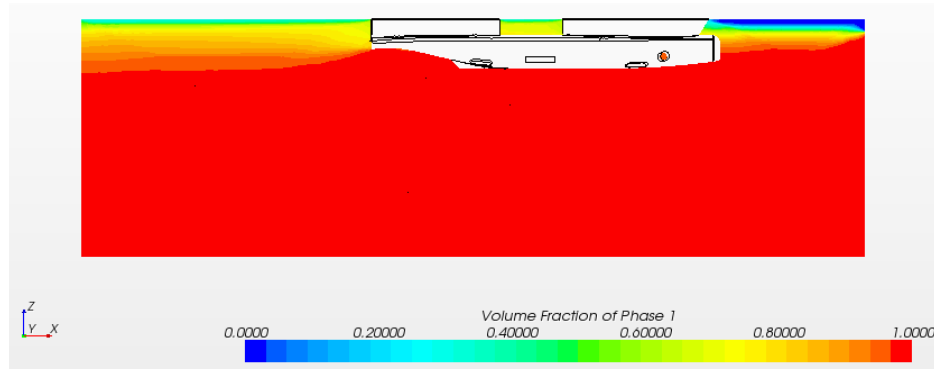


Figure 6.7: Volume fraction of the water phase. The section is in the middle of the hull.

The large mixing phase can be reduced by using the sharpening factor in the Volume of Fluid model (VOF). This was done with the sharpening factors 0.5, 1.0 and 2.0 for the 8 knots simulation with the result of divergence. Most probable the mesh is not suited for the sharpening effect. For obtaining a sharper surface we should consider using a new mesh with the sharpening factor applied to the VOF physics model. After discussions with CD-adapco, we found that the best mesh setup is to use a trimmed volume mesh. The mesh should also be refined by using more cells at the free surface. Due to time limitations, this was not considered.

Wave making resistance

Generally most of the energy given by a ship for making waves, is transferred to water through the bow and stern parts. The two wave systems at the bow and stern waves interact with each other, and the resulting waves are responsible for the resistance. For small displacement hulls, such as sailboats or rowboats, wave-making resistance is the major source of the marine vessel drag.

A simple way of considering wave-making resistance, is to consider the hull in relation to bow and stern waves. If the length of a ship is half the waves generated, the resulting wave will be very small due to cancellation, and if the length is the same as the wavelength, the wave will be large due to enhancement.

By considering a deep water approximation, the phase speed c of the waves is given by equation (2.92):

$$c = \sqrt{\frac{g\lambda}{2\pi}}, \quad (6.1)$$

where λ is the length of the wave and g the gravitational acceleration. Substituting in the appropriate value for g yields the equation:

$$c \approx 1.34 \cdot \sqrt{\lambda}, \quad (6.2)$$

where the values for c and λ are in knots and feet. When the vessel exceeds a "speed-length ratio", see equation (6.3), of 0.94, it starts to outrun most of its bow wave, the hull actually settles slightly in the water as it is now only supported by two wave peaks.

$$\text{Speed-length ratio} \approx \frac{c \text{ in knots}}{\sqrt{\text{length in ft.}}} \quad (6.3)$$

As the vessel exceeds the speed-length ratio of 1.34, the wavelength is now longer than the hull, and the stern is no longer supported by the wake, causing the stern to squat, and the bow rise. The hull is now starting to climb its own bow wave, and resistance begins to increase at a very high rate, see Savitsky (2003).

By comparing the resistance of the scaled model (ForceCOND4) and the simulation (ForceStarkomega), see Figure 6.4, when the hull moves at 12-24 knots, we can see that the wave making resistance is an increasing component of the total resistance. For a speed at 11.89 knots, the speed-length ratio is 1.34 and the wave making resistance begins to increase at a very high rate. This is also confirmed by comparing the scaled model (ForceCOND4) and the simulation (ForceStarkomega) at 12 knots. It is clearly that our simulation does not capture this wave making resistance. This fact explains the large differences between

the scaled model and the simulation for the total resistance from 12-24 knots.

We can do some rough calculations of the wave making resistance by finding the amplitude and the wavelength of the waves generated by the hull. Unfortunately the free surfaces for all the simulations are very diffuse. By looking at the water surface at 90% water phase at 8 knots, see Figures 6.8-6.10, we can see that hull generates waves at the side and at the stern. In addition a wave between the two hulls is generated, to the right of the hull in Figure 6.8. At the same time we can see that we have boundary effects from the inlet, side and the outlet. From the volume fraction of the water phase, see Figure 6.7, we can also see that we will have boundary effects as the mixing phase of air and water reaches the boundary at the top. The simulation domain should be larger in each of these directions.

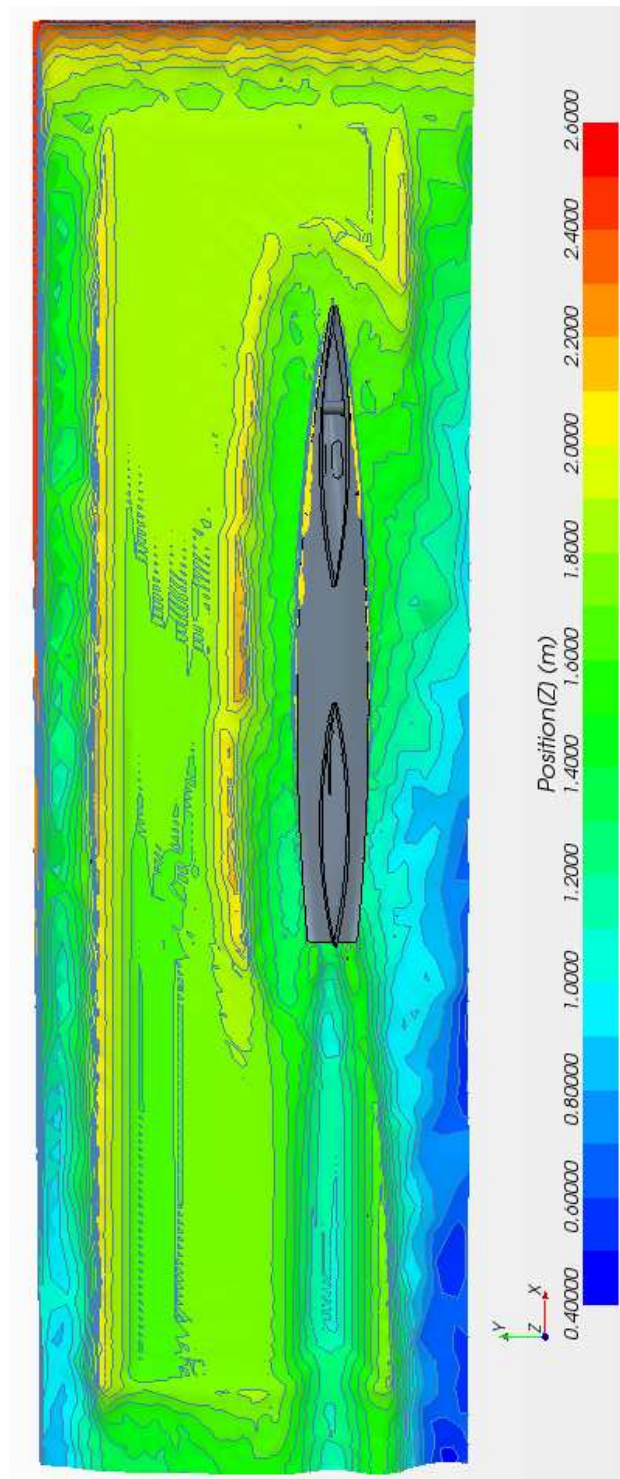


Figure 6.8: Water surface at 90% water phase at 8 knots.

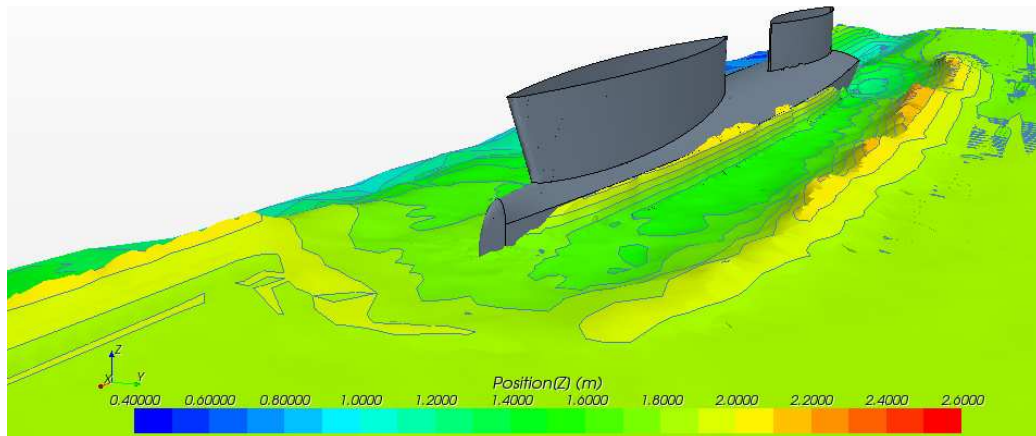


Figure 6.9: Water surface at 90% water phase at 8 knots. Looking at the bow of the hull.

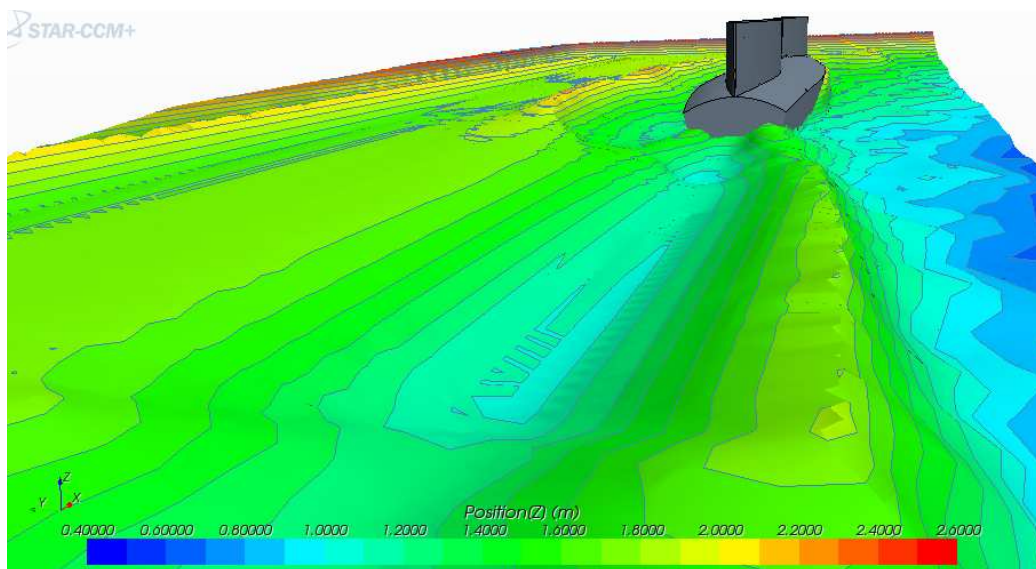


Figure 6.10: Water surface at 90% water phase at 8 knots. Looking at the stern of the hull.

Further we will try to calculate the wave making resistance by using a plane wave instead of the transverse and divergent waves. The wave making resistance can be approximately calculated by finding the amplitude and the wavelength of the wave. By looking at the water surfaces at 90% water phase, see Appendix C, we can find the amplitudes of the waves created between the hulls. The height of the water surface at 90% water phase is $z = 1.7$ meter for all the simulations. The values for the depth of the waves is $z = 0.8 - 1.1$ meter. The amplitude a is the

depth of the waves subtracted from the height of the water surface. The amplitudes are presented in Table 6.2. It is reasonable to think that the amplitude should increase for increasing speeds. This is not the case for the simulations. The reasons for this, may come from boundary effects and the fact that the free surface is very diffuse.

Speed (knots)	Amplitude (Meter)
8	1.1
10	1.0
12	0.9
14	0.9
16	0.9
18	0.8
20	0.8
22	0.8
24	0.8

Table 6.2: Amplitude of the waves generated between the hulls at 8-24 knots

Unfortunately we cannot find the wavelength of the waves from the water surfaces at 90% water phase in Appendix C. Therefore we will consider the case where the speed length ratio is 1.34, and the resistance begins to increase at a very high rate, at approximately 12 knots. The wavelength is equal the ship length in this case. The wave making resistance is assumed to be the difference between the results, see Table 6.1, for the scaled model (ForceCOND4) and the simulation (ForceSTAR ω) and is approximately 25 kN in this case.

We start with the equation (2.99), which is the time average energy flux, per unit length of crest due to a single sinusoidal component of wavenumber k .

$$F = E \cdot C_g = \left[\frac{1}{2} \rho g a^2 \right] \left[\frac{c}{2} \left(1 + \frac{2kH}{\sinh 2kH} \right) \right], \quad (6.4)$$

where $k \equiv \frac{2\pi}{\lambda}$, g is the gravity, c is the phase speed, H is the uniform depth and λ is the wavelength. The phase speed c is given by equation (2.91),

$$c = \sqrt{\frac{g\lambda}{2\pi} \tanh \frac{2\pi H}{\lambda}}. \quad (6.5)$$

Multiplying equation (6.4) with the length of the crest, denoted L , and dividing by the hull speed U we obtain the wave making resistance R_W ,

$$R_W = \frac{F \cdot L}{U}. \quad (6.6)$$

By using the amplitude $a = 0.9$, given in Table 6.2, the wavelength $\lambda = 24$ meter, the uniform depth is $H = 15.5$ meter and assuming that the length of the crest is equal the length between the two hulls at the stern $L = 8$ meter, the approximated wave making resistance R_W at 12 knots can be found. The calculated wave making resistance for a plane wave at 12 knots is found to be 16 kN, which is almost 10 kN smaller than the assumed wave making resistance. For obtaining a larger approximated value for the wave making resistance, the amplitude must be larger.

6.2 Force comparison

In this section the forces on the four holes, consisting of pressure and shear forces, for each speed in the interval 8-24 knots will be presented. The distribution of the forces on the four holes will be compared with the force on the hull. In the comparison of the forces, the force on the hull, the force on the four holes and the force on each of the four holes, are presented in a range of 500 N for the last 500 iterations, iteration 1500-2000, for each monitor plot in Appendix A. The force reports are written for iteration 2000, see Appendix B.1.

First we consider the forces on the four holes, with respect to the resistance on the hull. In Figure 6.11 we can see at the different speeds where the values are taken from the force reports, see Appendix B.1, that the forces on the four holes are 6.7% to 7.2% of the force on the hull. The area of the four holes is 2% of the area of the hull and 2.5% of the wetted surface, where the wetted surface is 164m^2 and the total area 196m^2 , see Table B.10. We can state that the forces on the four holes make a large contribution of the total resistance with respect to the area of the holes and the hull.

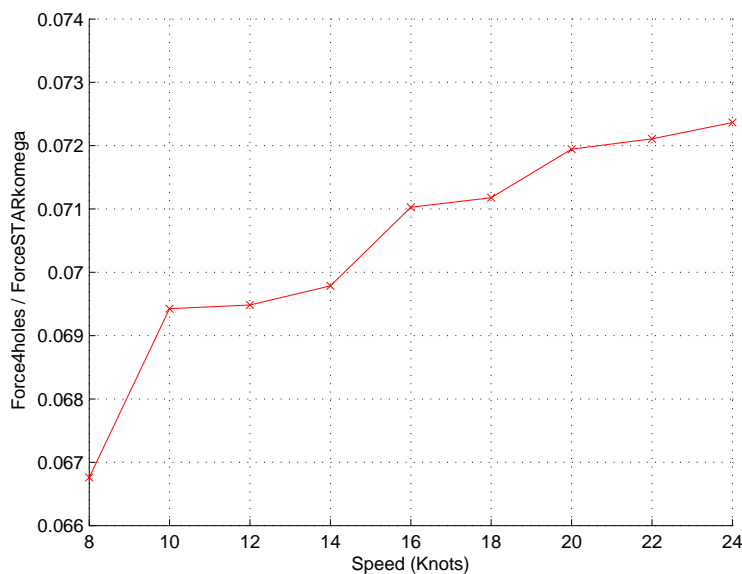


Figure 6.11: The forces on the four holes with respect to the resistance on the hull. The ratio of the forces on the four holes divided by the force on the hull is shown.

Secondly we consider the difference between the forces on each of the four holes taken from the force reports, see Appendix B.1. We get the largest contribution

from the forces on the two holes at the back, see Figure 6.12. Since the area of the holes at the back is almost twice as big as the area of the holes in the front, see Table B.10, this is quite natural.

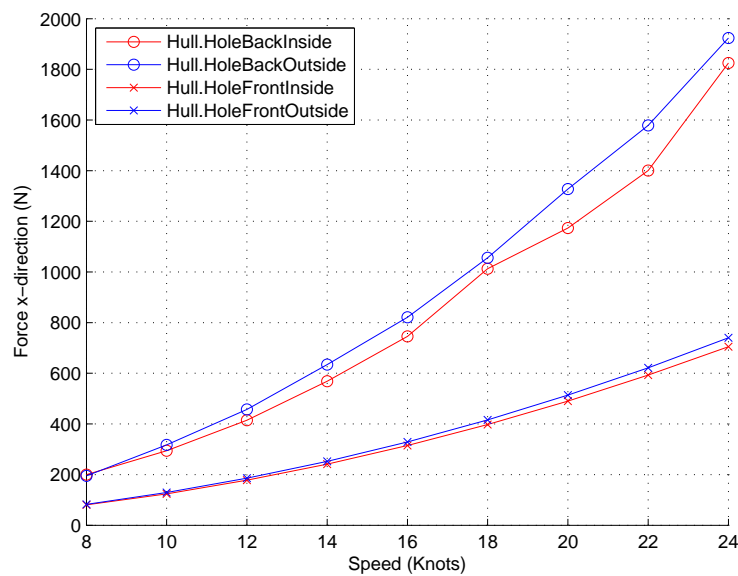


Figure 6.12: Forces on the four holes at iteration 2000.

By considering the force monitor plots, we can examine how the forces vary in time for the last 500 iterations, see Appendix A. The variations of forces on the hull, at low speeds, are mainly caused by the hole Hull.HoleBackInside. As we reach 12 knots, we also get a small contribution from the hole Hull.BackOutside as the force starts to oscillate. The forces on the two holes in the front do not vary in time for the last 500 iterations. In Table 6.3 we can see how much the forces vary in time. The reasons of these variations are most likely because of turbulence and the bad mesh areas effecting the solution, see Figure 5.9. However these effects only make a small effect, 0.3%-0.4%, of the force on the hull.

Speed (Knots)	8	10	12	14	16	18	20	22	24
Part									
Hull.HoleBackInside	<25	25	50	75	100	150	150	200	250
Hull.HoleBackOutside	0	0	<25	<25	25	25	50	75	100
Hull.HoleFrontInside	0	0	0	0	0	0	0	0	0
Hull.HoleFrontOutside	0	0	0	0	0	0	0	0	0
Four holes	<25	25	50	75	100	150	200	250	300
Hull	<25	25	50	75	125	150	200	250	350

Table 6.3: Maximum force differences (N) for the 500 last iterations, 1500-2000, at 8-24 knots. The values are taken from the force monitor plots in Appendix A and are presented in a 25 Newton interval.

6.3 Water level change in the ballast tanks

The ballast tanks in the hull are constructed with open holes to sea. In this section, we will therefore discuss how the water level inside the ballast tanks will be effected due to displacement of water as the hull is moving. In the calculations, the dimensions of the simulation domain is used, see Figure 5.3 and Figure 5.4. We will assume that the sea level does not change for different speeds. The flow is assumed to be inviscid, steady and barotropic. Then we can use the Bernoulli equation (2.41) to calculate the water level change. First we will use the continuity equation to calculate the velocity of the water at the holes in the front at position 2 and the back at position 3, see Figure 6.13. By continuity we have that

$$A_1 u_1 = A_2 u_2 = A_3 u_3, \quad (6.7)$$

where u is the velocity of the water and A is the cross section of the water at the actual position. The initial velocity u_1 is given and the velocity at position 2 and 3 is found by equation (6.7),

$$u_2 = \frac{A_1 u_1}{A_2} \quad \text{and} \quad u_3 = \frac{A_1 u_1}{A_3}. \quad (6.8)$$

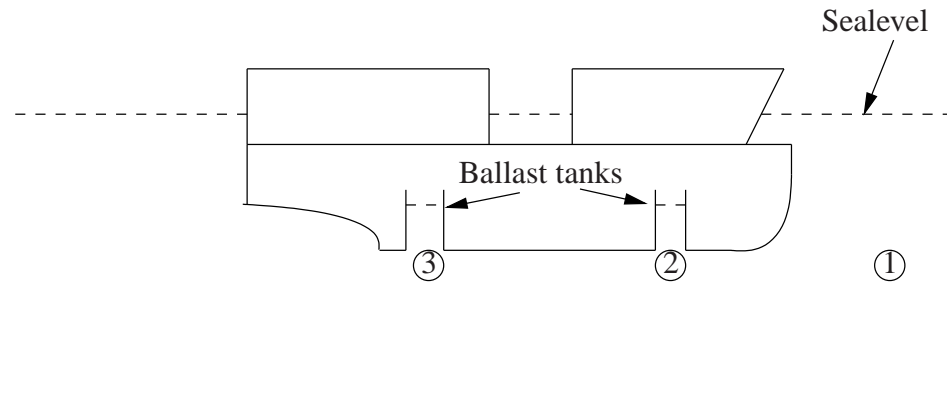


Figure 6.13: The hull with ballast tanks

As the cross section at position 2 and 3 is smaller with respect to the cross section at position 1, we will have an increase in the velocity by the continuity, see equation (6.8). This will lead to a pressure drop at position 2 and 3, which will decrease the water level inside the ballast tanks. The pressure drop is calculated by using Bernoulli's equation (2.41),

$$\frac{1}{2}\mathbf{u} \cdot \mathbf{u} + \frac{p}{\rho} + gz = \text{constant along streamlines.} \quad (6.9)$$

By assuming that the particles at position 2 and 3 lies on the same streamline as particles at position 1, we have that

$$\frac{1}{2}\mathbf{u}_1 \cdot \mathbf{u}_1 + \frac{p_1}{\rho} + gz_1 = \frac{1}{2}\mathbf{u}_2 \cdot \mathbf{u}_2 + \frac{p_2}{\rho} + gz_2. \quad (6.10)$$

Position 1 will be the reference position. The reference pressure and the reference height at position 1 is set to zero, $p_1 = 0$ and $z_1 = 0$. As position 2 and position 1 are at the same height, $z_2 = 0$. Rewriting equation (6.10), the pressure drop can be calculated

$$p_2 = \frac{1}{2}\rho(\mathbf{u}_1 \cdot \mathbf{u}_1 - \mathbf{u}_2 \cdot \mathbf{u}_2). \quad (6.11)$$

The pressure drop will reduce the water level inside the ballast tanks. The water level change, denoted by h , is given by

$$h_2 = \frac{p_2}{\rho g}. \quad (6.12)$$

The water level change at position 3, is calculated in the same way. The cross section at position 2, is larger than the cross section at position 3. Therefore we will have a larger water level change in the ballast tanks at the back at position 3, see Figure 6.14.

The cross section used at the inlet is $A_1 = 233\text{m}^2$. The cross sections at the ballast tanks in the front and the back are respectively $A_2 = 230\text{m}^2$ and $A_3 = 229\text{m}^2$, where the cross section at the inlet has been subtracted the cross sections of the hull that displace water at position 2 and 3. The locations of the cross sections of the hull are shown in Figure 6.15 and the cross section at position 2 is shown in Figure 6.16. The area of the hull at position 2 is calculated with the sea level at 2.5 meter. The same is done at position 3.

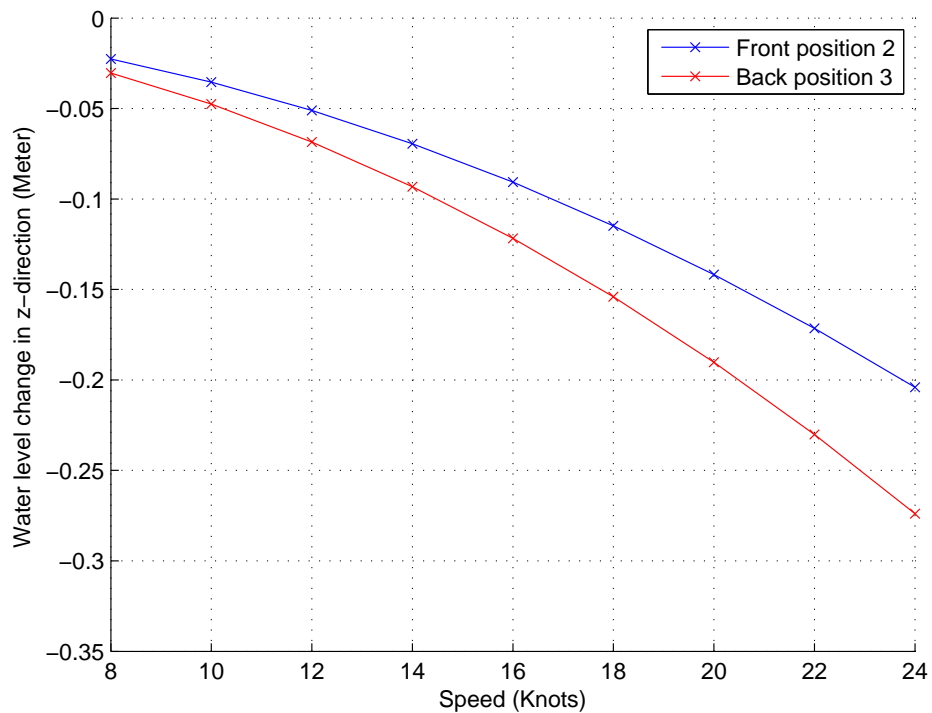


Figure 6.14: Water level change in the ballast tanks.

If we consider the hull to be moving in shallow water, the cross sections A_2 and A_3 are smaller and the velocities at position 2 and 3 will increase. This will result in a larger pressure drop and an additional reduction of the water level in the ballast tanks. At the same time the viscous force of the hull, will increase due to the increased velocity of water.

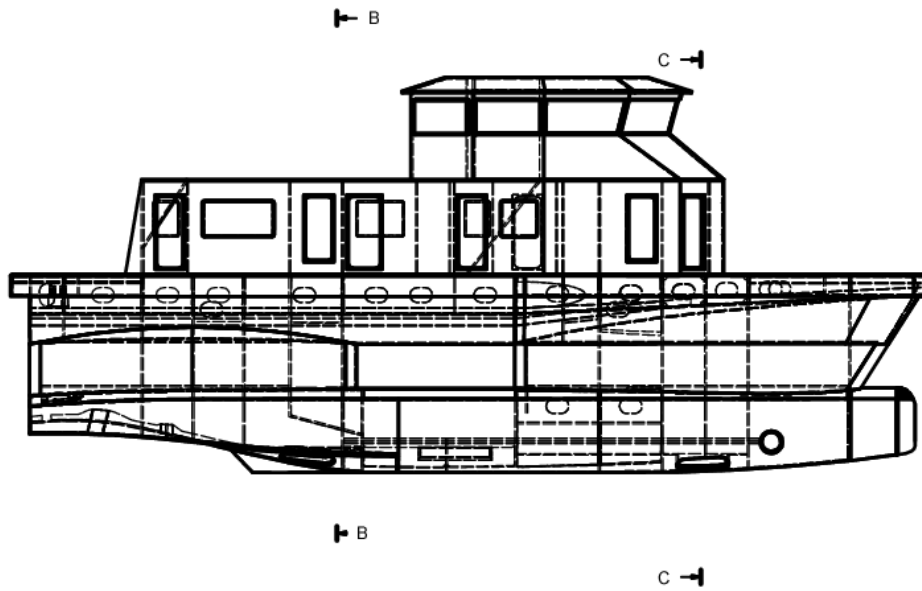


Figure 6.15: Locations of the cross sections of the twin hull.

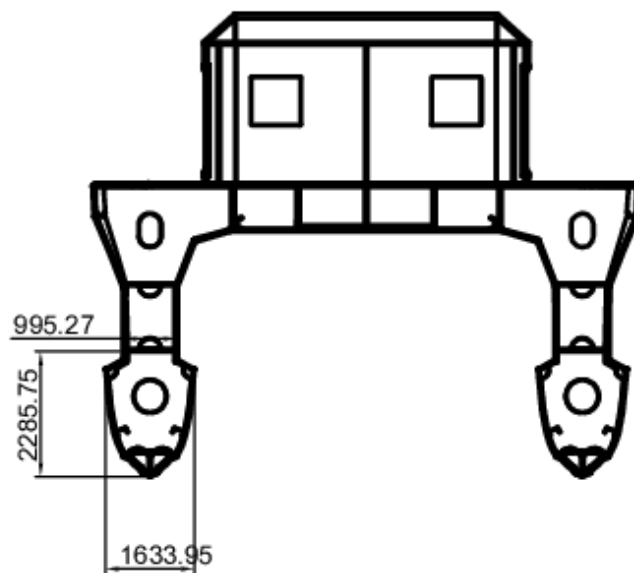


Figure 6.16: Section C-C of Figure 6.15.

Chapter 7

Summary and Discussion

In this thesis I have investigated the hull resistance on a SWATH wind turbine service vessel moving in still water at 8-24 knots by using the CFD tool STAR-CCM+. The model equations needed for the simulation were presented in Chapter 2 and transformed to Reynolds-Averaged Navier-Stokes equations in Chapter 4. From these equations we were able to calculate the flow around the vessel. As I had no prior experience with computational fluid dynamics, much of the theory behind the CFD code was developed in Chapter 3.

In Chapter 5, we developed the simulation set-up. A major part of the work with the simulations set-up was used to obtain a good mesh. After much work with the surface mesh by using the surface remesher, we only produced poor quality mesh that could not be used in the simulation. After several modifications of the surface wrapper, we eventually managed to produce a useful surface mesh. The selection of the boundaries and the physics models STAR-CCM+ userguide, CD-adapco (2011), provided us with the required boundaries and models set-up. As the set-up was well defined, we could start to run the simulations. This process was done many times as we experienced problems with the mesh and boundary effects. After several mesh modifications and changes of the simulation domain size, we were able to achieve better solutions.

“The majority of time spent in industry on a CFD project is usually devoted to successfully generating a mesh for the domain geometry.”

— Tu et al. (2007)

As I received the student license for STAR-CMM+ four months after I started the work with the thesis, time limitations were hindering me in obtaining a good solution without the boundaries effects and the diffuse free surface.

Due to the diffuse free surface and the size of the simulation domain, I did not obtain the wave pattern as the hull moved through the water. Therefore the wave making resistance was not calculated in my simulation. I did however a calculation of the wave making resistance by using a plane wave at 12 knots.

The resistance on the four holes of the hull, where the ballast tanks are placed, compared with the resistance on the hull was found to be approximately 7% of the total resistance.

Further I have examined how the water level inside the ballast tanks of the hull is affected as the vessel moves at different speeds in the simulation domain. For the ballast tanks in the front, the water level reduction was up to 0.20 meter and respectively up to 0.27 meter for the ballast tanks at the back.

Since I did not manage to calculate the wave making resistance in our simulation, we were not able to achieve a fully comparison of our simulation and the scaled test. In the comparison we should also keep in mind the source of error when converting the scaled model results to full scale. In addition the scaled model test allowed pitch and heave motions.

In the further work with the simulation, the simulation domain should be increased and the free surface sharpened. The mesh needs to be refined in the free surface area. After discussions with CD-adapco, the trimmed mesher should be used for the mesh in addition to mesh refinement.

The disadvantage by choosing the commercial program STAR-CCM+ in this thesis, is the fact that the simulation only can be run on one processor at a time. This has limited me in obtaining a good solution without boundary effects and achieving a sharp free surface.

Appendix A

Force monitor plots

Force monitor plot at 8 knots

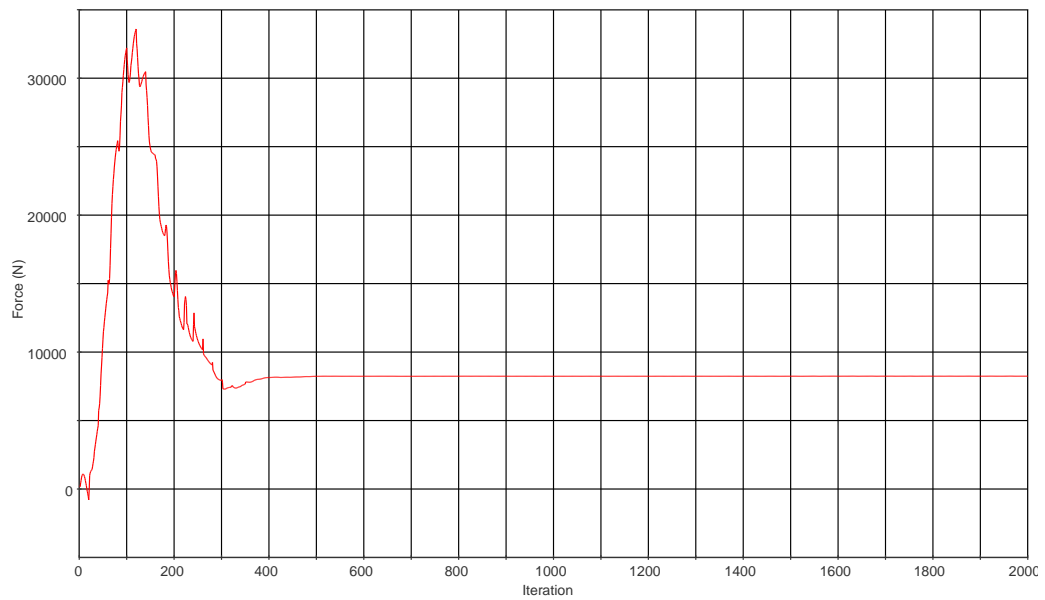


Figure A.1: Total force in the x direction on the hull at 8 knots.

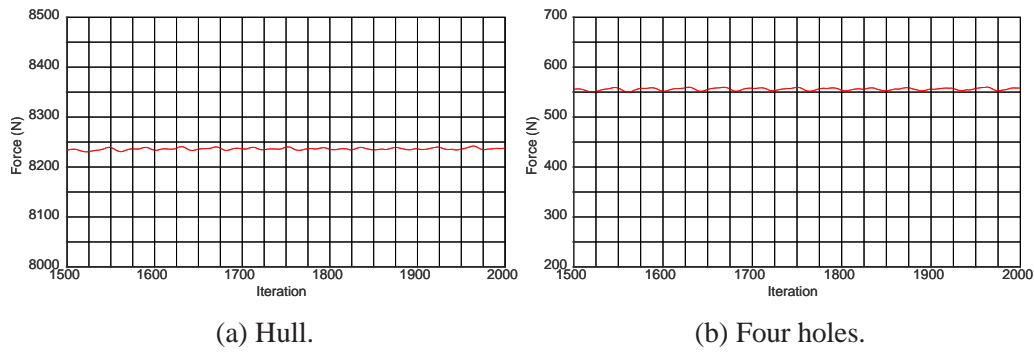


Figure A.2: Total force in the x direction on the hull (A.2a) and the four holes (A.2b) at 8 knots.

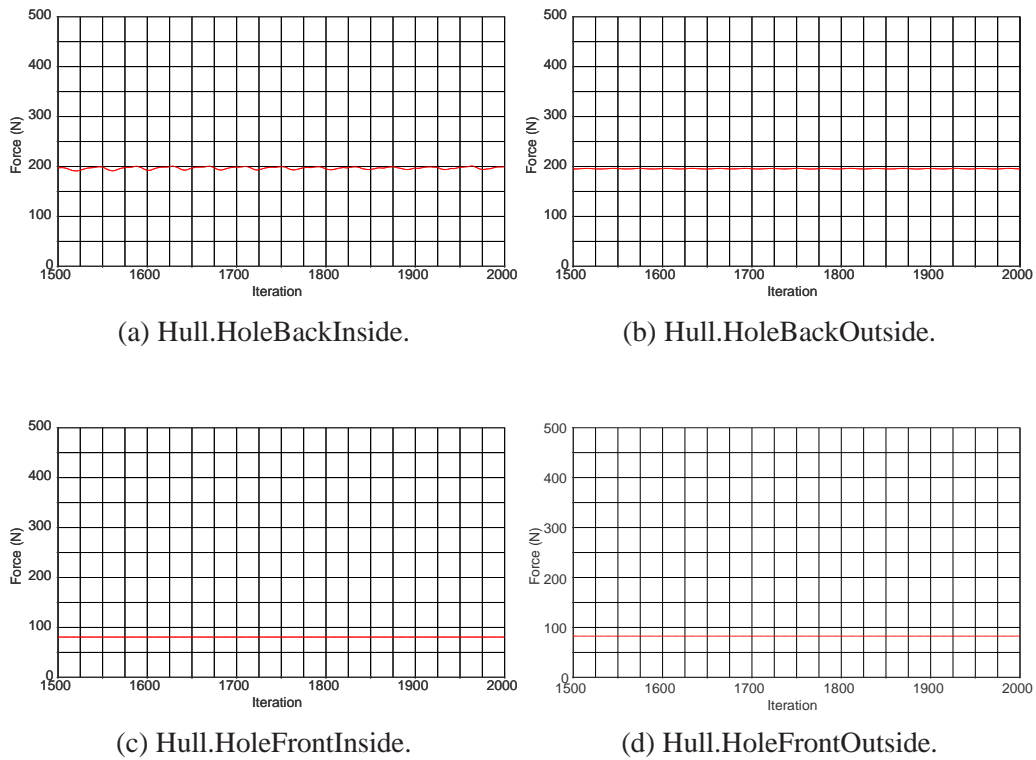


Figure A.3: Force in the x direction on Hull.HoleBackInside (A.3a), Hull.HoleBackOutside (A.3b), Hull.HoleFrontInside (A.3c) and Hull.HoleFrontOutside (A.3d) at 8 knots.

Force monitor plot at 10 knots

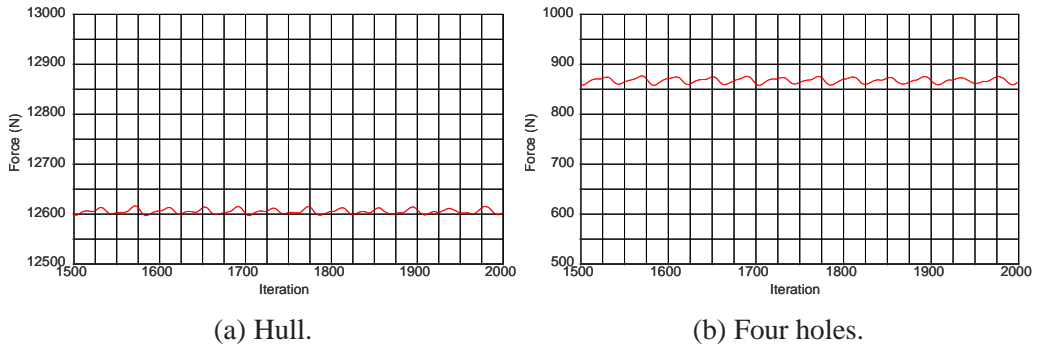


Figure A.4: Total force in the x direction on the hull (A.4a) and the four holes (A.4b) at 10 knots.

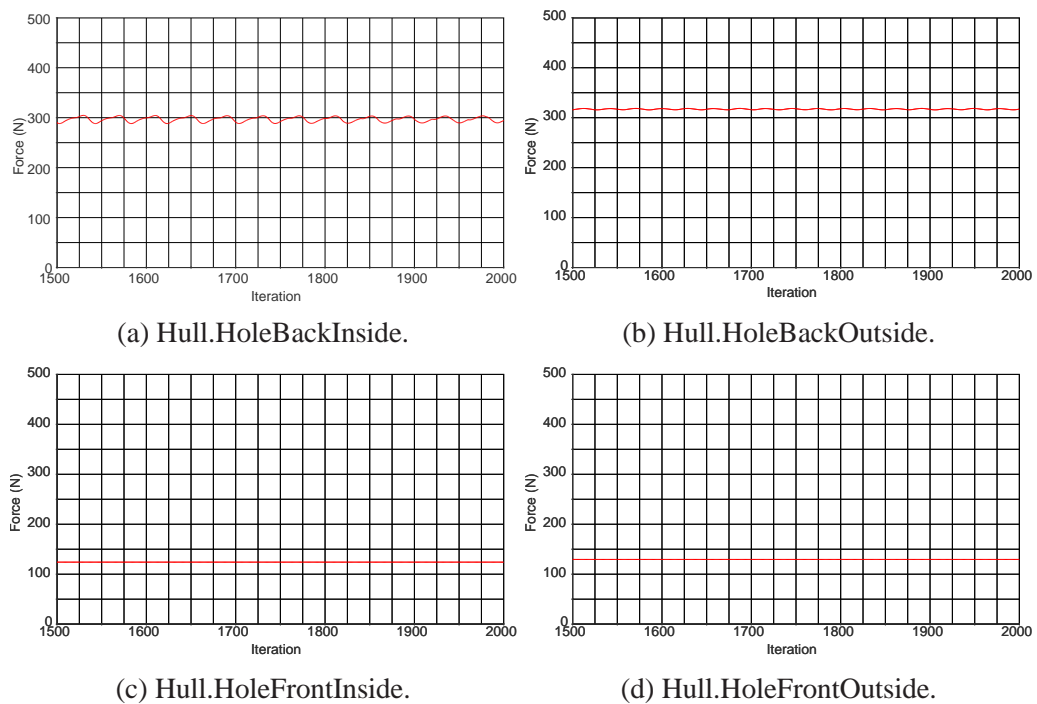


Figure A.5: Force in the x direction on Hull.HoleBackInside (A.5a), Hull.HoleBackOutside (A.5b), Hull.HoleFrontInside (A.5c) and Hull.HoleFrontOutside (A.5d) at 10 knots.

Force monitor plot at 12 knots

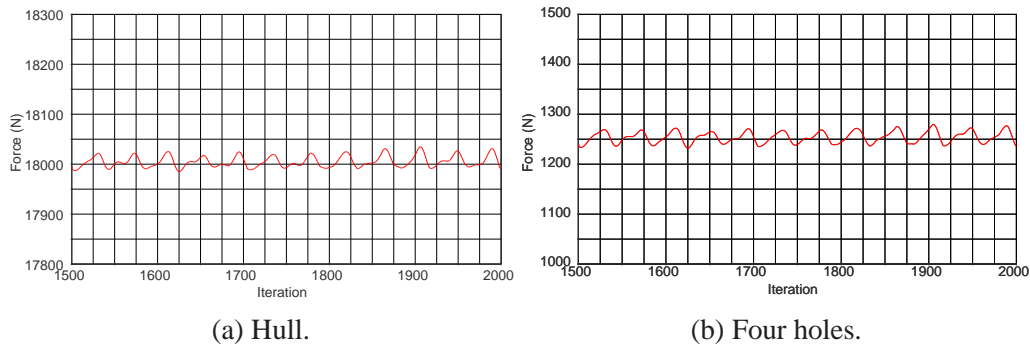


Figure A.6: Total force in the x direction on the hull (A.6a) and the four holes (A.6b) at 12 knots.

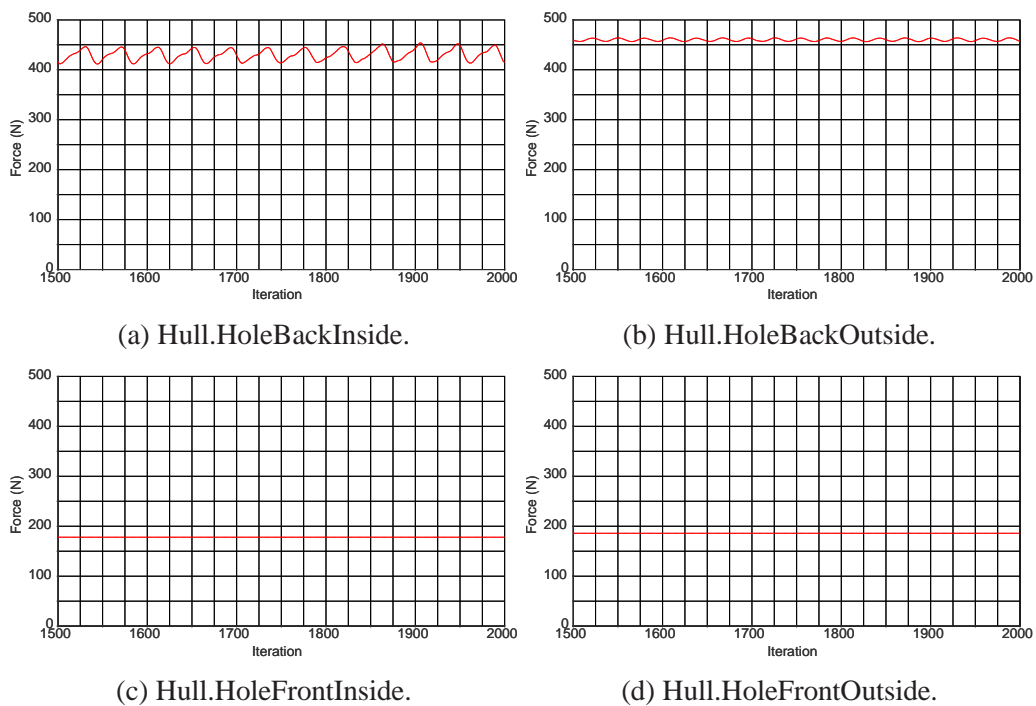


Figure A.7: Force in the x direction on Hull.HoleBackInside (A.7a), Hull.HoleBackOutside (A.7b), Hull.HoleFrontInside (A.7c) and Hull.HoleFrontOutside (A.7d) at 12 knots.

Force monitor plot at 14 knots

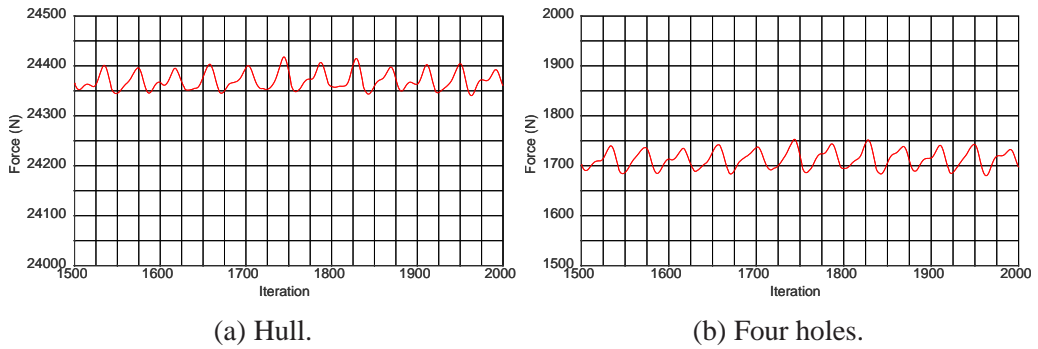


Figure A.8: Total force in the x direction on the hull (A.8a) and the four holes (A.8b) at 14 knots.

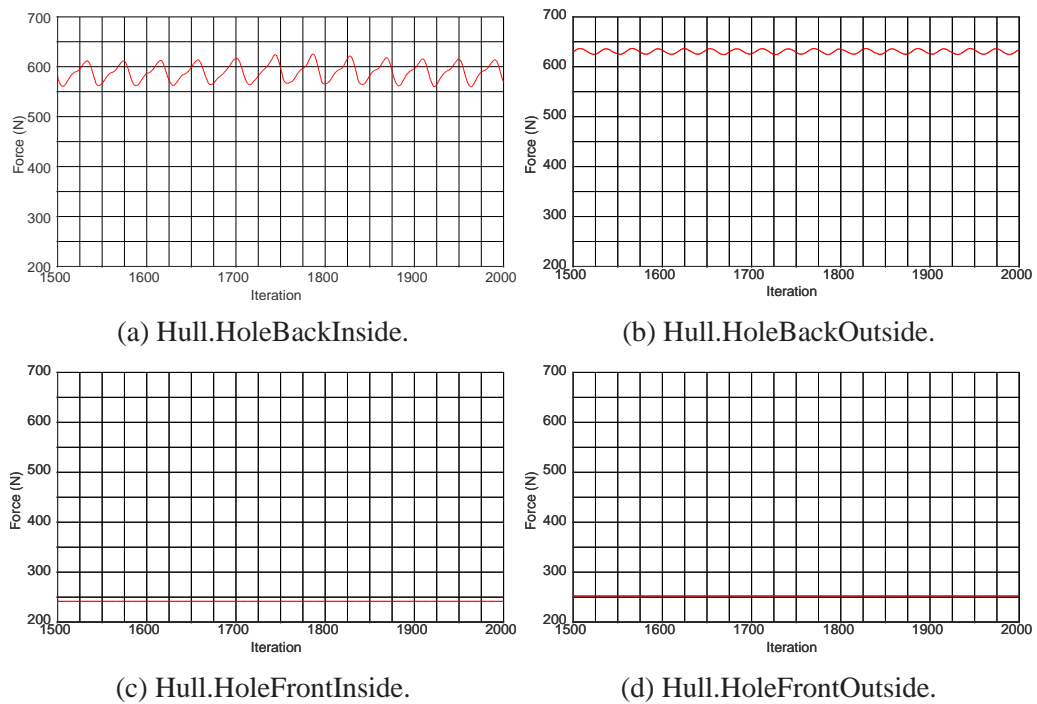


Figure A.9: Force in the x direction on Hull.HoleBackInside (A.9a), Hull.HoleBackOutside (A.9b), Hull.HoleFrontInside (A.9c) and Hull.HoleFrontOutside (A.9d) at 14 knots.

Force monitor plot at 16 knots

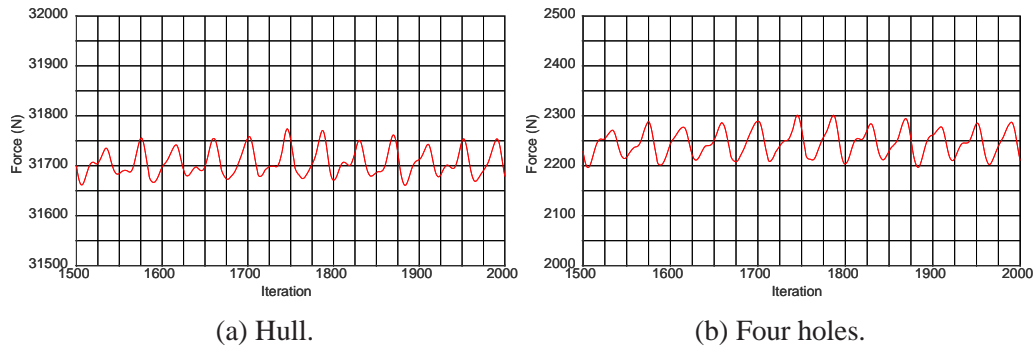


Figure A.10: Total force in the x direction on the hull (A.10a) and the four holes (A.10b) at 16 knots.

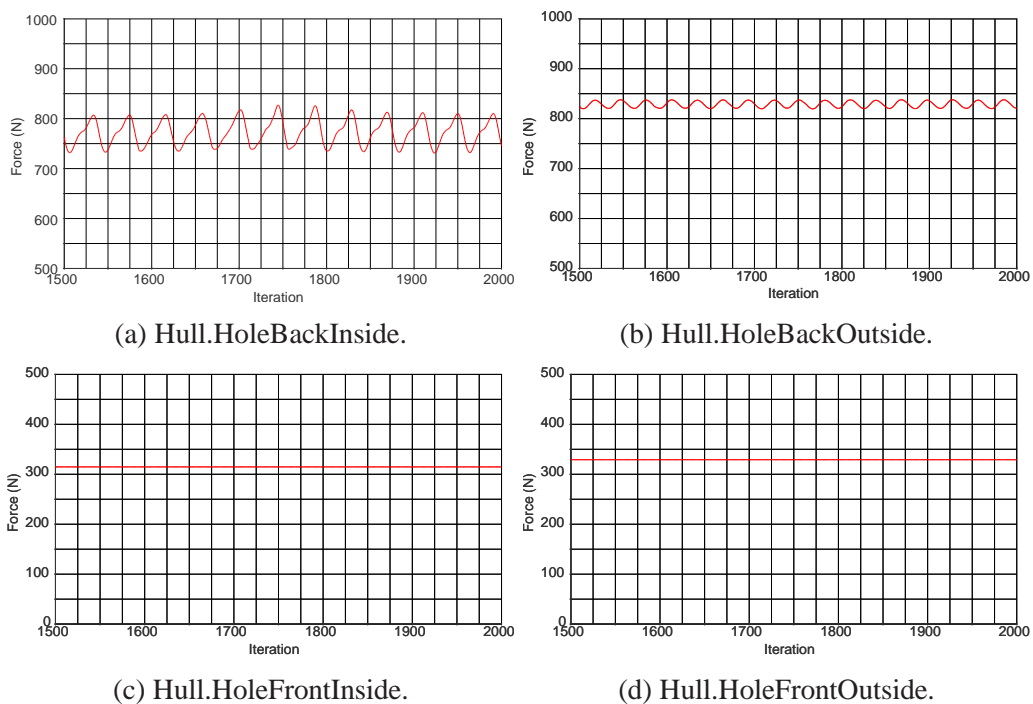


Figure A.11: Force in the x direction on Hull.HoleBackInside (A.11a), Hull.HoleBackOutside (A.11b), Hull.HoleFrontInside (A.11c) and Hull.HoleFrontOutside (A.11d) at 16 knots.

Force monitor plot at 18 knots

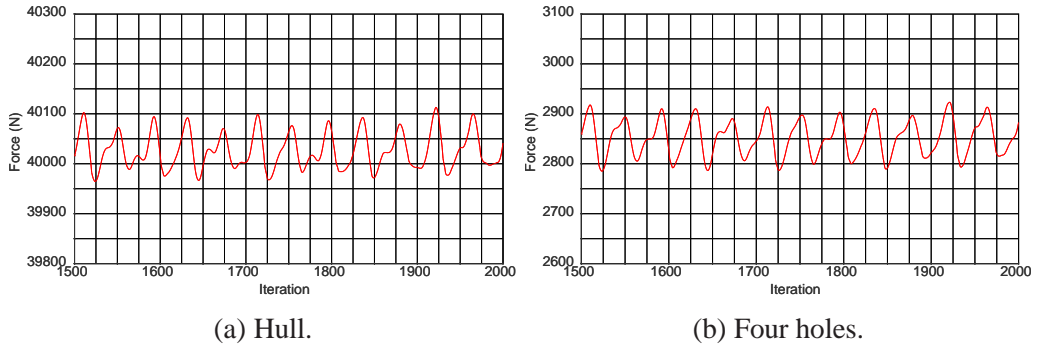


Figure A.12: Total force in the x direction on the hull (A.12a) and the four holes (A.12b) at 18 knots.

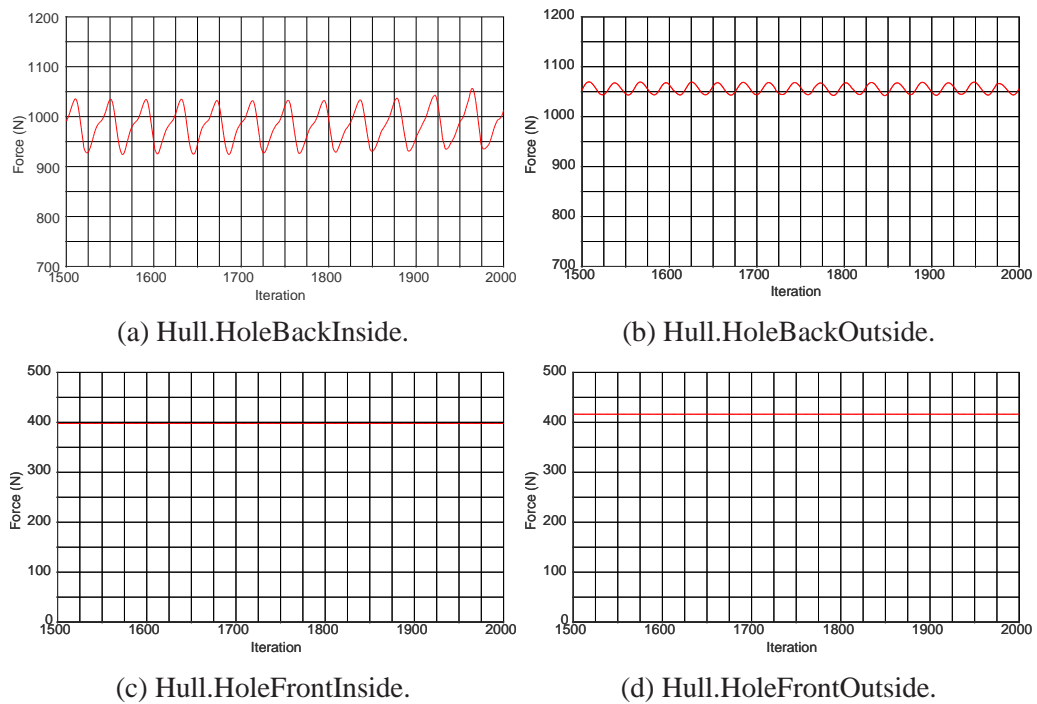


Figure A.13: Force in the x direction on Hull.HoleBackInside (A.13a), Hull.HoleBackOutside (A.13b), Hull.HoleFrontInside (A.13c) and Hull.HoleFrontOutside (A.13d) at 18 knots.

Force monitor plot at 20 knots

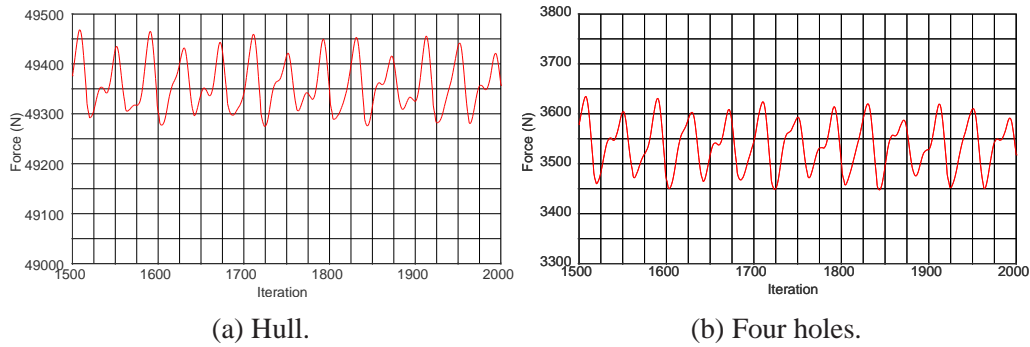


Figure A.14: Total force in the x direction on the hull (A.14a) and the four holes (A.14b) at 20 knots.

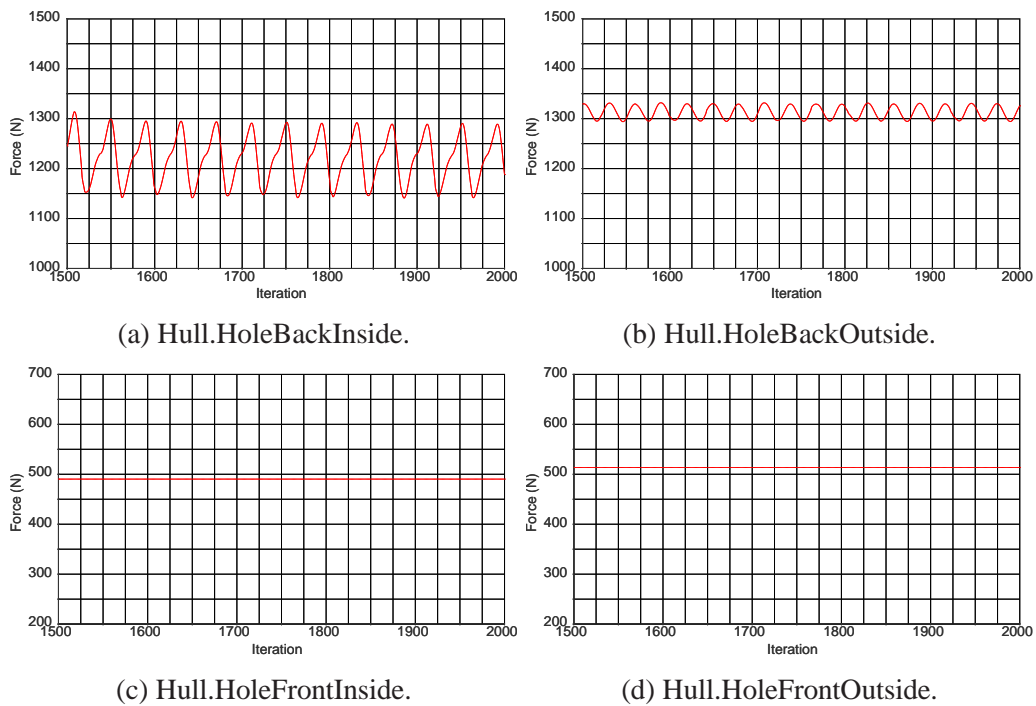


Figure A.15: Force in the x direction on Hull.HoleBackInside (A.15a), Hull.HoleBackOutside (A.15b), Hull.HoleFrontInside (A.15c) and Hull.HoleFrontOutside (A.15d) at 20 knots.

Force monitor plot at 22 knots

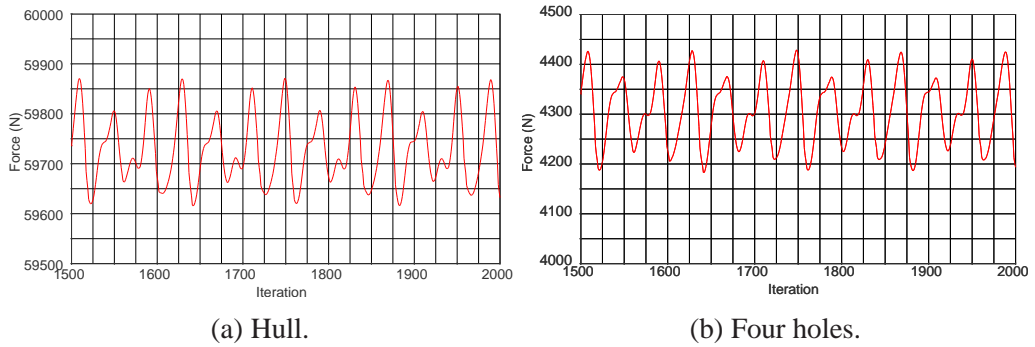


Figure A.16: Total force in the x direction on the hull (A.16a) and the four holes (A.16b) at 22 knots.

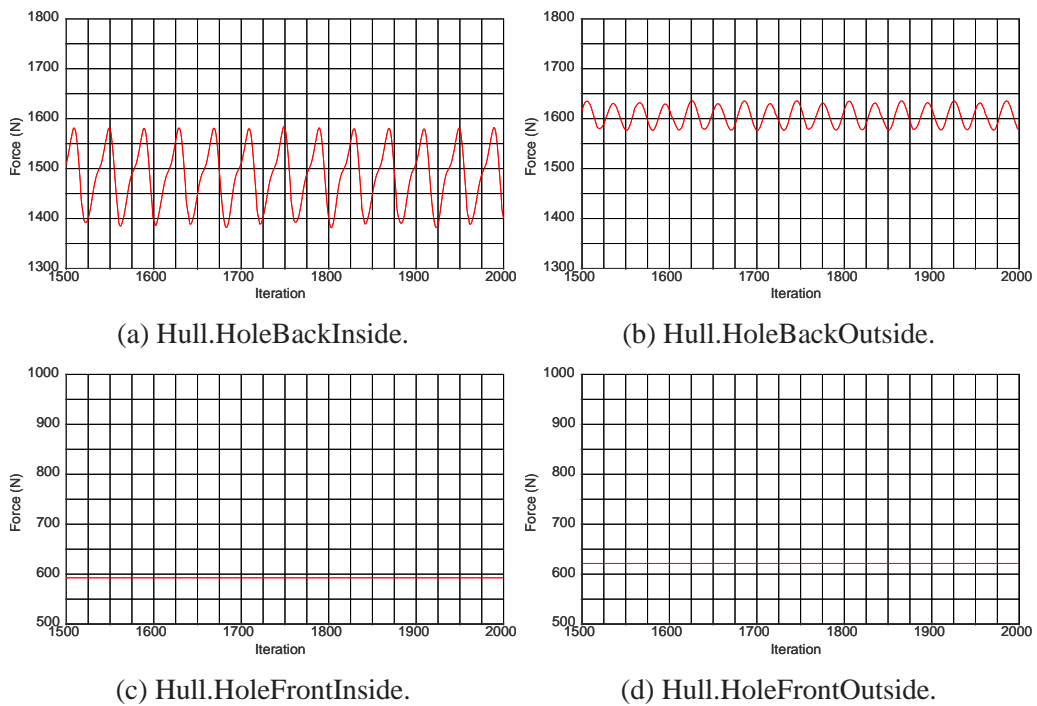


Figure A.17: Force in the x direction on Hull.HoleBackInside (A.17a), Hull.HoleBackOutside (A.17b), Hull.HoleFrontInside (A.17c) and Hull.HoleFrontOutside (A.17d) at 22 knots.

Force monitor plot at 24 knots

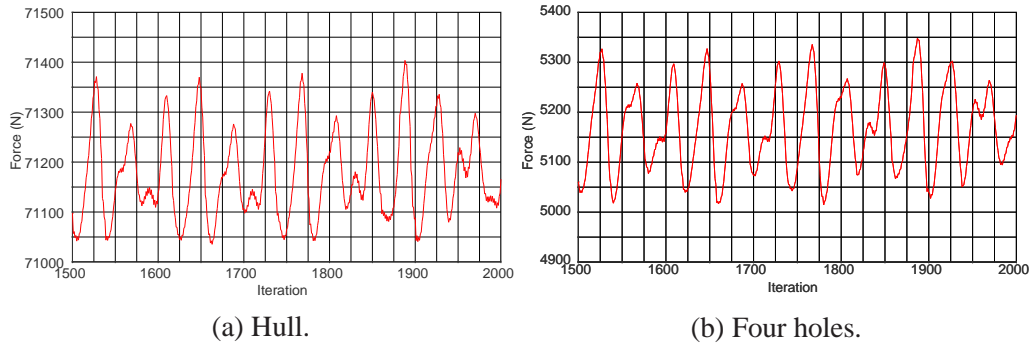


Figure A.18: Total force in the x direction on the hull (A.18a) and the four holes (A.18b) at 24 knots.

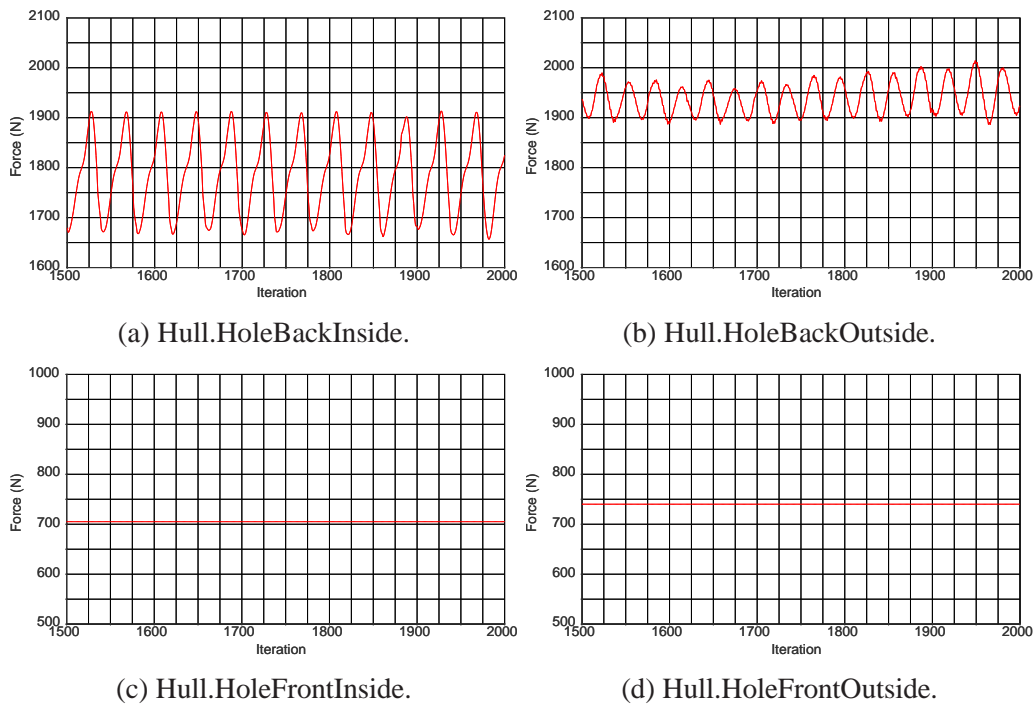


Figure A.19: Force in the x direction on Hull.HoleBackInside (A.19a), Hull.HoleBackOutside (A.19b), Hull.HoleFrontInside (A.19c) and Hull.HoleFrontOutside (A.19d) at 24 knots.

Appendix B

Reports

B.1 Force reports

Force report at 8 knots

Part	Pressure(N)	Shear(N)	Net(N)
Fin			
.Shell	8.276973e+01	3.778908e+01	1.205588e+02
Hull			
.Bau	3.857838e+02	7.516461e+00	3.933002e+02
.HoleBackInside	1.919304e+02	7.792050e+00	1.997225e+02
.HoleBackOutside	1.873389e+02	7.847084e+00	1.951859e+02
.HoleFrontInside	6.939101e+01	1.134841e+01	8.073942e+01
.HoleFrontOutside	7.109531e+01	1.151516e+01	8.261047e+01
.HullSideBottom	2.377830e+03	1.683732e+03	4.061562e+03
.HoleSide	6.758353e+01	1.344935e+01	8.103288e+01
.HullTop	3.061969e+02	5.951210e+02	9.013179e+02
.Tunnel	4.902389e+02	4.978975e+00	4.952179e+02
TopBracketBack			
.TopBracketBack	1.474797e+02	2.996147e+02	4.470944e+02
.TopBracketBackAngle	8.128039e+01	2.247733e+00	8.352812e+01
TopBracketFront			
.TopBracketFront	8.414260e+02	2.833803e+02	1.124806e+03
.TopBracketFrontAngle	-2.925809e+01	8.953545e-01	-2.836273e+01
Total:	5.271086e+03	2.967228e+03	8.238314e+03

Table B.1: Force report of one hull from STAR-CCM+ in direction: [-1, 0, 0] at 8 knots at iteration 2000.

Force report at 10 knots

Part	Pressure(N)	Shear(N)	Net(N)
Fin			
.Shell	1.304129e+02	5.703369e+01	1.874466e+02
Hull			
.Bau	6.009520e+02	1.098790e+01	6.119399e+02
.HoleBackInside	2.833483e+02	1.112972e+01	2.944780e+02
.HoleBackOutside	3.048311e+02	1.227002e+01	3.171011e+02
.HoleFrontInside	1.071807e+02	1.692467e+01	1.241054e+02
.HoleFrontOutside	1.120575e+02	1.745182e+01	1.295093e+02
.HullSideBottom	3.745875e+03	2.562239e+03	6.308115e+03
.HoleSide	9.116286e+01	1.814836e+01	1.093112e+02
.HullTop	4.830156e+02	8.990012e+02	1.382017e+03
.Tunnel	6.164253e+02	7.432342e+00	6.238577e+02
TopBracketBack			
.TopBracketBack	2.267454e+02	4.532109e+02	6.799563e+02
.TopBracketBackAngle	1.287646e+02	3.429504e+00	1.321941e+02
TopBracketFront			
.TopBracketFront	1.321774e+03	4.264752e+02	1.748249e+03
.TopBracketFrontAngle	-4.637096e+01	1.366434e+00	-4.500453e+01
Total:	8.106175e+03	4.497101e+03	1.260328e+04

Table B.2: Force report of one hull from STAR-CCM+ in direction: [-1, 0, 0] at 10 knots at iteration 2000.

Force report at 12 knots

Part	Pressure(N)	Shear(N)	Net(N)
Fin			
.Shell	1.892811e+02	7.987756e+01	2.691587e+02
Hull			
.Bau	8.644252e+02	1.500735e+01	8.794326e+02
.HoleBackInside	3.989086e+02	1.553532e+01	4.144439e+02
.HoleBackOutside	4.402881e+02	1.722615e+01	4.575143e+02
.HoleFrontInside	1.542933e+02	2.368545e+01	1.779787e+02
.HoleFrontOutside	1.614381e+02	2.442247e+01	1.858606e+02
.HullSideBottom	5.409539e+03	3.584166e+03	8.993705e+03
.HoleSide	1.315473e+02	2.539344e+01	1.569408e+02
.HullTop	6.999909e+02	1.259011e+03	1.959002e+03
.Tunnel	8.889339e+02	1.027674e+01	8.992106e+02
TopBracketBack			
.TopBracketBack	3.206772e+02	6.352313e+02	9.559086e+02
.TopBracketBackAngle	1.867913e+02	4.843504e+00	1.916348e+02
TopBracketFront			
.TopBracketFront	1.919206e+03	5.954617e+02	2.514668e+03
.TopBracketFrontAngle	-6.767478e+01	1.931799e+00	-6.574298e+01
Total:	1.169764e+04	6.292070e+03	1.798971e+04

Table B.3: Force report of one hull from STAR-CCM+ in direction: [-1, 0, 0] at 12 knots at iteration 2000.

Force report at 14 knots

Part	Pressure(N)	Shear(N)	Net(N)
Fin			
.Shell	2.596847e+02	1.062288e+02	3.659135e+02
Hull			
.Bau	1.176710e+03	1.954943e+01	1.196260e+03
.HoleBackInside	5.478113e+02	2.067233e+01	5.684836e+02
.HoleBackOutside	6.113240e+02	2.307490e+01	6.343989e+02
.HoleFrontInside	2.100628e+02	3.147455e+01	2.415374e+02
.HoleFrontOutside	2.199460e+02	3.245635e+01	2.524024e+02
.HullSideBottom	7.392635e+03	4.762839e+03	1.215547e+04
.HoleSide	1.794960e+02	3.373374e+01	2.132297e+02
.HullTop	9.603319e+02	1.674125e+03	2.634457e+03
.Tunnel	1.211928e+03	1.351495e+01	1.225443e+03
TopBracketBack			
.TopBracketBack	4.309025e+02	8.443434e+02	1.275246e+03
.TopBracketBackAngle	2.562237e+02	6.485228e+00	2.627089e+02
TopBracketFront			
.TopBracketFront	2.636295e+03	7.890101e+02	3.425305e+03
.TopBracketFrontAngle	-9.353768e+01	2.592479e+00	-9.094520e+01
Total:	1.599981e+04	8.360101e+03	2.435991e+04

Table B.4: Force report of one hull from STAR-CCM+ in direction: [-1, 0, 0] at 14 knots at iteration 2000.

Force report at 16 knots

Part	Pressure(N)	Shear(N)	Net(N)
Fin			
.Shell	3.415864e+02	1.360386e+02	4.776250e+02
Hull			
.Bau	1.538274e+03	2.459626e+01	1.562871e+03
.HoleBackInside	7.190635e+02	2.646872e+01	7.455322e+02
.HoleBackOutside	7.911243e+02	2.972759e+01	8.208519e+02
.HoleFrontInside	2.744825e+02	4.027265e+01	3.147552e+02
.HoleFrontOutside	2.876211e+02	4.153103e+01	3.291522e+02
.HullSideBottom	9.698019e+03	6.094347e+03	1.579237e+04
.HoleSide	2.351887e+02	4.313973e+01	2.783284e+02
.HullTop	1.265370e+03	2.142773e+03	3.408143e+03
.Tunnel	1.586156e+03	1.712562e+01	1.603282e+03
TopBracketBack			
.TopBracketBack	5.560085e+02	1.079486e+03	1.635494e+03
.TopBracketBackAngle	3.378169e+02	8.351807e+00	3.461688e+02
TopBracketFront			
.TopBracketFront	3.478667e+03	1.005961e+03	4.484627e+03
.TopBracketFrontAngle	-1.243606e+02	3.343508e+00	-1.210171e+02
Total:	2.098501e+04	1.069316e+04	3.167818e+04

Table B.5: Force report of one hull from STAR-CCM+ in direction: [-1, 0, 0] at 16 knots at iteration 2000.

Force report at 18 knots

Part	Pressure(N)	Shear(N)	Net(N)
Fin			
.Shell	4.354662e+02	1.691640e+02	6.046301e+02
Hull			
.Bau	1.950024e+03	3.013161e+01	1.980156e+03
.HoleBackInside	9.779163e+02	3.503773e+01	1.012954e+03
.HoleBackOutside	1.018867e+03	3.723394e+01	1.056101e+03
.HoleFrontInside	3.475884e+02	5.006047e+01	3.976488e+02
.HoleFrontOutside	3.645412e+02	5.162445e+01	4.161657e+02
.HullSideBottom	1.231151e+04	7.577137e+03	1.988864e+04
.HoleSide	2.987491e+02	5.357869e+01	3.523278e+02
.HullTop	1.617005e+03	2.663393e+03	4.280398e+03
.Tunnel	2.012657e+03	2.108287e+01	2.033739e+03
TopBracketBack			
.TopBracketBack	6.942125e+02	1.339442e+03	2.033655e+03
.TopBracketBackAngle	4.322026e+02	1.044031e+01	4.426429e+02
TopBracketFront			
.TopBracketFront	4.453941e+03	1.244957e+03	5.698897e+03
.TopBracketFrontAngle	-1.606967e+02	4.200983e+00	-1.564957e+02
Total:	2.675398e+04	1.328749e+04	4.004147e+04

Table B.6: Force report of one hull from STAR-CCM+ in direction: [-1, 0, 0] at 18 knots at iteration 2000.

Force report at 20 knots

Part	Pressure(N)	Shear(N)	Net(N)
Fin			
.Shell	5.424094e+02	2.057608e+02	7.481702e+02
Hull			
.Bau	2.412701e+03	3.614110e+01	2.448842e+03
.HoleBackInside	1.133719e+03	3.989454e+01	1.173613e+03
.HoleBackOutside	1.282628e+03	4.493037e+01	1.327558e+03
.HoleFrontInside	4.294810e+02	6.081012e+01	4.902911e+02
.HoleFrontOutside	4.508358e+02	6.271303e+01	5.135488e+02
.HullSideBottom	1.532826e+04	9.202528e+03	2.453079e+04
.HoleSide	3.707466e+02	6.502305e+01	4.357696e+02
.HullTop	2.018611e+03	3.235008e+03	5.253619e+03
.Tunnel	2.492978e+03	2.535453e+01	2.518333e+03
TopBracketBack			
.TopBracketBack	8.471848e+02	1.623156e+03	2.470341e+03
.TopBracketBackAngle	5.405635e+02	1.275104e+01	5.533146e+02
TopBracketFront			
.TopBracketFront	5.571782e+03	1.505663e+03	7.077445e+03
.TopBracketFrontAngle	-2.031747e+02	5.149165e+00	-1.980256e+02
Total:	3.321872e+04	1.612488e+04	4.934361e+04

Table B.7: Force report of one hull from STAR-CCM+ in direction: [-1, 0, 0] at 20 knots at iteration 2000.

Force report at 22 knots

Part	Pressure(N)	Shear(N)	Net(N)
Fin			
.Shell	6.615268e+02	2.456586e+02	9.071854e+02
Hull			
.Bau	2.927407e+03	4.261288e+01	2.970020e+03
.HoleBackInside	1.352559e+03	4.763290e+01	1.400192e+03
.HoleBackOutside	1.525048e+03	5.384350e+01	1.578892e+03
.HoleFrontInside	5.202383e+02	7.250365e+01	5.927420e+02
.HoleFrontOutside	5.466527e+02	7.477359e+01	6.214263e+02
.HullSideBottom	1.866921e+04	1.097311e+04	2.964232e+04
.HoleSide	4.517101e+02	7.745227e+01	5.291623e+02
.HullTop	2.472537e+03	3.855680e+03	6.328217e+03
.Tunnel	3.030116e+03	2.990698e+01	3.060023e+03
TopBracketBack			
.TopBracketBack	1.009509e+03	1.929447e+03	2.938956e+03
.TopBracketBackAngle	6.639431e+02	1.528430e+01	6.792274e+02
TopBracketFront			
.TopBracketFront	6.843086e+03	1.786761e+03	8.629846e+03
.TopBracketFrontAngle	-2.523509e+02	6.096397e+00	-2.462545e+02
Total:	4.042119e+04	1.921076e+04	5.963196e+04

Table B.8: Force report of one hull from STAR-CCM+ in direction: [-1, 0, 0] at 22 knots at iteration 2000.

Force report at 24 knots

Part	Pressure(N)	Shear(N)	Net(N)
Fin			
.Shell	7.944466e+02	2.886543e+02	1.083101e+03
Hull			
.Bau	3.495122e+03	4.953687e+01	3.544659e+03
.HoleBackInside	1.764715e+03	6.041081e+01	1.825126e+03
.HoleBackOutside	1.860345e+03	6.354739e+01	1.923893e+03
.HoleFrontInside	6.200448e+02	8.511361e+01	7.051584e+02
.HoleFrontOutside	6.522783e+02	8.777713e+01	7.400555e+02
.HullSideBottom	2.233220e+04	1.288769e+04	3.521990e+04
.HoleSide	5.428103e+02	9.083305e+01	6.336433e+02
.HullTop	2.982074e+03	4.524256e+03	7.506330e+03
.Tunnel	3.626318e+03	3.469823e+01	3.661017e+03
TopBracketBack			
.TopBracketBack	1.177132e+03	2.256975e+03	3.434108e+03
.TopBracketBackAngle	8.036749e+02	1.803945e+01	8.217143e+02
TopBracketFront			
.TopBracketFront	8.281960e+03	2.087190e+03	1.036915e+04
.TopBracketFrontAngle	-3.093325e+02	7.185497e+00	-3.021470e+02
Total:	4.862379e+04	2.254191e+04	7.116570e+04

Table B.9: Force report of one hull from STAR-CCM+ in direction: [-1, 0, 0] at 24 knots at iteration 2000.

B.2 Area of hull report

Part	Area (m ²)
Fin.Shell	1.913001e+00
Hull.Bau	1.602044e+00
Hull.HoleBackInside	1.347671e+00
Hull.HoleBackOutside	1.348610e+00
Hull.HoleFrontInside	7.066795e-01
Hull.HoleFrontOutside	7.050649e-01
Hull.HullSideBottom	1.033655e+02
Hull.HoleSide	9.530661e-01
Hull.HullTop	3.786161e+01
Hull.Tunnel	1.568206e+00
TopBracketBack.TopBracketBack	2.080200e+01
TopBracketBack.TopBracketBackAngle	1.304931e-01
TopBracketFront.TopBracketFront	2.330916e+01
TopBracketFront.TopBracketFrontAngle	3.731476e-02
Total:	1.956504e+02
Wetted surface	1.641335e+02

Table B.10: Area of the hull.

Appendix C

Water surface

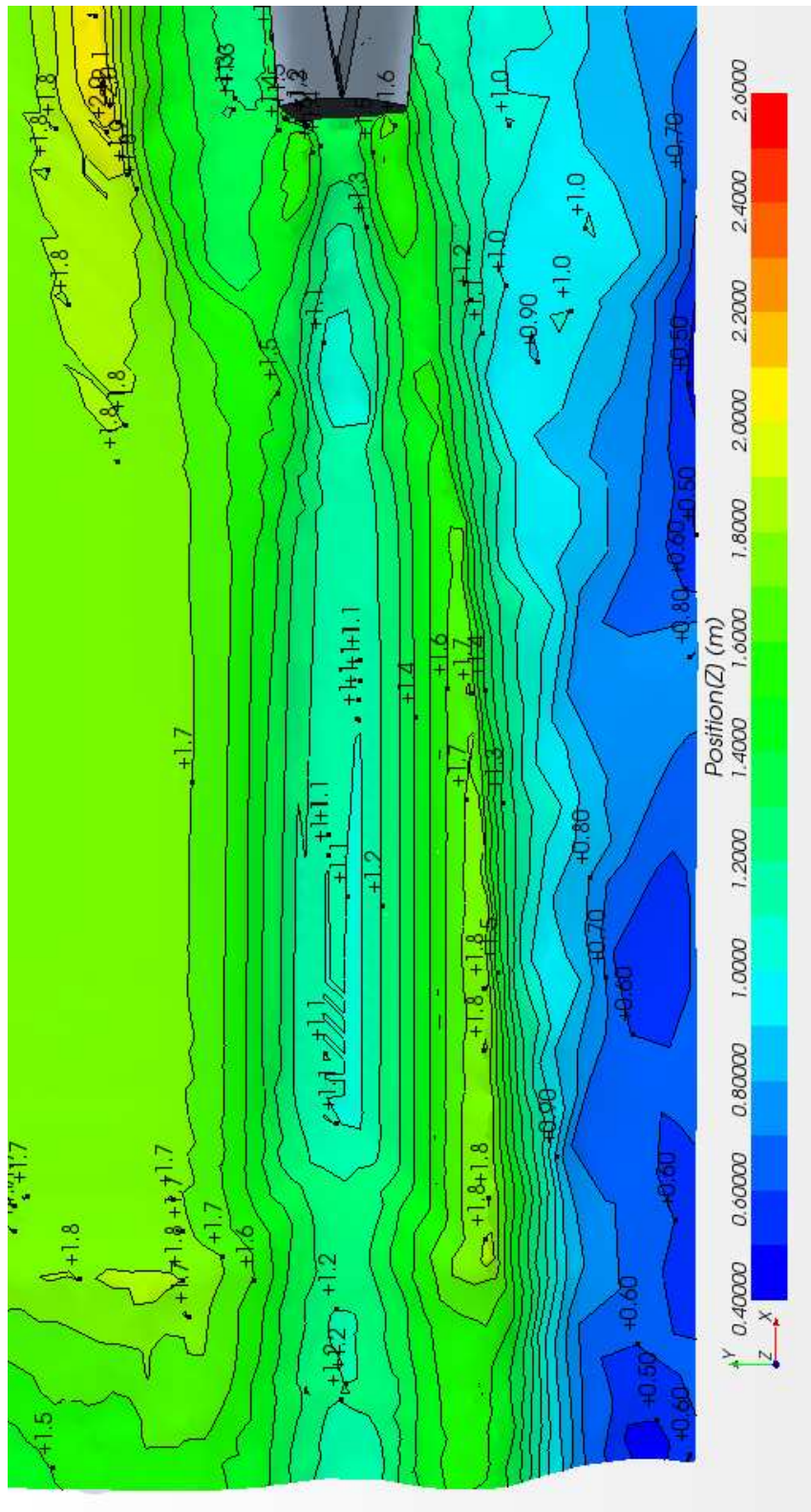


Figure C.1: Water surface at 90% water phase at 8 knots.

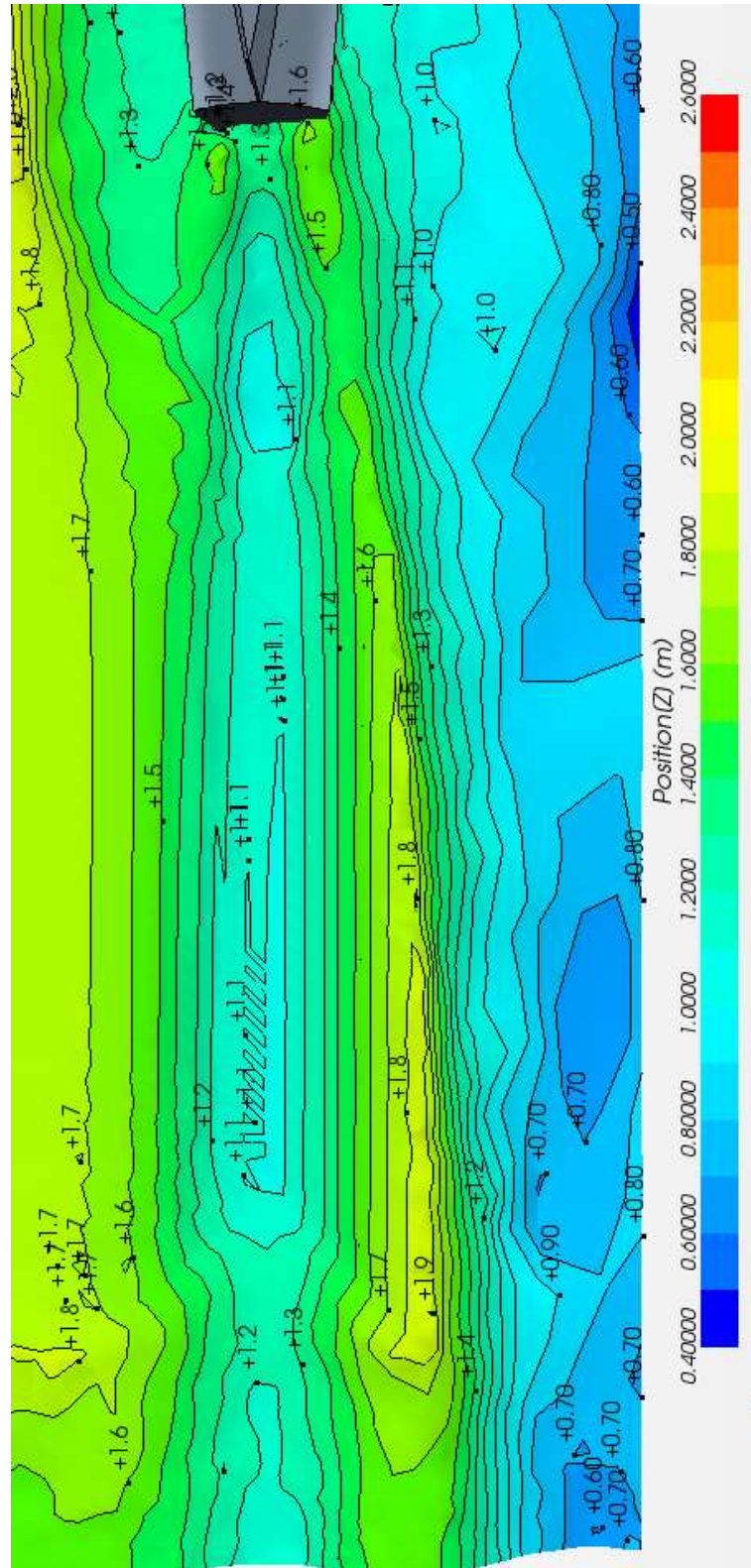


Figure C.2: Water surface at 90% water phase at 10 knots.

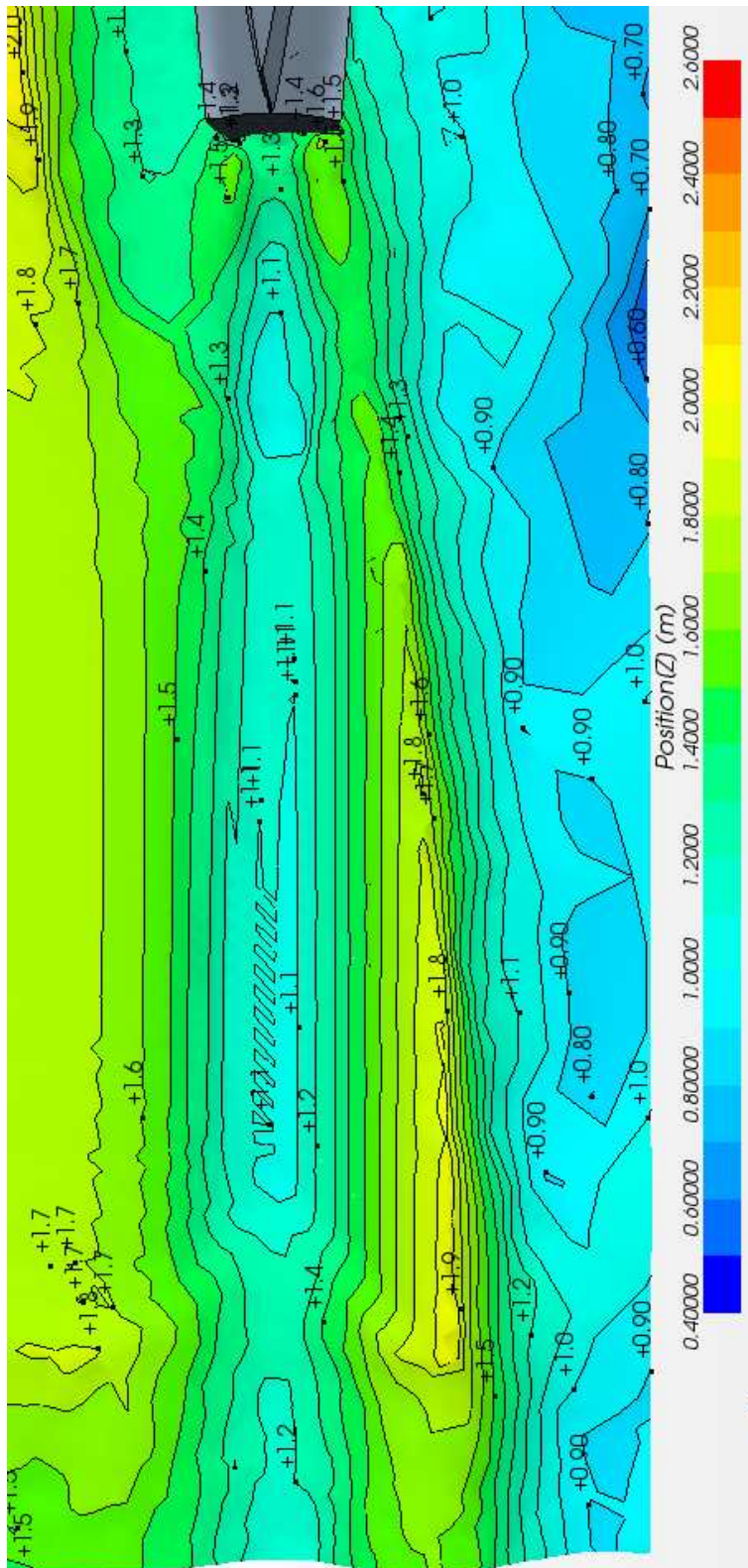


Figure C.3: Water surface at 90% water phase at 12 knots.

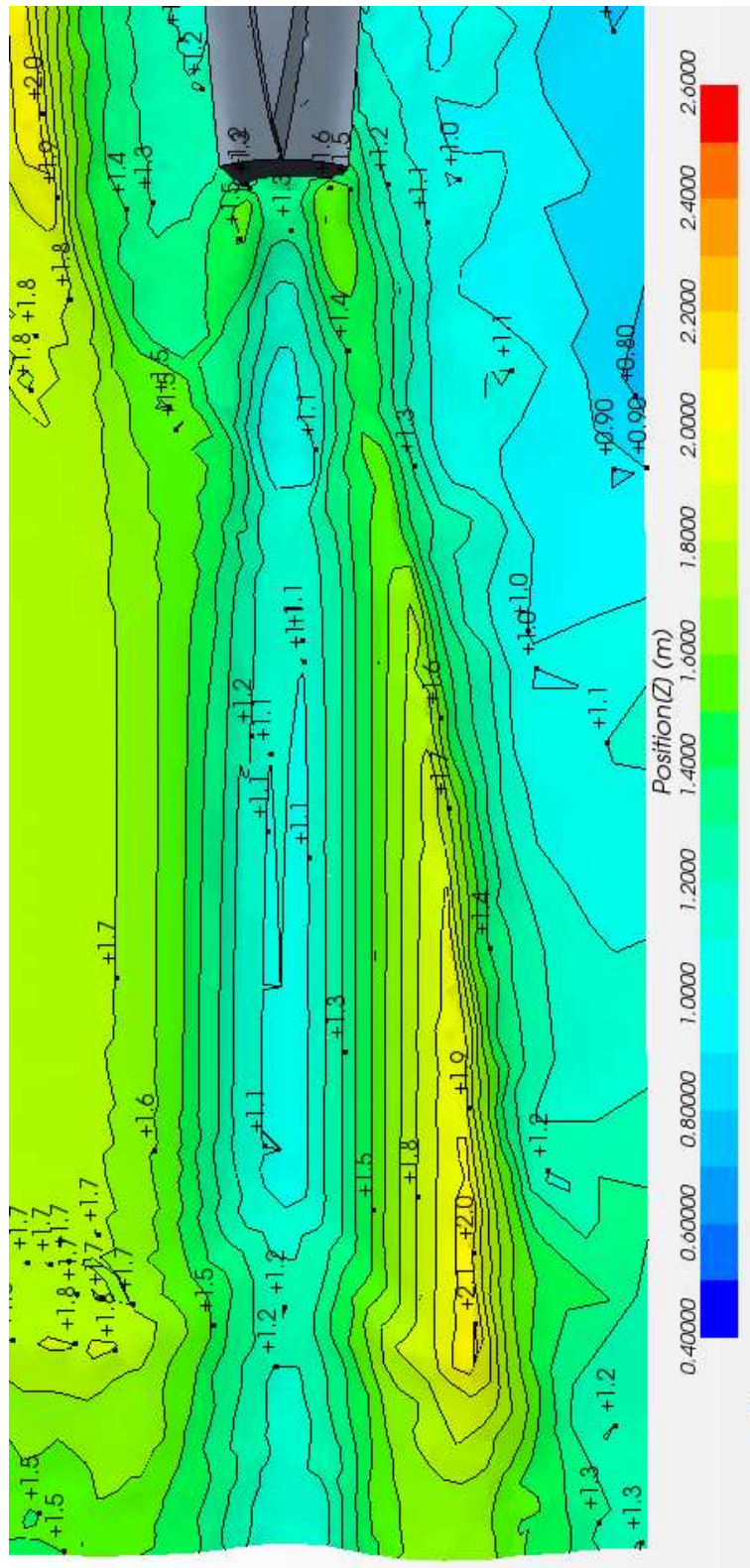


Figure C.5: Water surface at 90% water phase at 16 knots.

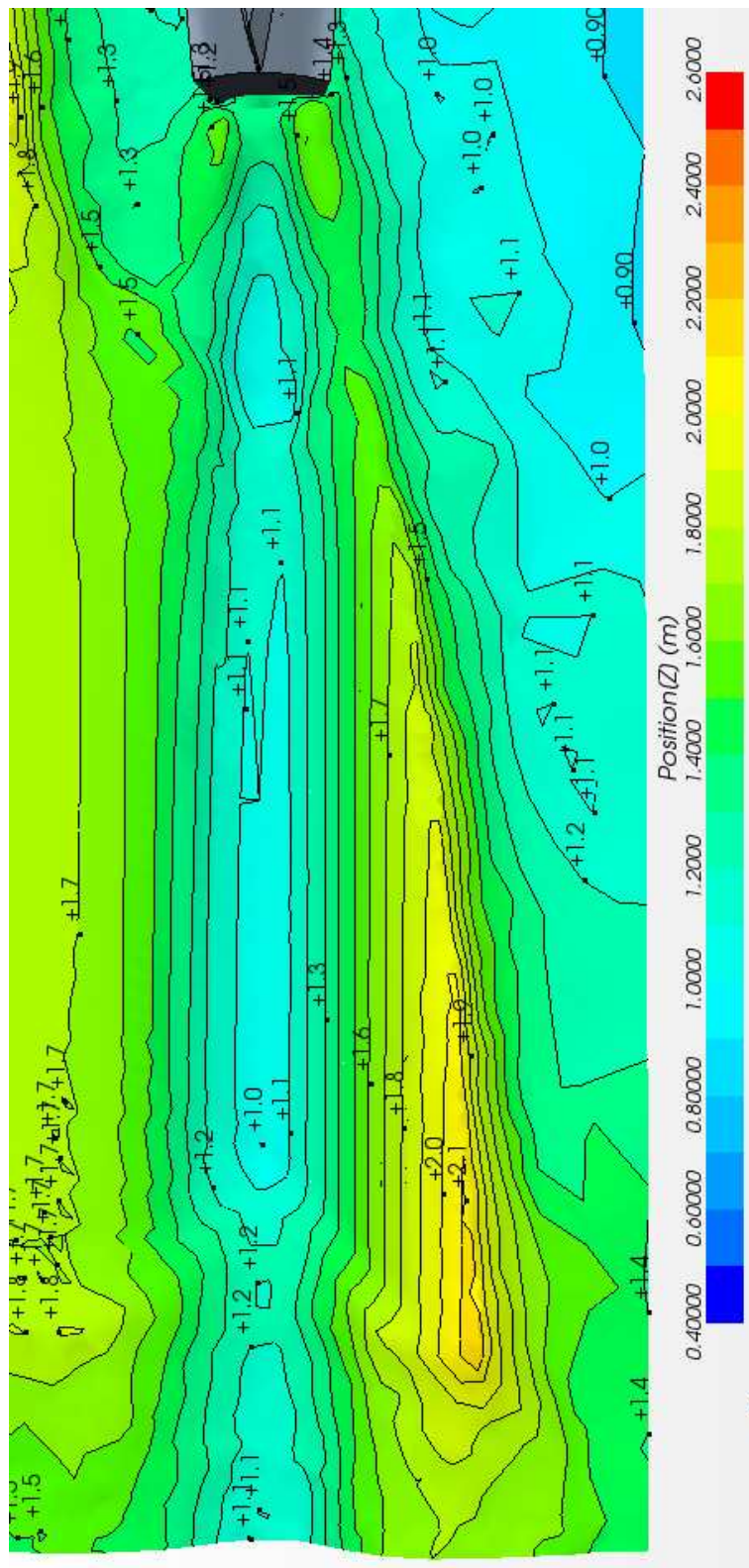


Figure C.7: Water surface at 90% water phase at 20 knots.

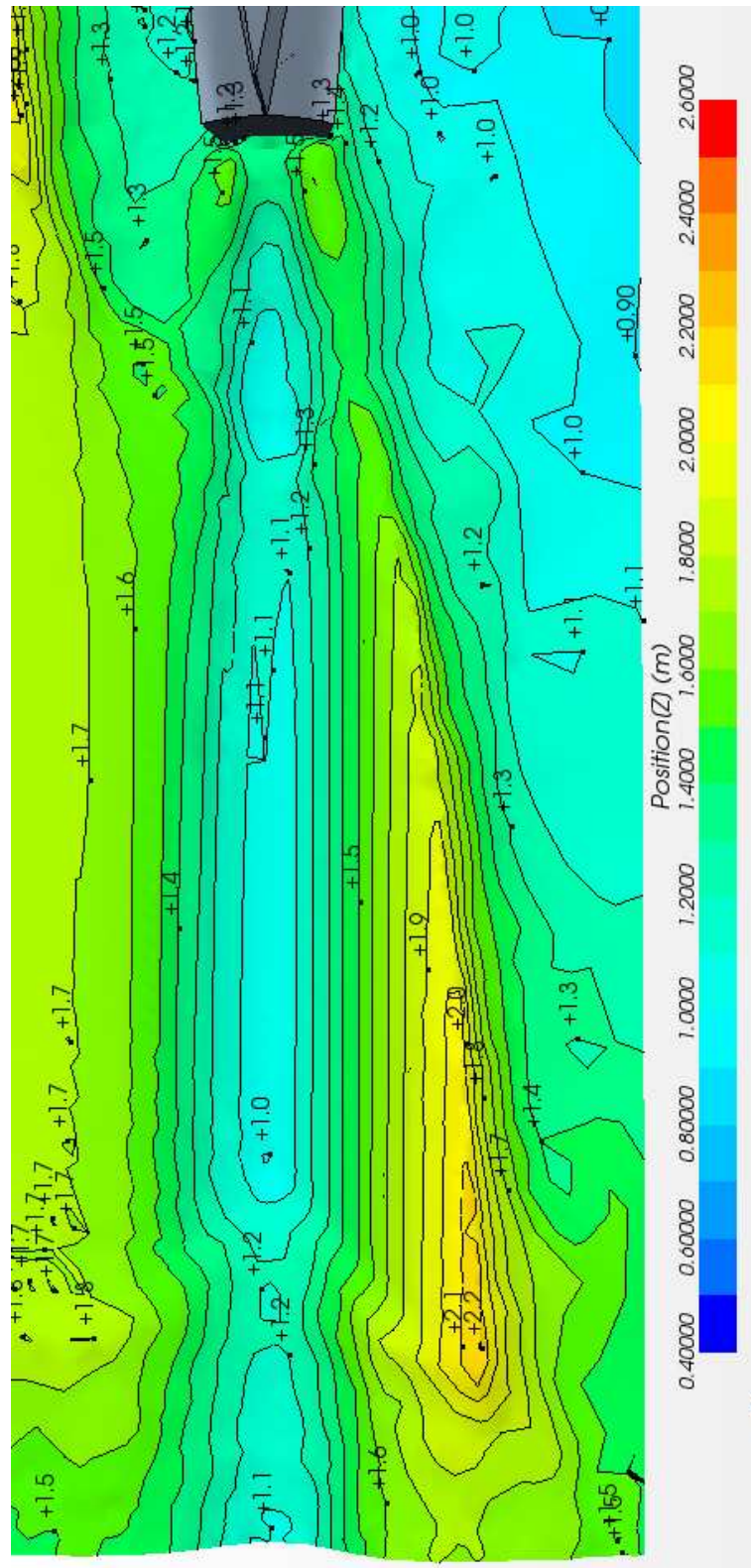


Figure C.8: Water surface at 90% water phase at 22 knots.

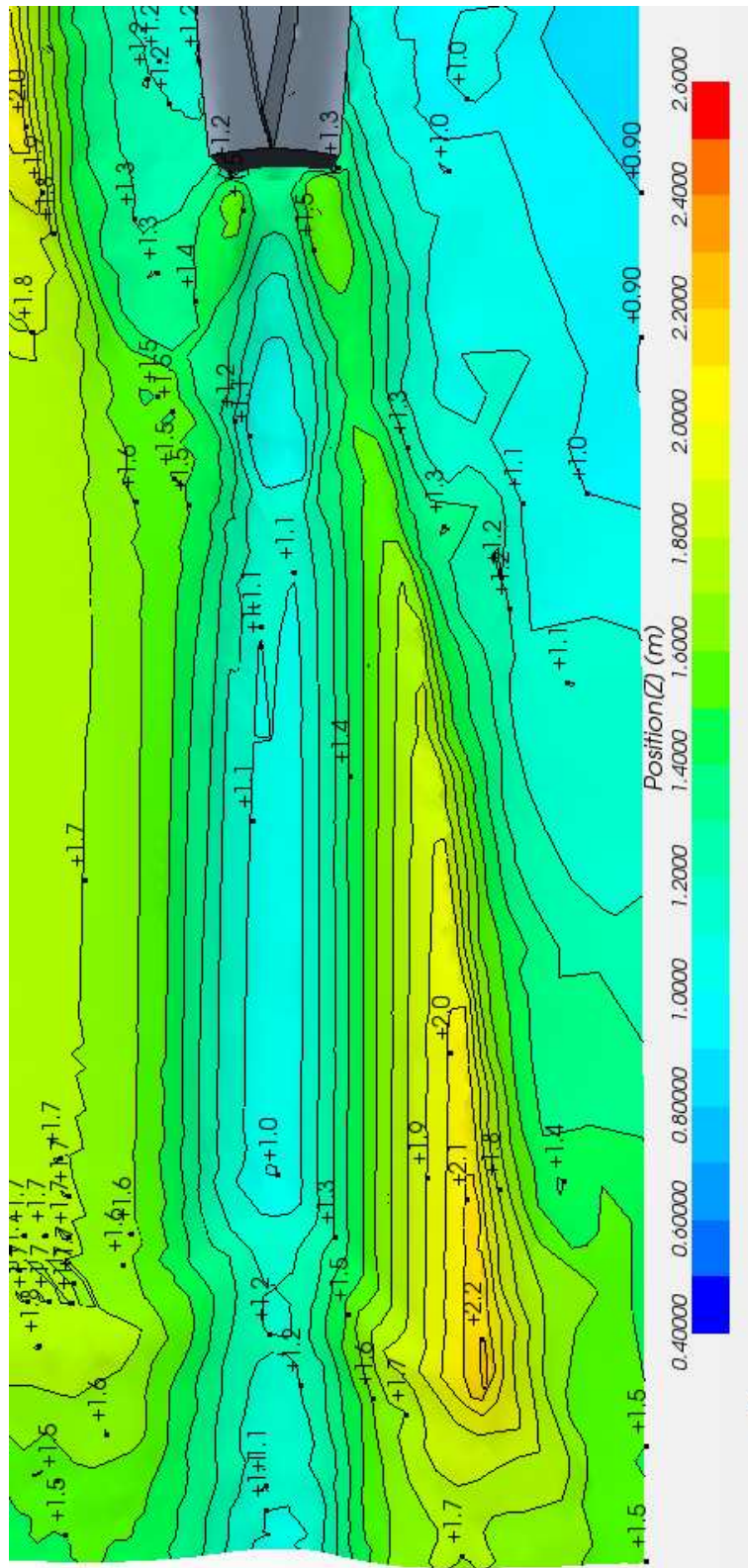


Figure C.9: Water surface at 90% water phase at 24 knots.

Bibliography

- R. Aris. *Vector, tensor, and the basic equations of fluid mechanics*. Dover Pubns, 1962.
- J. Bardina, J. H. Ferziger, and W. C. Reynolds. *Improved subgrid models for large eddy simulation*. AIAA paper 80-1357, 1980.
- CD-adapco. *STAR-CCM+ User Guide Version 6.04.014*, 2011.
- H. K. Dahle. *Lecture notes in continuum mechanics*. University of Bergen Department of Mathematics, 2010.
- Danish Yachts. SeaStrider (SWATH): Trailblazing Modern Crew Transport Vessels for Offshore Wind Farms, [Accessed 23 March 2012] . URL www.danishyachts.com/medias_news/SWATH.pdf.
- K. B. Dysthe. *Dimensjonsanalyse*. University of Tromsø Department of Mathematics, 1992.
- J. H. Ferziger and M. Perić. *Computational Methods for Fluid Dynamics*. Springer-Verlag, 2002.
- T. I. Fossen. *Handbook of Marine Craft Hydrodynamics and Motion Control*. John Wiley & Sons Ltd., 2011.
- R. I. Issa. Solution of the implicitly discretised fluid flow equations by operator-splitting, *J. Comput. Phys.*, vol 62, pp. 40-65, 1986.
- P. K. Kundu and I. M. Cohen. *Fluid Mechanics*. Academic Press Inc, 2010.
- B. P. Leonard. A stable and accurate convective modelling procedure based on quadratic upstream interpolation: *Computer Methods in Applied Mechanics and Engineering*, vol 19, pp. 59–98, 1979.
- Marine Roll & Pitch Control AS. Stabilization, [Accessed 23 March 2012] . URL http://www.mrpc.no/?page_id=307.

- F. R. Menter. *Two-equation eddy-viscosity turbulence modeling for engineering application*, 32(8) pp. 1598-1605, 1994.
- OpenCFD. *OpenFOAM - The Open Source CFD Toolbox - Documentation. 2.0 edition*. OpenCFD Ltd., 2011a.
- OpenCFD. *OpenFOAM - The Open Source CFD Toolbox - User's Guide. 2.0 edition*. OpenCFD Ltd., 2011b.
- V. Rieu and Z. Kishhev. *Still water performance tests, SWATH wind turbine service vessel*. Force Technology, 2012.
- P. J. Roache. *Computational fluid dynamics*. Hermosa, Albuquerque, NM, 1976.
- SALOME. Salome is an open-source software that provides a generic platform for pre- and post-processing for numerical simulation, [Accessed 23 January 2012] . URL <http://www.salome-platform.org/>.
- D. Savitsky. On the subject of high-speed monohulls, in: *Presentation to the Greek Section Of the Society Of Naval Architects and Marine Engineers, Athens, Greece.*, 2003.
- J. B. Scarborough. *Numerical mathematical analysis*. The Johns Hopkins Press, 1958.
- SNAME. The Society of Naval Architects and Marine Engineers. Nomenclature for treating the motion of a submerged body through a fluid, in: *Technical and Reasearch bulletin No. 1-5*, 1950.
- D. B. Spalding. A novel finite-difference formulation for differential expressions involving both first and second derivatives, *Int. J. Numer. Methods Eng.*, vol 4, pp. 551, 1972.
- D. B. Spalding. *Computational fluid dynamics*. Hermosa, Albuquerque, NM, 1976.
- Stadt Towing Tank AS. Hydrodynamic test facility located in deknepollen, close to the city of måløy, [Accessed 21 March 2012] . URL <http://www.stadttowingtank.no/>.
- I. Surjo and W. Adj. *Lecture notes: Chapter 7. Resistance and powering of ships*. Institut Teknologi Sepuluh Nopember(ITS), 2007.
- P. K. Swedby. High resolution schemes using flux limiters for hyperbolic conservation laws, *SIAM J. Numer. Anal.*, vol 21, no. 5, pp. 995-1011, 1984.

- J. Tu, G.H. Yeoh, and Liu C. *Computational Fluid Dynamics: A Practical Approach*. Butterworth Heinemann, 2007.
- H. K. Versteeg and W. Malasekera. *An introduction to computational fluid dynamics: The finite volume method*. Pearson Education Limited, 2007.
- D. C. Wilcox. *Turbulence Modeling for CFD*. DCW Industries, 2006.